Application of hyper-spectral remote sensing to assess contamination associated with gold mining in the Witwatersrand Gold Basin, South Africa

Mafuza Maya

A research report submitted to the Faculty of Science, University of the Witwatersrand, in fulfilment of the requirements for the degree of Master of Science

Supervisor: Dr H Tutu
Co-Supervisors: Dr A Ramoelo
Ms I Weiersbye

JOHANNESBURG, AUGUST 2014

DECLARATION

I declare that this research report is my own, unaided work. It is being submitted for the Degree of Master of Science at the University of the Witwatersrand, Johannesburg. It has not been submitted before for any degree or examination at any other University.

_____

(Signature of candidate)

Signed on the __15th___day of ___August___2014

Abstract

Efflorescent minerals are a common feature of the soil surface in seasonal environments where evapotranspiration (ET) exceeds precipitation (P), and are formed by the evaporation of salt solutions from the soil during periods of drying. On the Highveld gold fields, ET exceeds rainfall by approximately two-and-a-half times during the dry season, and soils overlying acid mine drainage and along polluted stream banks can become covered by distinctively coloured mineral efflorescent crusts. Whereas some efflorescent minerals are relatively insoluble and present a negligible environmental hazard (for example, gypsum), others may be readily soluble and contain high concentrations of potentially toxic metals (for example, copiapite, jarosite and uranyl sulphate). During periods of rainfall, such salts are washed further afield and into surface water bodies and act as sources of episodic pollution.

The presence of some efflorescent minerals can be detected from their characteristic reflectance signatures using remote-sensing (RS) of the electromagnetic spectrum. The species of efflorescent minerals present is a useful indication of the spatial extent of sub-surface contamination, and also of the chemical conditions of the substrate, in particular the concentration of total dissolved solids, pH and redox conditions.

The aim of this study was therefore to assess the use of remote-sensing on indicator efflorescent minerals as a cost-effective aid in the spatial mapping of acid rock-drainage polluted soils and water-bodies. This study describes the range of efflorescent crusts identified on different land-use areas and soil classes in a Highveld gold-mining region. Crusts were first measured in-situ under natural sunlight using a portable analytical spectral radiometer (ASD) as well as using X-ray diffraction (XRD). They were then dissolved in deionized water and the resulting salt solutions allowed to evaporate prior to analysis under controlled lighting conditions. Spectra were post-processed and compared with

geological spectral reference libraries. The salt solutions were also analyzed for metal and sulphate content and the results were used to establish evaporation models from which mineral precipitation could be predicted.

Minerals identified in the visible near-infra red (VNIR) region included iron oxides (hematite and goethite), and the sulphate mineral jarosite. In the short wave infra-red (SWIR) region clay minerals of the smectite group were dominant. Gypsum and Al-Mn-Mg-Na sulphate salts were identified in the SWIR region as mixtures occurring with clay minerals. Minerals identified in the VNIR-SWIR region were all confirmed by X-Ray diffraction (XRD). Upon dissolution, geochemical modeling revealed that gypsum and jarosite are the most common minerals expected to precipitate. The precipitation of gypsum and jarosite indicates persistent acidic conditions after dissolution of mineral salts. Gypsum and jarosite were also accurately identified by hyper-spectral spectroscopy and confirmed by XRD and geochemical modeling. Agreement between spectral interpreted minerals and geochemically precipitated mineral phases demonstrated the ability of hyper-spectral data in detecting efflorescence minerals on the soil surface. Using partial least squares regression (PLSR) combined with bootstrapping, reflectance spectrum was significantly correlated with geochemical variables.

Acknowledgements

I would like to express my sincere appreciation and gratitude to:

- My supervisors, Dr Hlanganani Tutu and Ms Isabel Weiersbye for their guidance and continual support during my studies at Wits.
- Dr Abel Ramoelo, for his encouragement, patience and for providing access to all the software programmes used in the study.
- Mr Malcom Sutton for his support in sample collection and preparation.
- My friends, Kgaukgelo Mashishi and Sydney Muthige for their support during my studies.
- The Council for Geoscience and The Department of Science and Technology for joint funding of the research through the South African Geological Hazard Observation Systems project.
- National Research Foundation and Anglo Gold Ashanti for partly funding my studies.

Contents

DECLARATION ii
Abstract iii
Acknowledgements v
Contents vi
Figures vii
Tables ix
Acronyms x
1 Background to the study 1
1.1 Introduction to mine waste and acid mine drainage in the Witwatersrand basin 1
1.2 Problem statement 3
1.3 Research objectives and research questions 3
1.4 Description of the study area 5
1.5 Structure of the research report 8
2 Literature review 9
2.1 Background and chemistry of acid mine drainage 9
2.1.1 Weathering of sulphide minerals 9
2.1.2 Neutralisation processes 10
2.1.3 Microbiological activity 11
2.1.4 Formation of efflorescent salts 12
2.1.5 Previous research on acid mine drainage in the Witwatersrand Basin. 13
2.2 Introduction to remote sensing for geochemical hazard assessment 15
2.2.1 The interaction of electromagnetic waves with minerals 15
2.2.2 The spectral reflectance of minerals associated with acid mine drainage 16
2.2.3 Spectral characteristics of salinity 18
3 Materials and methods 20
3.1 Overview of the methodology 20
3.2 Sample collection 21
3.3 SEM and XRD analysis 22
3.4 Laboratory procedures 22
3.5 Collection of reflectance spectra 26
3.6 Analysis of reflectance spectra 26
3.6.1 Quantitative absorption feature (QAF) analysis 28
3.6.2 First derivative reflectance transformation 29
3.7 Geochemical modelling 30
3.8 Statistical modelling techniques 30
4 Results and discussion 33
4.1 Geochemical characteristics of salt precipitates 33
4.1.1 Descriptive statistical analysis 33
4.1.2 Multivariate statistical analysis 39
4.1.3 Effect of land use and sample colour on the total concentration of elements 44
4.2 Geochemical assessment of contamination levels 45
4.2.1 Enrichment factors 45
4.2.2 Index of Geo-accumulation 47

4.2.3 Pollution Load Index 49
4.3 Mineralogy and geochemical modelling 50
4.3.1 X-ray diffraction and SEM mineralogical phases 50
4.3.2 Geochemical modelling 56
4.4 Spectral characteristics 68
4.4.1 Analysis of reflectance spectra 68
4.4.2 Identified minerals and their diagnostic absorption features 69
4.4.3 Relationship between spectral mineral end-members and XRD mineral phases 73
4.5 Correlation between spectral charactersitics and geochemistry 74
4.5.1 Correlation of geochemical variables with spectral parameters (QAF) 75
4.5.2 Regression results with non-spectral data 77
4.5.3 Spectral indices for salts 79
4.5.4 Partial Least Squares Regression 82
4.5.5 Determination of important wavelengths in PLSR models 87
5 Conclusion and recommendations 89
6 References 94

Figures

Figure 1-1 Study area with selected sample points 6
Figure 2-1 Diagnostic features in the spectra of Fe minerals (USGS spectral library) 17
Figure 2-2 Surface features of salts in the study area 19
Figure 3-1 General overview of study methodology. 20
Figure 3-2 Buffer solutions and EC-pH meter 24
Figure 3-3 Example of first derivative spectrum for selected samples 30
Figure 4-1 Box plots showing the variation of pH according to different land uses 34
Figure 4-2 Distribution of samples in Ficklin Diagram 35
Figure 4-3 Distribution of selected major ions against pH 36
Figure 4-4 Dissolved concentrations divided by total concentrations plotted against pH for selected elements. 37
Figure 4-5 Variation of EC according to different land uses 38
Figure 4-6 Variation of major anions in the study area 38
Figure 4-7 Relationship between sulphate and selected elements 42
Figure 4-8 Ca/SO_4 ratio plotted against pH 43
Figure 4-9 Median values of selected elements in different salt precipitates 44
Figure 4-10 Variation of EF values for selected element 47
Figure 4-11 Variation of Igeo for selected elements 48

Figure 4-12 Variation of calculated PLI values 50
Figure 4-13 SEM images of Blodite and Picromerite 53
Figure 4-14 SEM image of Wupartkiite and Hexahydrite 54
Figure 4-15 SEM images of Tamarugite, Apjohnite with Mn-Mg-S matrix 55
Figure 4-16 SEM image of Jarosite and Fe-rich matrix 55
Figure 4-17 Evaporation model of minerals expected to precipitate from MWS 38: a) Evaporation profile with no equilibrated gases and no charge balance b) With charge balance on carbonate species and equilibration with oxygen c) Evaporation profile with no charge balance and equilibration with atmospheric gases. 59
Figure 4-18 Evaporation model of minerals expected to precipitate from MWS 51, a) Evaporation profile with no equilibration of gases b) Evaporation profile with the equilibration of atmospheric gases 60
0Figure 4-19 Evaporation model of minerals expected to precipitate from MWS 68, a) Evaporation profile without equilibration of gases, b) Jarosite curve of the same model, c) Evaporation profile assuming complete equilibration with atmospheric gases 62
Figure 4-20 Evaporation model of minerals expected to precipitate a) when equilibrated with oxygen b) and then with water 63
Figure 4-21 Evaporation models of minerals expected to precipitate in equilibrium with atmospheric gases a) modelled without oversaturated solids, b) when solids jarosite and pyrolusite are taken into account 63
Figure 4-22 Evaporation model of minerals expected to precipitate without equilibration of gases. 64
Figure 4-23 Evaporation model of minerals expected to precipitate a) without atmospheric gases, b) when equilibrated with atmospheric gases. 65
Figure 4-24 Generalised precipitation sequence from XRD results, showing the relationship between evaporation, humidity and cation substitution (Adapted from Onac et al, 2003). 66
Figure 4-25 Reflectance spectrum of selected samples with wavelength positions that were used in mineral interpretation 69
Figure 4-26 Continuum removed reflectance spectra of a) Montmorrillonite and b) Vermiculite..... 71
Figure 4-27 Continuum Removed reflectance spectrum of a) Hematite and b) Geothite 72
Figure 4-28 Reflectance spectrum of Thernadite and Copiapite 74
Figure 4-29 Collelogram of reflectance spectra and geochemical variables (n=29) 75

Figure 4-30 Significant spectral parameters for pH and SO_4^{2-} variables. 78
Figure 4-31 Variation of soil reflectance in various sample colours 81
Figure 4-32 The influence of salinity in spectral reflectance of salts 82
Figure 4-33 PLSR coefficients showing the contribution of each wavelength for development of geochemical models 85
Figure 4-34 B coefficients (blue line) for SO_4^{2-}, EC and pH PLSR models. Black threshold lines are defined using standard deviation. 88

Tables

Table 3-1 Summary of chemical laboratory procedures (Adapted from Estifanos, 2006 and Maritz et al, 2010). 25
Table 4-1 Statistical summary of geochemical variables (n = 29; all elements in mg kg^{-1}) 34
Table 4-2 Comparison of major anions (mg kg^{-1}), EC (mS/cm) and pH in crusts to soil and water levels. 36
Table 4-3 Spearman correlation analysis for elements in mineral salts 41
Table 4-4 Results (p-values) of comparison between land use and colour ($\alpha = 0.05$) 45
Table 4-5 Classes of contamination by metals according to EF indices 46
Table 4-6 Classes of contamination by metals according to EF indices 48
Table 4-7 Classes of contamination by metals according to PLI indices (Kalender and Ucar, 2013) ... 49
Table 4-8 X-ray diffraction mineral weight percentage for selected mineral precipitants 51
Table 4-9 Physical parameters and anions of the leachates used in the evaporation experiment. 57
Table 4-10 Charge balances and pe values of the solutions 58
Table 4-11 Predicted XRD and ASD interpreted mineral of selected salt precipitates 67
Table 4-12 Minerals identified in spectral analysis 70
Table 4-13 Wavelength position of absorption features caused by water and metal bonding 73
Table 4-14 Correlation coefficients between spectral parameters variables and geochemical variables 76
Table 4-15 Normality test for QAF parameters (n=30) 77
Table 4-16 Soil Indices for soil colour characterization 79
Table 4-17 Spectral indices for salinity (Khan et al, 2001) 79

Table 4-18 Explanatory statistics for all calculated spectral variables (n=29). 80
Table 4-19 Correlation between pH, EC and spectral measurements of soil salinity..... 80
Table 4-20 Performance of spectral transformation techniques for estimating geochemical variables using PLSR with bootstrapping (n=29). 86
Table 4-21 B-coefficient standard deviation of selected geochemical variables..... 87
Table 4-22 Significant spectral regions selected by PLSR weights..... 87

Acronyms

AMD: Acid Mine Drainage

ASD: Analytical Spectral Devices, Inc

CR: Continuum Removal

EC: Electrical Conductivity

EF: Enrichment Factor

*I*geo: Index of Geo-accumulation

MAE: Mean Absolute Errors

ME: Model Efficiency

pH: Hydrogen Potency

PLI: Pollution Load Index

PLSR: Partial Least Square Regression

QAF: Quantitative Absorption Feature

R^2: Coefficient of Determination

RMSE: Root Mean Square Error

RPD: Ratio of Prediction to Deviation

SEM: Scanning Electron Microscope

SWIR: Short Wave Infrared

TDS: Total Dissolved Solids

TSF: Tailings Storage Facilities

VNIR: Visible Near Infrared

1 Background to the study

1.1 Introduction to mine waste and acid mine drainage in the Witwatersrand basin

Mining activities in the Witwatersrand Basin have resulted in six billion tons of mine waste containing 30 million tons of sulphur and approximately 430 000 tons of uranium in the tailings storage facilities (Hobbs and Cobbings, 2007; Weiersbye *et al*, 2006a). Part of this mine waste includes more than 270 tailings dams, which cover an area of about 400 to 500 km^2 (Hobbs and Cobbings, 2007). In addition to the uraniferous nature of the tailings (which is a cause of great concern), the oxidation of sulphide bearing waste material releases metals into the surrounding environment. This has resulted in severe environmental degradation as a result of water and soil pollution. Sources of contamination from abandoned workings are two fold namely: 1) contamination from rising water in mine voids and 2) contamination from mine tailings. The contamination from rising water in mine voids is due to the large number of gold mines in the area that have been closed down. The closure of mines means that the pumping of subsurface water from mine voids is no longer taking place which results in large quantities of water accumulating in the cavities. The rising water levels in these workings necessitate pumping and treatment with lime before discarding the water into open water bodies. However, in general, the lime treatment was considered to be unsuccessful since large quantities of low quality water were entering open water bodies without treatment (Coetzee *et al*, 2006). Moreover, lime treatment results in the formation of large quantities of sludge containing elevated metal concentrations. It is estimated that 25 million litres of contaminated water is discharged into surface water bodies per day and that 100 tons of salt is deposited into the surrounding environment every day (Hobbs and Cobbings, 2007). The discharge of mine water has resulted in

high salinity levels in the Vaal River and other local streams. The water contaminated by mine water discharge typically has a pH of less than 4 and is associated with a high concentration of iron and other metals (Hobbs and Cobbing, 2007). The iron oxidizes on exposure to water and air and precipitates along the water flow paths, leaving visually observable precipitates on river beds and banks (Valente *et al*, 2009). An additional source of contamination is the gold-rich waste storage facilities which are a source of metal pollution in this region.

Many studies have been conducted on acid mine drainage and metal contamination in soils, plants, waters and sediments (Coetzee *et al*, 2006; Weiersbye *et al*, 2006a; Tutu *et al*, 2005) as part of rehabilitation programs in the Witwatersrand gold mining areas. The assessment and monitoring of environmental contamination based on plant, water and soil sampling and physiochemical analysis using conventional methods is costly, labour intensive and time consuming.

Remote sensing techniques such as multispectral imaging have been used as a cheaper alternative to map different materials at the surface of the earth based on their spectral signatures (Quental *et a*l, 2011; Riaza *et al*, 2012). Imaging spectroscopy or hyperspectral remote sensing offers high quality data (reflectance spectra) because it measures many (> 100), narrow (2-5 nm) contiguous spectral bands and high spatial resolution. For mineral mapping and physiochemical characterization, the visible-near-infrared (VNIR) region 350 nm – 2500 nm of the electromagnetic spectrum is measured by hyperspectral sensors.

Weiersbye *et al.* (2006b) successfully mapped secondary minerals associated with seepage zones to characterize ground water pollution in gold mining areas. Wu *et al.* (2007) successfully used hyperspectral data to assess sulphide related contamination. Statistical techniques such as the

partial least squares regression (PLSR) have been used to relate hyperspectral data to physiochemical data of plants, soils and minerals (Wold *et al*, 2001). In Europe, continuous analysis of hyperspectral images is used to monitor spectral indicators of acid mine drainage (Riaza *et al*, 2012). These studies prove that hyperspectral data can be used as an efficient and cheaper alternative to characterize and monitor environmental pollution.

1.2 Problem statement

Water contaminated by mine residue material is acidic and contains significant amounts of metals. Evaporation results in the formation of efflorescent salts from the concentrated mine water solutions. The precipitated salts are unstable and dissolve readily in the presence of water. The dissolved salts tend to increase the acidity of the water in which it they are dissolved and remobilise metals in the environment.

The high concentrations of metals in the efflorescent salts pose a significant geochemical hazard. This hazard is compounded by the fact that these mineral salts occur in sensitive areas such as residential areas, cultivated fields and watercourses. In order to focus remediation efforts, cost-effective methods are needed to characterise the acid mine drainage plume based on the distribution and prevalence of the salt crusts.

1.3 Research objectives and research questions

The ultimate objective of the research was to assess shallow groundwater contamination in selected portions of the Witwatersrand Basin using a combination of remote sensing techniques and geochemical modelling by considering efflorescent salts as surrogates for contamination. To achieve these objectives, the research focused on the following research questions:

1. To what extent do efflorescent minerals pose geochemical hazards to the surrounding environment?
2. Which minerals can be used as indicators for geochemical hazards?
3. Which minerals can be identified using the visible portions of the electromagnetic spectrum?
4. What are suitable spectral transformation techniques for characterization of efflorescent salts?
5. Which spectral indices and wavelength bands can be effectively used for identification of mineral salts?
6. Can spectral techniques be complemented by geochemical modelling techniques?

To achieve the objectives and answer the research questions, the following field data collection and data analysis strategies have been performed:

1. The assessment of changes in mining areas in the East Rand over the last 10 years using remote sensing data;
2. The collection of samples of mineral salts from selected tailings storage facilities and capillary fringes in the vicinity of impacted water systems;
3. The mineralogical analysis of efflorescent salts using X-ray diffraction and hand-held infrared spectrometer measurements;
4. The total elemental and anionic concentration analyses of dissolved salts;
5. The construction of evaporation models of dissolved salts to assess mineral precipitation;
6. The assessment of shallow groundwater contamination using the resulting information as input;

7. Establishment of the relationship between geochemical parameters and reflectance spectra and
8. Determination of the spectral bands suitable for modelling of geochemical variability.

1.4 Description of the study area

The study area covers the eastern part of the Witwatersrand Basin in the Ekurhuleni Metropolitan Municipality. Mining operations in these areas include four deep level gold mines with supporting infrastructure such as metallurgical plants, chemical laboratories, tailings storage facilities, waste rock dumps and evaporation dams. The study area has been intensively mined and hosts some of the oldest tailings dams. The surrounding areas are dominantly zoned for residential purposes and agriculture. The study area (Figure 1-1) was chosen because of the long history of mining and availability of geographical data. Periodical soil biogeochemical data is collected as part of on-going rehabilitation programs at these sites. Other rehabilitation methods in the area include ground water monitoring, re-vegetation of tailings dams, groundwater dewatering, and stream diversion and widening.

The study area is characterized by warm to hot, rainy summers and cold dry, sunny winters. Annual rainfall average ranges between 600 mm – 625 mm with a mean temperature of 30°C in summer and 18°C in winter. Prevailing north-westerly winds are dominant in this region. Evaporation rates are high in the Highveld region with a summer annual average of 1900 mm per annum (DWA, 2012). Because the tailings dams and storage waste facilities are uncovered and unvegetated, winds in the study area give rise to dust storms by dispersing tailings material. Warm and dry conditions together with high evaporation rates promote capillary movement of saline groundwater in the soil profile leading to increased weathering rates.

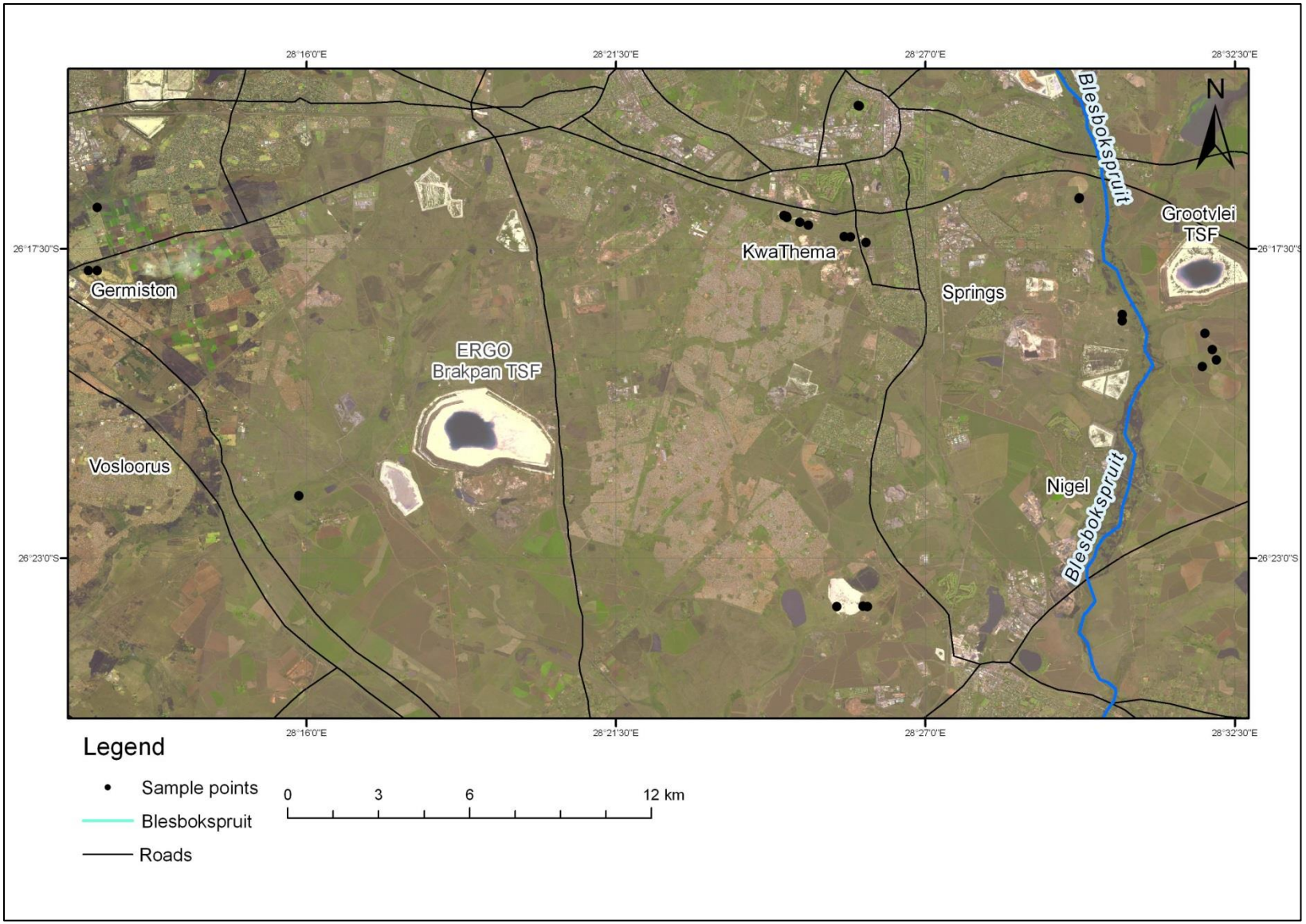

Figure 1-1 Study area with selected sample points

Tailings storage facilities are common landmarks in this region. In the Ekurhuleni Metropolitan Municipality region, mine residue deposits cover an area of about 7956.5 hectares, whereas slime dams and footprints cover 6742.4 hectares (Sutton *et al.*, 2006). Rock and process effluents that are generated during the mining processes are stored in them. The tailings are generally acidic, with a pH that ranges from 2 to 4.11. These structures show similar mineralogy to that of the Witwatersrand ores. Quartz is the most abundant mineral in tailings impoundments. Within the oxidized zone, there is little or no pyrite because of weathering (Nengovhela *et al*, 2006). Common secondary sulphides include pyrrothite (FeS_2), chalcopyrite ($CuFeS_2$), pentlandite (Fe, $Ni)_9$,S_8) and sphalerite (ZnS) (McCarthy, 2006).

An aerial photography survey by Sutton *et al.* (2006) showed that about half of the mine residue deposits were situated within watercourses. Several of these deposits were built on wetlands and pans. The study also revealed that about 64% of the mine residue had undergone structural failure and, consequently, spillage resulting in extensive sedimentation along water channels. A small number of mine residue deposits were built on dolomite areas to take advantage of the neutralizing effect of dolomites, and also to improve drainage and thus structural stability. The majority of mine residue deposits were closely associated with residential and agricultural areas.

Abiye *et al.* (2011) summarized the hydro-chemical characteristics of Department of Water and Environmental Affairs boreholes in the Witwatersrand Basin. Borehole waters are characterized by high salinity and pH levels. These trends are attributed to leaching from weathering profiles and carbonate saturation. The impermeable nature of chert-rich dolomites is responsible for

decreasing Mg concentration with depth. High concentrations of chloride and sulphate occur at a depth of up to 60 meters. The presence of soluble salts in the weathering profile and soil crusts contributes to high chloride concentrations. The dissolution caused by acidic conditions also leads to high sulphate and total iron concentrations (Abiye *et al*, 2011).

1.5 Structure of the research report

Acid mine drainage is a problem and the environmental and health and safety concerns require that ways to mitigate the problem need to be formulated. However, before this can be done, we need to understand the mechanisms that lead to acid mine drainage, the environmental and physical attributes of the study area that accelerate the processes and to find ways to effectively and efficiently map the extent of affected areas. This will enable the identification of mitigation and relief strategies.

General background information on sulphide weathering, formation, chemistry and processes of acid mine drainage is introduced in Section 2.1. Spectral characteristics of minerals associated with acid mine drainage are presented in Section 2.2. This effectively provides the background for the use of remote sensing techniques to rapidly map large areas affected my AMD remotely. The materials and methods used for geochemical hazard assessment in this investigation are presented in Section 3. Results are presented and discussed in Chapter 4 while Chapter 5 entails concluding remarks and recommendations.

2 Literature review

2.1 Background and chemistry of acid mine drainage

2.1.1 Weathering of sulphide minerals

Sulphide minerals such as arsenopyrite and pyrite are stable under reducing conditions where they are formed. They become unstable in oxygenated water and react to form acidic plumes that result in the formation of secondary minerals (Dold, 2005). Pyrite is the main source of acid mine drainage. During oxidation, pyrite follows the reaction (Hammastrom *et al*, 2005; Dold, 2005):

$$2FeS_2 + 2H_2O + 7O_2 = 2Fe^{2+} + 4SO_4^{2-} + 4H^+ \qquad \textit{Equation 1}$$

The ferrous ion formed further oxidizes to form ferric iron:

$$4Fe^{2+} + O_2 + 4H^+ = 4Fe^{3+} + 2H_2O \qquad \textit{Equation 2}$$

The ferric ion becomes the primary oxidant of pyrite:

$$FeS_2 + 14\ Fe^{3+} + 8H_2O = 15\ Fe^{2+} + 2SO_4^{2-} + 16H^+ \qquad \textit{Equation 3}$$

During hydrolysis the ferric ions releases H^+ ions and precipitates $Fe(OH)_3$

$$Fe^{3+} + 3H_2O = Fe\ (OH)_3 + 3H^+ \qquad \textit{Equation 4}$$

The overall sequence reaction of pyrite can be summarized as follows

$$4FeS_2 + 14H_2O + 15O_2 = 4\ Fe(OH)_3 + 8SO_4^{2-} + 16H^+ \qquad \textit{Equation 5}$$

Formation of $Fe\ (OH)_3$ is acid generating and buffers the pH of acid mine drainage (AMD). The above reactions show that for every mole of FeS_2 oxidized, 4 moles of H^+ are released. This is a highly acidic reaction (Dold, 2005). The liberated H^+ ions are capable of producing more acidic waters. Decreasing pH conditions also increase the solubility of iron.

Oxidation products of pyrite (iron oxides, sulphate ions and hydrogen ions) react with minerals on the surface resulting in the formation of sulphuric acid which further exacerbates the acid mine drainage problem. For example, iron sulphate react with chalcopyrite as follows:

$$CuFeS_2 + 2Fe_2(SO_4)_2 + 2H_2O + 3O_2 = CuSO_4 + 5FeSO_4 + 2H_2SO_4 \qquad \textit{Equation 6}$$

Tailings storage facilities have high surface areas with finely grained crystals that lead to increased mineral reactivity and high oxidation rates in these sites (Riaza *et al*, 2012; Nengovhela *et al*, 2006)

Prevailing climatic conditions also affect the oxidation of sulphide minerals in tailings storage facilities. During rainy seasons, increased oxidation leads to a drop in pH and metals become soluble. Gully erosion pathways can cause water and air to penetrate into the inner parts of sulphide wastes promoting leaching of soluble contaminants to ground water reserves.

A series of acid-base reactions occur when the acidic water contacts carbonate, hydroxide and other base-containing solids (Cheng *et al*, 2009). This results in the formation of different pH regions that are characterized by metal-bearing hydroxide and hydrosulfate minerals (Riaza and Muller, 2009). Ferrous sulphate salts are found close to the source of pyrite and ferric sulphate salts are found away from the pyrite source where most of the Fe^{2+} has oxidized to Fe^{3+}. These secondary minerals are highly soluble and not stable at the surface (Hammarstrom *et al*, 2005).

2.1.2 Neutralisation processes

The acid produced by the weathering of sulphide minerals can be neutralized by carbonate and silicate minerals. Secondary minerals that are formed act as buffers in certain pH

ranges (Cheng *et al*, 2009). The most common carbonate minerals calcite, siderite and lime react quickly with acidic water and neutralize it according to the following reactions:

Calcite $CaCO_3 + 2H^+ = Ca^{2+} + CO_2 + H_2O$ *Equation 7*

Siderite $FeCO_3 + H^+ = Fe^{2+} + HCO_3^-$ *Equation 8*

Lime $Ca(OH)_2 + 2H^+ = Ca^{2+} + 2H_2O$ *Equation 9*

An increase in pH leads to a decrease in solubility of iron oxides and mineral precipitation of some dissolved metal hydroxides according to the following reactions:

$Al(OH)_3 + 3H^+ = Al^{3+} + 3H_2O$ *Equation 10*

$Fe(OH)_{3(s)} + 3H^+ = Fe^{3+} + 3H_2O$ *Equation 11*

$FeO(OH)_{(s)} + 3H^+ = Fe^{3+} + 3H_2O$ *Equation 12*

Silicate minerals such as Chlorite $(Mg,Fe,Li)_6AlSi_3O_{10}(OH)_8$ and Epidote $(CA_2Al_2(Fe^{3+},Al)(SiO_4)(Si_2O_7)O(OH))$ are also capable of neutralizing the acid but to a lesser extent than carbonate minerals. Weathering of silicates is controlled by pH, silica, Na, K and calcium concentration (Dold, 2005). Dissolution of silicate minerals is slower compared to metal hydroxides and carbonates minerals. Slow dissolution is the result of kinetics limitations such as limited diffusion and limited surface reactions (such as hydrolysis).

2.1.3 Microbiological activity

Microorganisms play a very important role during oxidation and reduction of sulphidic metals. Microbial populations can initiate the oxidation of metal sulphides without the presence of oxygen. Additionally, the oxidation of ferric iron to ferrous iron is accelerated by bacterial species such as *Thiobacillus ferroxidans*. Microbial populations also drive the reduction of sulphate to form sulphides. The sulphides can react with reduced iron to form iron monosulphides (FeS) which transforms after a long time to pyrite. (Hammastrom *et al*, 2005).

Iron reducing bacteria, commonly *Thiobacillus ferroxidans* is active under both oxic and anoxic conditions under a wide range of pH conditions. Reduction of sulphate and iron by microbial populations tends to increase alkalinity in acid mine drainage. When the microbial activity changes the oxidation states of Fe and S, mineralogy of iron precipitates is affected. During the oxidation of Fe (II), *Thiobacillus ferroxidans* can produce the minerals schwertmannite and jarosite at different pH ranges. With further microbial activity, these minerals will change into more stable precipitates like goethite. Microbial activity also promotes the release of cations from minerals such as biotite ($K\ (Mg,\ Fe)_3AlSi_3O_{10}(F,OH)_2$) and plagioclase ($NaAlSi_3O_8$ – $CaAl_2Si_2O_8$). Other common Fe-S oxidizing bacteria that play an important role in acceleration pyrite weathering include *Leptospirillum ferrooxidants* and Sulfolobus *acidocaldarius.*

2.1.4 Formation of efflorescent salts

The formation of efflorescent salts in acid-sulphate rich soils is very common. The salts form in banks of water courses, depressions, mud flats and in spoil heaps. Hydraulic conductivity, relative humidity and temperature are some of the factors influencing the precipitation of efflorescent minerals (Weisbrod *et al*, 2005). Evaporation from unsaturated fractures triggers capillary flow of saline water towards the surface. This results in the precipitation of salts in the form of crusts. The chemical composition of the water determines the types of minerals that will form. Under normal conditions, the sequence in which minerals precipitate is: carbonates will precipitate first, followed by sulphates and then followed by chlorides (Fitzpatrick *et al*, 2009).

Dissolution of the crusts results in episodic release of salts into groundwater reservoir or surface streams. The solubility of minerals controls precipitation at the surface. For example, as the saline groundwater moves up towards the soil surface, minerals with low solubility like gypsum

form first within the profile. More soluble minerals form on top of the surface as efflorescent. During the rainy season, increased infiltration dissolves the accumulated salt crusts.

Dissolution of efflorescent salts has adverse effects on streams and soils and these effects are well documented (Clou *et al*, 2013; Fang and Li 2010 and Harris *et al*, 2003). Depending on the strength and the amount of acid and base compounds in the salts, dissolution affect the stream pH, increases electrical conductivity and increases metal load. These effects on water and soil quality can complicate remediation efforts for acid drainage.

2.1.5 Previous research on acid mine drainage in the Witwatersrand Basin.

Coetzee *et al.* (2002) noted that untreated mine water from West Wits mines was entering Tweelopiespruit. A large volume of water began to discharge from an abandoned shaft and Coetzee *et al.* (2002) estimated an average of 15.5 ML/d mine water discharge. The water was of poor quality with high Fe, Mn, Ni, Zn, and sulphates concentrations. A pH of 3 and electrical conductivity of 362 mS/cm were recorded for the decanting water. It was later found that decanting of acidic water was not limited to the shaft at West Wits mine, but to several shafts in the area.

Naicker *et al.* (2003) studied acid mine drainage in a stream to the east of Johannesburg and reported heavily contaminated ground water reserves as a result weathering of a pyrite-rich tailings dam. They found that the seasonal fluctuation of the water table gave rise to different seepage zones. The seepage zones were found to be marked by the precipitation of limonite. Contamination levels in soil profiles were found to decrease with depth with the highest concentration occurring in the top 20 cm of the soil profile. Surface water also showed high levels of contamination by metals.

Tutu *et al.* (2008) investigated the chemical characteristics of AMD in the central part of the Witwatersrand Basin. Tailings dams, reprocessing plants and other mining infrastructure were associated with low pH levels and acidification of nearby streams, dams and lakes. Salt loads and electrical conductivity were found to be high in water bodies adjacent to the mining infrastructure. Total pollution levels varied seasonally with high pollution levels occurring in summer during the rainy season.

Nengovhela *et al.* (2006) examined the availability and the role of oxygen in gold tailings in the Witwatersrand Basin. The study reported a decreasing pattern of oxygen content with depth and oxygen depletion throughout the deeper zones. Large amounts of oxygen occur in the top 4 metres of tailings. The tailings material (mainly sand and sandy silt) determines the availability of oxygen in the impoundments. Therefore, the oxidation of sulphides and production of AMD was found to be limited in the tailings dams.

Roychoudhury and Starke (2006) studied the behaviour of trace elements in a wetland located in the East Rand to assess the impact of mining in the environment. High levels of trace elements were found in sediments. High pH values of water were attributed to the underlying dolomitic aquifer and lime treatment in the area. These conditions were found to promote the precipitation of metals whilst limiting the mobility of trace elements. Furthermore, sequential extraction experiments indicated that metals were associated with carbonates and Fe-Mn oxide phases.

Sutton *et al.* (2006) investigated the risk posed by mine residue deposits using GIS and remote sensing techniques. The study reported numerous contaminants in areas such as cultivated fields, wetlands and major water courses. Changes in contaminant secondary minerals occurred seasonally.

Weiersbye *et al.* (2006b) delineated seepage zones associated with groundwater contamination in the Witwatersrand Basin by mapping secondary minerals using hyperspectral AVRIS data.

The assessment of environmental contamination based on plant, water and soil sampling and physiochemical analysis using the above conventional methods is costly, labour intensive and time consuming. Studies by Sutton *et al.* (2006) and Weiersbye *et al.* (2006b) show remote sensing can be used as a cheaper alternative to monitor contamination in mining areas. By focusing efflorescent salt minerals as major constituents of soils, contamination patterns can be mapped and monitored.

2.2 Introduction to remote sensing for geochemical hazard assessment

2.2.1 The interaction of electromagnetic waves with minerals

In areas where little or no vegetation is present and where soil and rocks are visible, remote sensing techniques can differentiate different minerals in soils and rocks. This is because minerals absorb, reflect and or scatter the incident energy differently depending on their chemical compositions. Portions of the electromagnetic spectrum that are useful for mapping surface mineralogy include the visible and near infrared (VNIR), the short wave infrared (SWIR) and the thermal infrared (TIR) portions. Absorption features in the VNIR band are related to cation bonds and electrical processes. Absorption features in the SWIR band are related to vibration and stretching processes between water and cations. The Si-O absorption feature occurs in the TIR band (Fan *et al*, 2012). The VNIR wavelength region is useful for mapping iron oxides and hydroxides (like hematite and goethite). The SWIR wavelengths map dioctahedral and trioctahedral silicates (kaolinite, white micas, smectite, chlorites, amphiboles, talc and

serpentine) whereas the TIR wavelengths are useful for the mapping of framework silicates (quartz, feldspars, garnets, pyroxenes and olivines). Furthermore, carbonates and sulphates produce diagnostic spectral features at both SWIR and TIR wavelengths (van der Meer *et al*, 2004).

2.2.2 The spectral reflectance of minerals associated with acid mine drainage

The spectral signatures of minerals commonly found in mine-waste environments have been described in detail by Crowley *et al.* (2003) and Cloutis *et al.* (2006). The spectral signatures of some of these minerals are displayed in Figure 2-1 and can be summarised as follows:

- Copiapite: Absorption bands at 430 nm, 540 nm and 868 nm. Absorption bands near 1178 nm, 1453 nm, 1768 nm and 1941 nm are caused by molecular water and hydroxyl groups.
- Goethite: Absorption bands at 480 nm, 674 nm and 939 nm. Aluminium substitution for ferric iron shifts the position of the 939 nm absorption band towards longer wavelengths. Water related absorption features occur at 1450 nm and 1940 nm.
- Hematite: Absorption bands at 872 nm and 1930 nm. Like goethite; Hematite shows displacements of the ferric iron related to Al substitution.
- Ferrihydrite: Absorption bands at 900 nm and 600 nm. There is a marked curve into the UV region. Water related absorption bands occur near 1450 nm and 1940 nm.
- Jarosite: Absorption bands at 437 nm, 910 nm and a weak shoulder at 650 nm. Water related bands occur at 1467 nm, 1849 nm and 1936 nm and 2264 nm.

- Schwertmannite: absorption bands at 489 nm and 910 nm. Water related absorption features at 1450 nm and 1950 nm. The Schwertmannite spectrum is similar to that of Ferrihydrite.
- Carbonate minerals and efflorescent salt have absorption features at 1400 – 2500 nm.

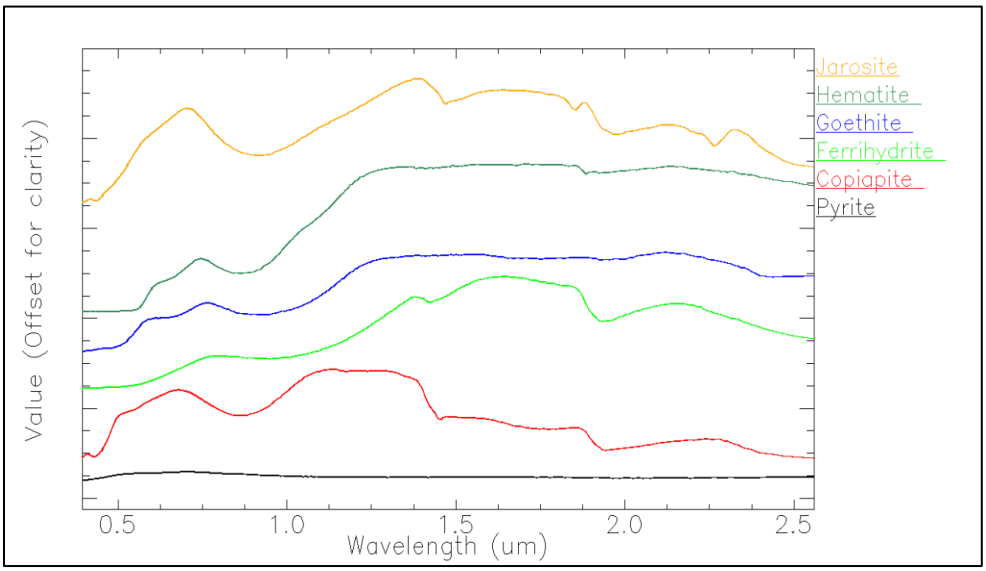

Figure 2-1 Diagnostic features in the spectra of Fe minerals (USGS spectral library)

In the Witwatersrand Basin, acid mine drainage is characterized by pyrite, calcium minerals, phyllosilicates minerals and secondary minerals like copiapite, melantirite, jarosite, ferrihydrite, Goethite and Hematite. These minerals are colourful and appear as yellow, orange and red in affected streams, river sediments and in wetlands (Figure 2-2).

A zoning pattern of iron-bearing minerals is observed around oxidised pyrite. This zoning reflects the pH of the water from which the minerals precipitated. The zones consists of a central core of original pyrite or copiapite formed under low pH conditions and grades outwards into sub concentric and commonly discontinuous zones of jarosite, goethite and hematite forming under more neutral pH conditions. Trace elements like Cd, Pb, Zn and As can become aggregated in

these minerals and their solubility is affected by acidity of the water. Minerals in zone layers are characterized by distinct and diagnostic spectral absorption features in the VNIR region of the electromagnetic spectrum (Fan *et al*, 2012; Montero *et al*, 2005).

Secondary minerals associated with acid mine drainage can be used to assess the quality of water in adjacent streams. FeOH precipitates appear dark red to red-orange in near neutral stream beds and banks. Ferryhydrite can occur in acidic and neutral environments and affect the spectral attributes of streams affected by AMD. Iron oxides forming under severely acidic conditions (pH<4) are highly reflective in the far red and the near –infrared regions. On the other hand, neutral pH, iron-rich streams show low reflectance (Ferrier *et al*, 2009). Jarosite, goethite and schwertmannite form in streams with low pH. The distribution of these minerals can be used in remote sensing to locate potential acid-producing areas.

2.2.3 Spectral characteristics of salinity

The secondary effect of shallow saline groundwater is soil salinization. Acidic saline soils (ASS) are soils affected by weathering of iron sulphide materials and are dominated by Ca, Na, Mg, K and major anions Cl^-, SO_4^{2-}, HCO_3^-, CO_3^{2-}, and NO_3^-.

In areas affected by gold mining, the most common efflorescent salts include the highly soluble melanterite, epsomite, halotrichite and copiapite groups (Giere *et al*, 2003 and Harries *et al*, 2003). Spectral reflectance of these salts on the surface is usually blurred by the presence of vegetation. The influence of salts on surface roughness can be seen in the morphological properties of minerals that they form. According to Metternicht and Zinck (2003), abundance of sodium sulphates results in the formation of puffy crusts and chlorides result in the formation of smooth saline crusts. Common salt morphological features found in the West Rand basin are

shown in Figure 2-2. The relative reflectance from the salt crusts varies according to the thickness of the crust. Reflectance of hydrated salts is characterized by sharp absorptions at the water bands and low reflectance towards longer wavelengths.

Figure 2-2 Surface features of salts in the study area

Non-hydrated salts have high reflectance in longer wavelengths. Except for alkaline soils which are dark because of organic matter, high albedo is used to differentiate saline and non-saline soils. The accumulation of saline crust increases albedo by decreasing surface roughness while moisture decreases albedo by dissolving salts (Ferifteh *et al*, 2008). According to Ferifteh *et al*, (2008) high concentrations of dissolved salts in soil result in high reflectance in the 520 mn– 900 nm regions and broad water absorption features at 1300 nm and 1650 nm. Soil electrical conductivity (EC) values greater than 4000 mS/cm cause low reflectance in the 500 nm – 2380 nm. There is an inverse relationship between EC and reflectance. Electrical conductivity increases as the reflectance decreases.

3 Materials and methods

3.1 Overview of the methodology

A diagrammatic representation of the methodology used to assess the use of hyperspectral data in detecting contamination, as well as the relationship between geochemistry and spectral data is shown in Figure 3-1. Firstly, geochemical contamination levels in different mineral precipitates are determined. Secondly, the correlation between selected geochemical variables and spectral parameters will be examined. And lastly, the modelling of geochemical variables based on reflectance spectra will be carried out. A detailed description of statistical methods and pre-processing techniques is found in Section 4.5.4.

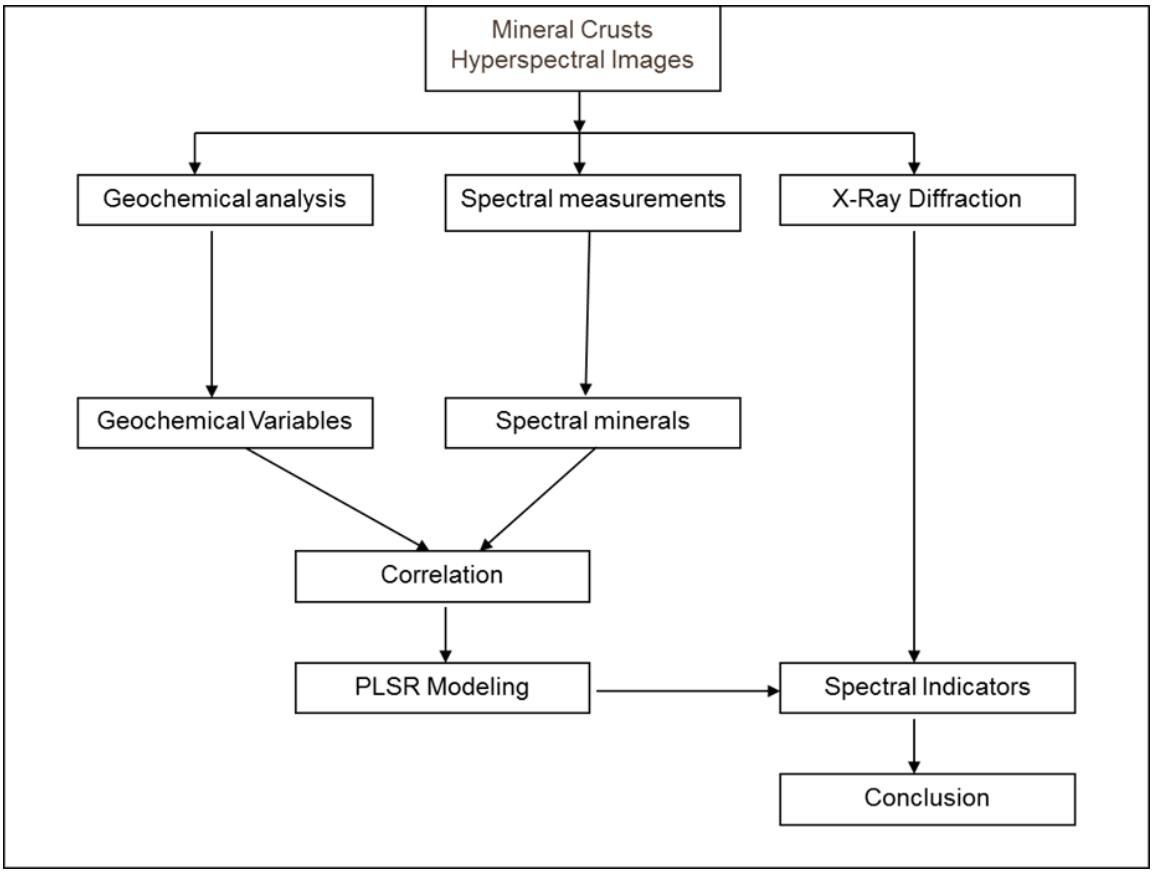

Figure 3-1 General overview of study methodology.

3.2 Sample collection

The collection of soil and mineral samples for laboratory analysis included samples from a range of soil classes and locations. To ensure that representative samples were obtained sampling material with varying colour, textural variation and proximity to tailings facilities were considered during sampling. Top 5cm of efflorescent mineral blooms were sampled, randomly along stream banks, depression hallows and excavation walls. Different land use areas like residential areas, agricultural and mining areas were also sampled. In areas were efflorescent mineral blooms are not well developed, composite soil samples were taken. Samples were selected at depths of 0 – 10 cm collecting about 100 – 200 g of sample material. The collected samples were stored in plastic bags to avoid evaporation and contamination. Sampling took place during September 2011.

The samples were subsequently dried in laboratory conditions and sieved with 100 (approximately 150 micron) mesh sieve size to remove large debris and stones. Since oven-drying affects the mineralogy of salts, the samples were air-dried for 24 hours. The drying of samples was considered to be crucial for subsequent spectral analysis since drying tends to maximize the depth of absorption features in minerals. To further concentrate the efflorescent material, the crust portion of the samples was dissolved with distilled water. The samples were subjected to evaporation at room temperature (25-30°C). After evaporation, concentrated salt crystals were stored for further analysis.

Prior to analysis, a Munsell soil colour chart (Munsell Colour, 1998) was used to characterize the colour of the samples. The characterization of the colour of the crusts was determined since colour is known to be related to the chemical composition. Organic coating leads to darker colours, iron oxides results in yellow, red and brown colours and Al-oxide-hydroxide coatings

results in white colours (Alloway, 1995). The colour of the samples varied between four major classes: Red brown, Pale Yellow, Pale Brown and Pale White.

3.3 SEM and XRD analysis

After drying, samples were crushed using a mortar and pestle to obtain a minus 75 nm fraction. The powdered samples were lightly pressed into aluminium sample holders for insertion into the X-ray diffraction (XRD) analyser, a Philips D500 diffractometer. Estimation of the relative abundances of mineral phases was made by comparing the intensities of the main peaks. Each mineral phase identified was assigned an approximate percentage of total mineral content of the sample.

The crystal structure and chemistry of salt precipitates were determined by scanning electron microscopy. The FE-SEM Zeiss Model Ultra operating at 3kV fitted with an Oxford energy dispersive X-ray detector system (EDS) was used. Dry samples were fixed on aluminium SEM plates with electronic-conductive carbon tapes.

3.4 Laboratory procedures

Geochemical analysis of precipitate samples was carried out at CGS laboratories using ICP-AES and AAS. Different classes of elements were targeted using water and four acids as digestions solutions. For quality control, analysis was performed on 3 lab duplicates. All duplicated were precise to 10%. Table 3-1 summarises laboratory analytical methods used in the study.

Partial extraction with water

The most important soil properties that influence the formation of efflorescent salts, pH and electrical conductivity were determined in the lab. Ions soluble in water like Na, Mg and Ca are good indicators of salt crust. Approximately 1 g of the sample was dissolved with 20 ml distilled water and shaken for 30 minutes and centrifuged for 15 minutes to settle down. The leachate was analysed for anions and major elements (see Table 3-1).

Total extraction digestion

The four acid method ($HF / HClO_4$ digestion) was used to target mineral phases and dissolve trace elements from crystalline phases. This method is effective in dissolving sulphide phases like pyrite. Ultra-pure water was used in the preparation of standard solutions and the final dilution of digested samples. Approximately 0.20 g of the milled sample was digested in 30 ml fluoro-polymer sample containers (with 3 ml HCl, 2 ml HNO_3, 1 ml $HClO_4$ and 2 ml HF). The digestion mixture was evaporated at various temperatures to dry the decomposition (Maritz *et al*, 2010).

Samples were diluted by adding 0.5 ml aliquot of the prepared sample solution and 9.5 ml of the prepared standard (indium and iridium) in 2% v/v HNO_3. The resultant dilution factor was 1:2000. The final volume was set to 10 ml with the final concentration of In 20 ng ml^{-1} and 30 ng ml^{-1} for Ir (Maritz *et al*, 2010). The decomposition was analysed for major and trace elements by ICP-AES.

Electrical conductivity, pH determinations and total dissolved salts

The pH and EC for the leachates were determined. The pH meter (Figure 3-2) was calibrated using pH standards 4, 7 and 9.21. After calibration, the liquid samples were shaken by hand for a few minutes. The pH electrode was immersed in the suspension and readings were recorded when the number was stable.

For electrical conductivity (EC), about 30 ml of 0.01M of Potassium chloride (KCI) solution was added to a glass beaker. The temperature was measured and adjusted while the EC electrode (Figure 3-2) was inserted into the solution. Electrical conductivity was read. Distilled water was used to rinse the electrodes between measurements.

Figure 3-2 Buffer solutions and EC-pH meter

The total dissolved salt (TDS) concentration was determined from the measured electrical conductivity. The formula used is adjusted to Witwatersrand conditions as:

$$TDS = 27.44 + 6.310 \times \text{Electrical Conductivity (mS/cm)}$$

Table 3-1 Summary of chemical laboratory procedures (Adapted from Estifanos, 2006 and Maritz et al, 2010).

Water extractable ions, pH and EC measurements			
Step	*Activity*	*Utility*	*Purpose/reason*
1	Weighing 1 g sample material		
2	Add 20 ml of deionised water		
3	Shake for 2 hours		
4	Ion Chromatography	IC (Dionex DX300)	for F, Cl, Br, NO_3, NO_2,PO_4, SO_4^{2-}
	ICP-AES	ICP-AES	As to Zr
5	Settle for an hour		
6	EC and pH measurement	EC and pH meter	electrical conductivity and pH determination
Total extraction			
1	Weighing 0.2 g of sample material	30 ml flouro-polymer sample containers	
2	Digestion with 3 ml HCI, 2 ml HNO_3, 1 ml $HCIO_4$ and 2 ml HF		Following CGS protocol
3	Evaporation	Fume wood	
4	Diluting with a standard solution (Indium and Iridium) in 2% v/v HNO_3	Calibrated bottle-top dispenser. ICP-MS	As to Zr

3.5 COLLECTION OF REFLECTANCE SPECTRA

Reflectance spectrum was collected using a portable Analytical Spectra Device (ASD) Fieldspec Pro spectrometer. The instrument covers the visible near infrared (VNIR) 350 – 1050 nm, the short wave infrared (SWIR) 1000 – 1800 nm and the SWIR 2 (1800 – 2500 nm) regions of the electromagnetic spectrum. The sampling interval for the VNIR region was 1.4 nm with a spectral resolution of 3 nm. The sampling interval for the SWIR region is 2 nm and the spectral resolution varies between 10 nm and 12 nm depending on the scan angle of the wavelength. The measured spectra can either be acquired in radiance or reflectance mode. For this study, the latter was used as the spectra can be readily checked and the quality monitored instantaneously.

All spectral measurements were taken in the laboratory under darkroom conditions which are necessary to minimize contamination by stray light. The reflected light was measured with a 25° field of view (FOV) fore optic. Prior to the collection of reflectance spectra, a reference spectrum from a white spectralon panel was taken for calibration purposes. To avoid shadows in the sample material, the light source (contact probe) was orientated perpendicular to a sample surface at a distance of 5 cm. Since interference, noise and instrument defects can affect spectral measurements, a single measurement cannot be assumed to be reliable. Therefore measurements were repeated at least three times for all the samples.

3.6 Analysis of reflectance spectra

The collected reflectance spectra were subjected to qualitative and quantitative analysis to determine mineral end-members. Qualitative analysis involved the comparison of the spectral reflectance of mineral precipitates and comparing it with the spectra of known mineral end-members (USGS spectral libraries).

To facilitate the quantitative analysis of measured spectra, the Continuum Removal (CR) algorithm was applied. Continuum Removal minimizes the effect of background absorption features thereby highlighting and isolating absorption features of interest for further analysis (van der Meer *et al*, 2004). By applying continuum removal, the effects of spectral brightness are also cancelled. The CR technique was used to normalize the spectra to make absorption features comparable. Van der Meer *et al.* (2004) compares this normalization process to fitting a rubber band over the local reflectance maxima of a spectrum where the value of the hull is adjusted to 100% reflection. Absorption values between 0 – 1 are obtained by dividing the reflectance at a certain wavelength of the absorption feature by the value of the hull at the same wavelength (van der Meer *et al*, 2004). CR normalized spectra show a flat background while different absorption features are retained.

The normalization of the spectra achieved by the CR algorithm is necessary for comparison of the spectra to other spectra taken with different instruments or under different environmental conditions. Using known mineral spectra libraries, the spectral signatures were tested against known minerals to identify end-members using ENVI 4.7 software (ITT Visual Information Solution, Boulder, Co, USA). After Continuum removal, the spectral analyst tool was used for comparison between measured spectra and spectral libraries. Spectral Analyst makes use of different algorithms to rank comparison scores of spectral information. In this study, Binary Encoding (BE), Spectral Angle Mapper (SAM) and Spectral Feature Fitting (SFF) were used to compare measured reflectance spectra to known mineral spectral libraries.

3.6.1 Quantitative absorption feature (QAF) analysis

Absorption features in the electromagnetic spectrum are related to the composition and concentration of substances in the material. Quantitative Absorption Feature (QAF) analysis makes use of the assumption that absorption features are caused by chemical and physical structure of the material (van der Meer, 2004). The QAF method works on dominant absorption features after CR normalization. After CR normalization, absorption features are characterised in terms of wavelength position, depth area and asymmetry. The absorption position (WAVE) is defined as the band having the minimum reflectance value over the wavelength range of the absorption feature. The absorption depth (DEP) is defined as "the reflectance value at the shoulders minus the reflectance value at the absorption-band minimum" (van der Meer, 2004). The width of the absorption (WID) is the full wavelength width at half DEP. The absorption area (AREA) is the area of the absorption feature that is the sum of DEP and WID.

The asymmetry of the absorption feature is defined as

$$S = A_{left}/A_{right} \qquad \textit{Equation 11}$$

Where A_{left} is the area of the absorption feature from the left shoulder to the minimum point and A_{right} is the area of the maximum point to the right shoulder of the absorption feature (van der Meer, 2004).

In numerous studies, the absorption position (WAVE), depth (DEP) and area are used for exploring features of materials (Choe *et al*, 2008). For this study, the main absorption features identified after continuum normalisation were processed to identify WAVE, DEP and AREA parameters using Dispec45 software (van der Meer *et al*, 2004).

3.6.2 First derivative reflectance transformation

A second technique for quantifying spectral parameters is by the determination of spectral derivatives. The standard first derivative is commonly used in studying physical and chemical properties of soils and rocks. The first derivative is related to the slope and length of the spectrum (Mutunga, 2004) and is derived as:

$$FDR(\lambda i) = (R_{(j+1)} - R_{(j)}) / \Delta \qquad \textit{Equation 11}$$

where FDR is the first derivative at a wavelength i midpoint between wavebands *j* and *j +1* and R *(j)* is the reflectance at wavelength *j*

- R_(j+1) is the reflectance at waveband *j+1*
- Δ_ is the difference in wavelengths between *j* and *j+1*

In the study, first derivative is used to define spectral variability. Derivative transform is useful for the identification of materials through analysis of the percentage reflectance of spectra at specific wavelength intervals. First-derivative values would be high at where the slope of reflectance values changes rapidly. In this investigation, derivatives around major absorption features (0.69, 0.98, 1.4, 1.8 and 2.2) were selected for spectral analysis. An example of first derivative transformed spectra is shown in Figure 3-3.

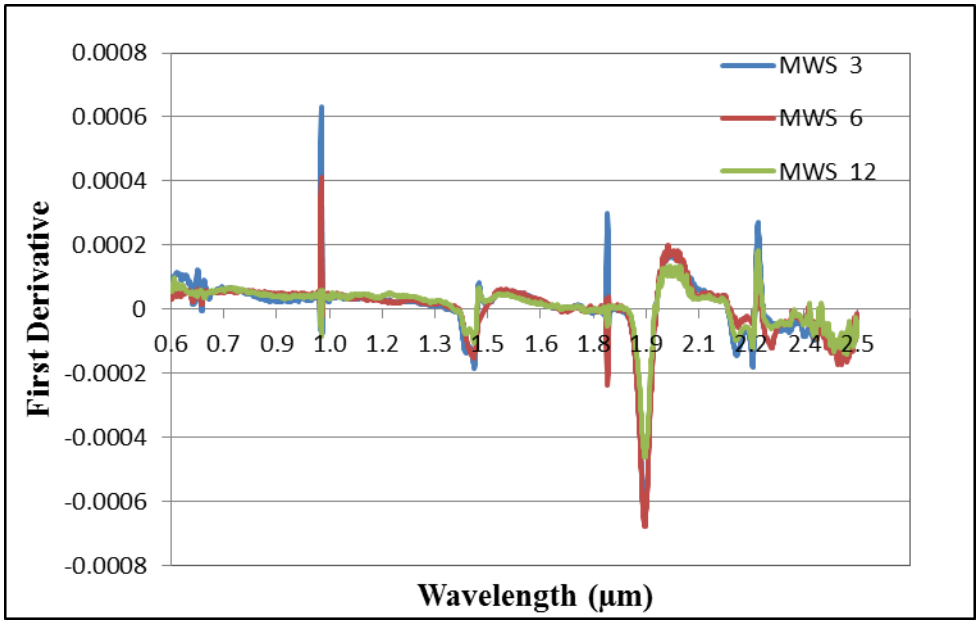

Figure 3-3 Example of first derivative spectrum for selected samples

3.7 Geochemical modelling

The results obtained from the analysis of dissolved crusts (pH, EC, metal and sulphate content) were modelled using the PHREEQC geochemical modelling code (Parkhurst and Appelo, 1999). Forward modelling based was applied to predict the evaporation sequences of the minerals. The predicted minerals were compared to those obtained by XRD, ASD and remote sensing. This way, the methods were complementary.

3.8 Statistical modelling techniques

Statistical regression models have been used to relate spectral data to chemical variables of mineral salts. In spectroscopy, regression models are used to reduce the number of spectral bands to a suitable number for modelling. Normal regression establishes relationships between X variables and Y variables. They work well with low sample numbers with no correlation between the samples. Spectral measurements using the handheld ASD instrument results in numerous

measurements that can be noisy, incomplete and strongly correlated with each other. This results in variables that are not independent from each other.

To counteract this problem, the Partial Least Square Regression (PLSR) technique, an extension of Multiple Linear Regression, which deals well with multi collinearity, large number of X-variables and simultaneously model numerous response variables, was used (Wold *et al*, 2001). In PLSR, original X variables are compressed into a few variables known as PLS components. Since fewer variables are considered, it is easier to explain the relationship between X and Y variables (Ramoelo *et al*, 2013). The results of the PLSR model can be improved by selecting the scale of variables to focus on (essentially highlighting the most important variables by giving more weight to the X variables). Several variables can be equally important and auto-scaling is the preferred standard method for selecting variables. The auto-scaling procedure standardises the variance of the variables by dividing the variable value with the standard deviation of the variable and centre it by subtracting the average. By doing so, each variable is given the same weight or same prior importance in the analysis (Wold *et al*, 2001).

When modelling chemical variables and their spectral response, the PLSR is based on the Beer Lambert Law. According to this law, there is a linear relationship between absorbance of energy and the concentration of absorbing species (Gannouni *et al*, 2012; Wu *et al*, 2007). These studies suggest that the spectral measurements would differ according to the mineral content and concentration of mine waste.

The Parles v3.1 (Viscal-Rossel, 2008) software was used to perform PLSR. Spectral parameters and geochemical variables from the analysed samples were used in the PLSR. Spectral parameters included the use of all reflectance values between 400 – 2500 nm and also value band

ratios, which are derived from specific wavelength positions. Results from the PLSR model are given as Root Mean Square Error (RMSE), Ratio of the Prediction to Deviation (RPD) and Mean and relative absolute errors (MAE). These variables assess how well the model predicts the variables. The coefficient of correlation (R^2) is also determined to indicate the statistical correlations between the measured variables and the predicted variables. Model accuracy is determined by MAE and R^2 values (Viscal-Rossel *et al*, 2006).

Geochemical and reflectance data were stored and processed in Microsoft excel spread sheets for easy management. Additional spread sheets were created to include parameters such as land use class and sample colour. Basic statistical parameters such as minimum, mean, median, maximum and standard deviation were calculated. SAS Enterprise 5.1 software was used to construct graphs and plots for visual assessment of the data. The problem with geochemical data and reflectance datasets is that it does not follow normal distribution. They are usually skewed because of severe outliers and these datasets are characterised by wide variance. Because of such distributions, non-parametric tests would be used for statistical comparison. Non-parametric tests, known as distribution free tests are suitable to these datasets because they are effective with small sample sizes and are resistant to outliers.

4 Results and discussion

4.1 Geochemical characteristics of salt precipitates

4.1.1 Descriptive statistical analysis

The chemical characteristics of the crusts are presented in Table 4-1. For comparison purposes, groundwater and tailings concentrations from the study area are also included in the table. Generally, medial values of Ni, Cr, Co, Zn, As and U were higher than the tailings and continental crust averages. Pb is the only element that recorded similar concentration to continental crust averages. Overall, the chemical results are typical of what could be expected in areas subjected to acid mine drainage and similar to those observed by other researchers who studied similar sites within the Witwatersrand Basin.

Elevated concentrations of Cr, V, Mn and Fe occurred in wetland, cultivated and bare field areas. Tailings footprints were characterised by high levels of Co, Ni, Cu and As. High levels of Cd and Cu were associated with wetlands and tailings material. Th and Zn are the only elements that showed uniform distribution in all land-use areas. High levels of Pb and Sb occurred in residential and wetland areas.

The pH values ranged from 2.65 to 8.2. Figure 4-1 shows the variation of pH values. High pH values were associated with wetland samples. Similar values have been reported by Phaleng (2009) for Blesbokspruit sediments and Roychoudhury and Starke (2006) reported a median of 8.1 for Blesbokspruit waters. Residential and cultivated areas also showed neutral to basic pH values. Low pH values (mean 2.65) were associated with tailings footprints.

Table 4-1 Statistical summary of geochemical variables (n = 29; all elements in mg kg^{-1} except for water quality in mg/l)

Variable	Min	Average	Max	Median	Water quality (average)[1]	Tailings (median)[2]	Continental Crust (average)[3]
As	4	71	956	14	-	72	1.5
Cd	0	1	14	0	3		0.10
Co	3	162	2040	38	41	26	10
Cu	8	96	646	43	-	37	25
Cr	15	241	971	153	5	273	35
Ni	15	429	5128	85	301	56	20
Pb	2	42	542	19	16	63	20
U	1	75	1110	5	8	76	2.8
V	4	92	378	53	1	40	60
Zn	22	297	1972	104	572	81	71

[1] Department of water affairs, 2012
[2] Ramontja *et al*, 2011
[3] Taylor and McLennan, 1995

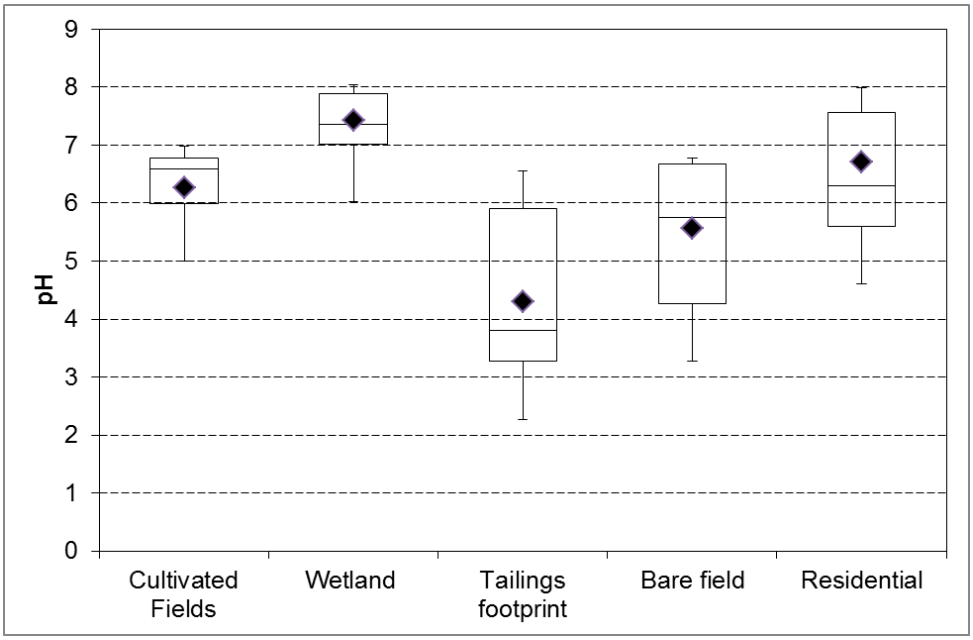

Figure 4-1 Box plots showing the variation of pH according to different land uses

The Ficklin diagram in Figure 4-2 displays a total sum of base metals against pH of analysed samples. Salts are classified into Near-neutral Extreme metal and Acid Extreme-metal. This pattern also suggests that pH exerts a major influence on the behaviour of elements. The precipitation of base metals is associated with higher pH values.

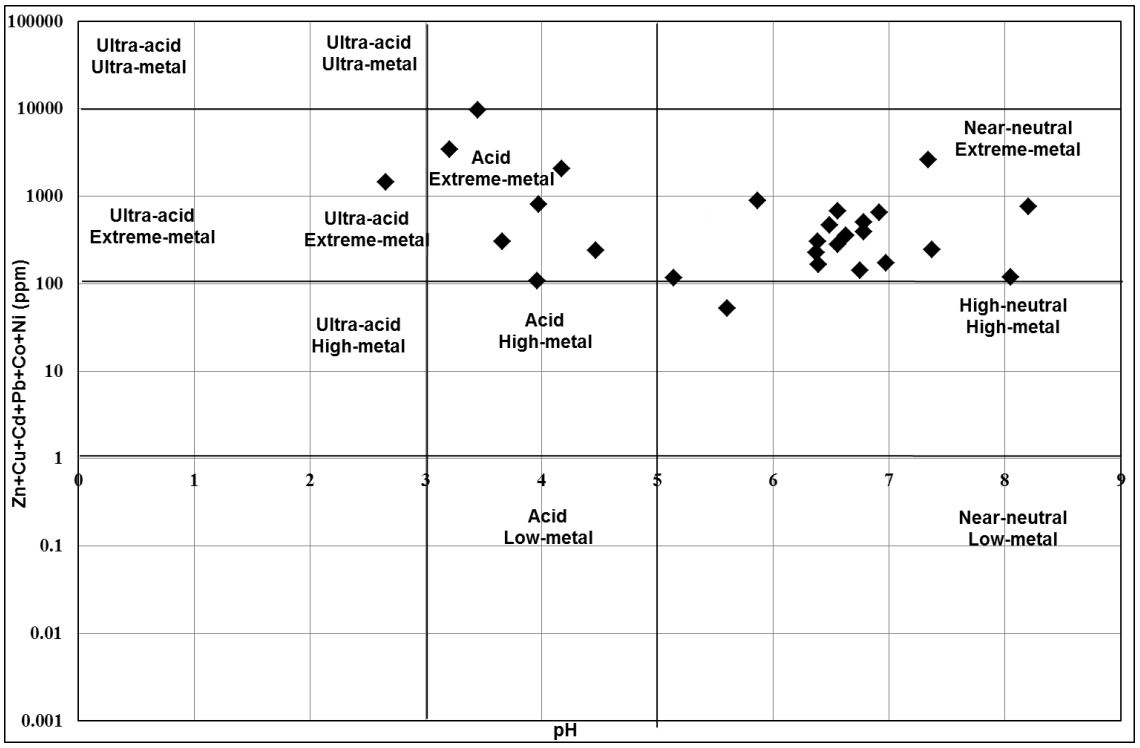

Figure 4-2 Distribution of samples in Ficklin Diagram

Figure 4-3 shows the total sum of Al, Ca, K, Mg and Na concentration over a wide range of pH values. The high concentrations of these ions are indicative of pronounced levels of weathering associated with aluminosilicates. Weathering of aluminosilicates results in the formation of buffering complexes like bicarbonates (Equeenuddin *et al*, 2010). Therefore, Figure 4-3 also indicates high neutralization potential associated with salt precipitates over wide range of pH values.

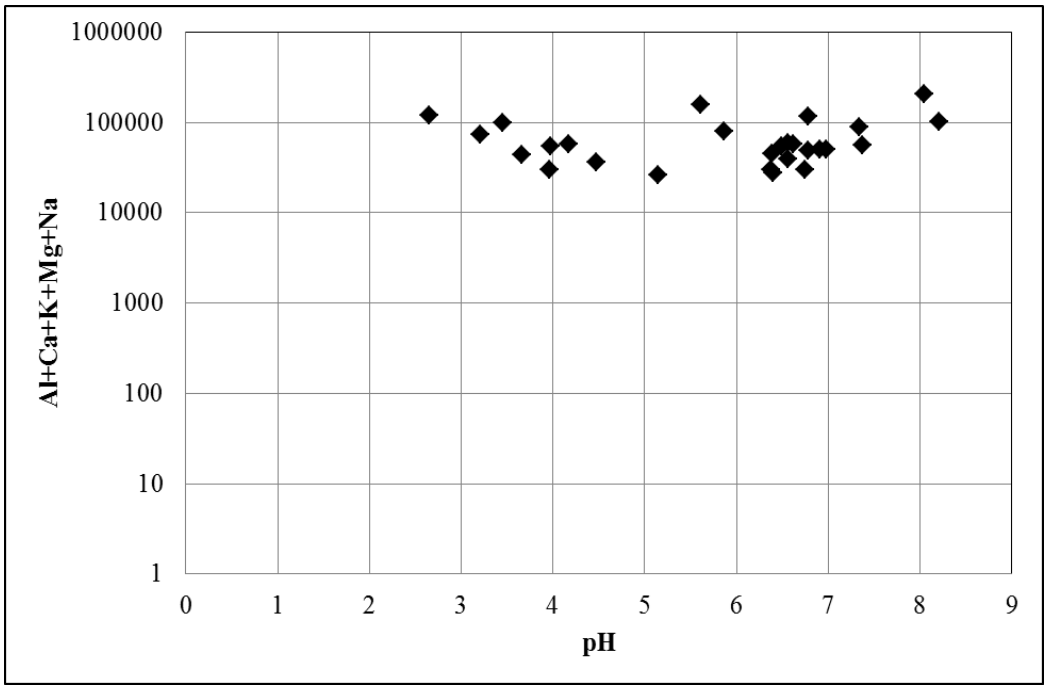

Figure 4-3 Distribution of selected major ions against pH

Figure 4-4 presents ratios of dissolved/total concentrations versus pH. The results suggest that trace metals such as Cr, Pb, As and Cu occur in particulate phases over a wide range of pH conditions. In acidic pH conditions, Co, Ni, U and Zn occur as free cationic forms.

Table 4-2 Comparison of major anions (mg kg^{-1}), EC (mS/cm) and pH in crusts to soil and water levels.

	Crusts		Tailings soil[a]		Surface Water[b]		Background Borehole water[b]	
	Mean	Median	Mean	Median	Mean	Median	Mean	Median
pH	6	6	2.9	2.6	3.1	3.2	7.2	7.3
EC	3051	1425	704	652	269	169	109	88
CI	4186	354	625	370	95	76	81	75
SO_4^{2-}	106270	25164	4902	4402	1534	742	280	183
NO_3	543	40	0.3	0.2	8.1	2.3	3.0	3.0

[a] Ramontja *et al*, 2011

[b] SRK Consulting, 2012

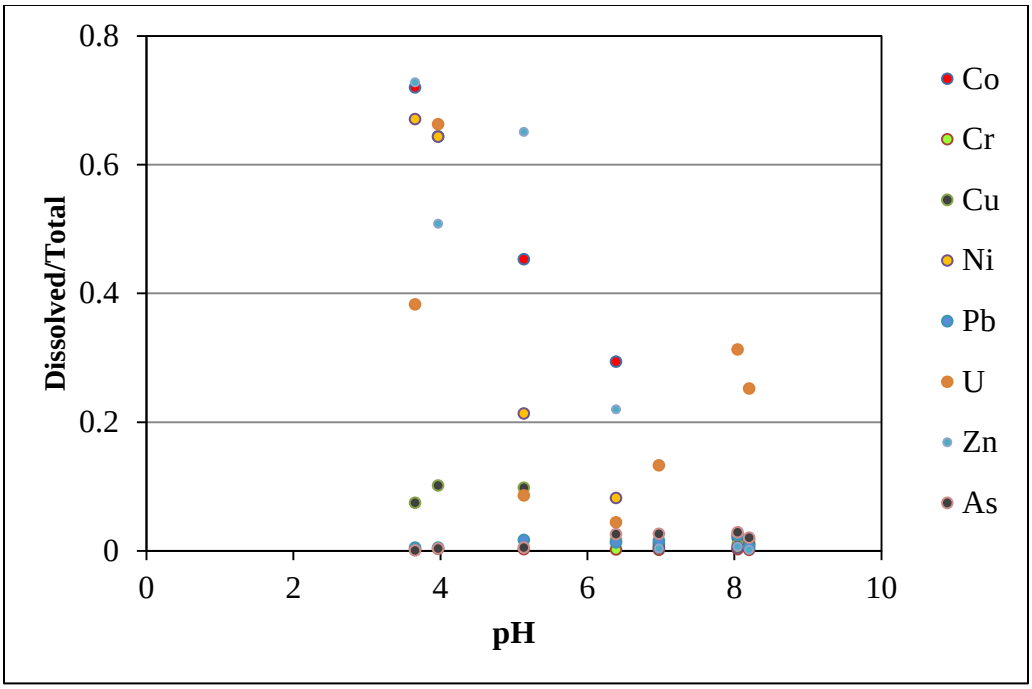

Figure 4-4 Dissolved concentrations divided by total concentrations plotted against pH for selected elements.

The distribution of electrical conductivity (EC) is presented in Figure 4-5. The EC values ranged from 21.2 to 20800 mS/cm. The mean EC value is lower than that of seepage waters recorded by Rosner and van Schalkwyk (2000). Table 4-2 shows mean concentration of EC of efflorescent salts is higher than tailings and groundwater EC concentration. High EC values were recorded where the concentration of salts was high in tailings and bare soils. High levels of electrical conductivity (EC) indicate substantial amounts of dissolved in the crusts.

Concentration of anions is shown in Figure 4-6. The presence of nitrates indicates input of organic matter in the environment (Table 4-1). In the study area, elevated nitrate (NO_2 and NO_3) levels occurred in residential and wetland areas which could be due to sewerage input and a combination of input from sewerage and plant organic matter. Phosphate showed a distribution pattern similar to that of nitrates, although low concentrations of phosphate were recorded in

cultivated soils. High levels of sulphates were associated with tailings and residential areas. Cl^- and F^- showed uniform distributions across all land-use areas.

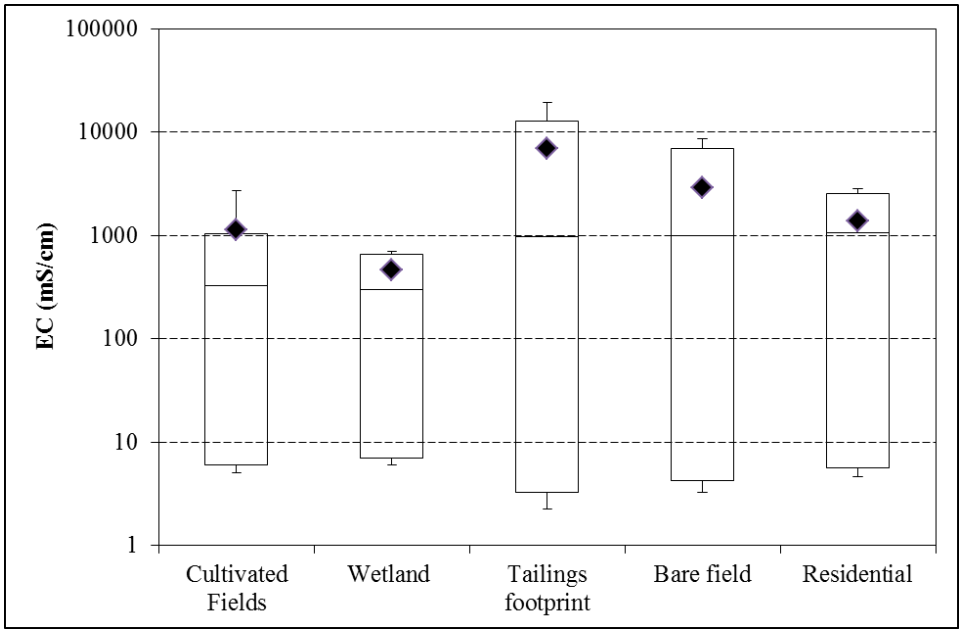

Figure 4-5 Variation of EC according to different land uses

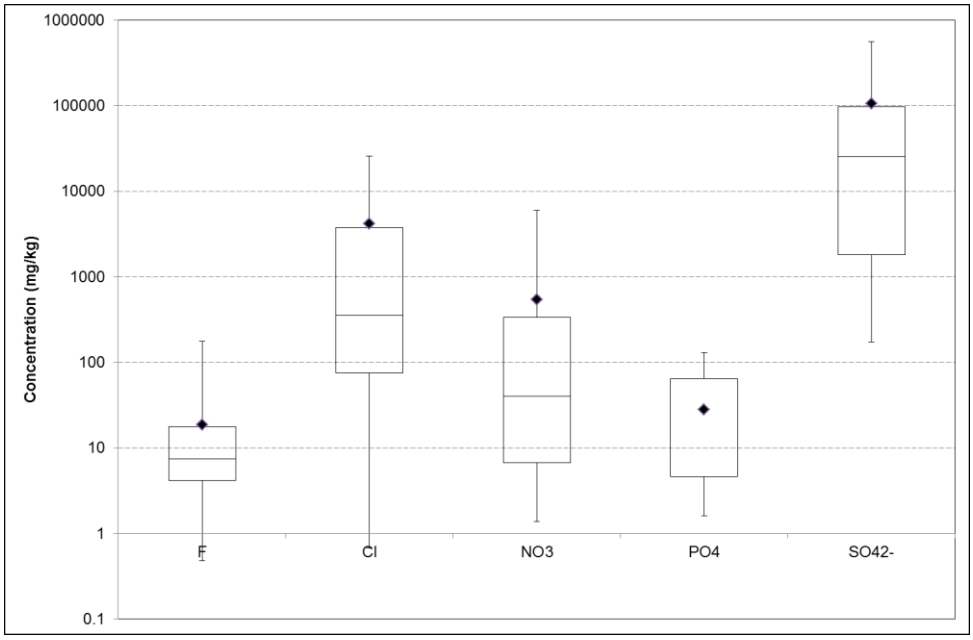

Figure 4-6 Variation of major anions in the study area

4.1.2 Multivariate statistical analysis

Results for the Spearman rank correlation are presented in Table 4-3. The results show that Na, Mg and SO_4^{2-} have significant positive correlation with EC (R^2 = 0.64, 0.52, 0.80, respectively). This correlation pattern indicates that EC can be used as a useful indicator for contamination. High correlation of Mn and Al with Co, Ni, Zn and Cd points can be interpreted as elements originating from the same mineral, possibly sphalerite, a zinc sulphide containing small amounts of Cd (Zn and Cd have similar geochemical behaviour).

The strong correlation between V, Cr, Sb, Pb and Mo with Fe demonstrates the scavenging effect of iron on highly mobile elements. Correlation strength between cations and Fe-Mn oxide is related to the fact that Mn oxide precipitates at higher pH conditions than Fe oxides, leading to high scavenging potential of Fe oxides in acidic environments (Carbone *et al*, 2013; Hammastrom *et al*, 2005). Uranium showed a strong positive correlation (R^2 = 0.63) with SO_4^{2-}. This indicates that U occurs as part of the sulphates. The pH shows a strong negative correlation (R^2 = -0.78) with SO_4^{2-}. This strong correlation can be attributed to the oxidation of sulphide minerals. High EC values are related to low pH values and the two parameters are significantly negatively correlated. According to Equeenuddin *et al.* (2010), this is because most elements are in dissolved form at low pH. There is a moderate negative correlation between Fe and SO_4^{2-}. This negative correlation indicates that oxidation of sulphide material is not a dominant process. This trend may also indicate hydrolysis of iron (Equation 4) where the precipitation of Ferric hydroxide removes iron solution. Mg, Na and Ca recorded high positive correlation with sulphate ions. Mg, Na and Ca are conservative in acid mine drainage conditions and only precipitates with sulphate ions (to form epsomite, tamarugite, thernadite and gypsum). Al showed positive correlation with sulphate. Al precipitates with SO_4^{2-} at higher pH conditions (to

form mineral alunogen). The strong correlation of Al, Mg, Na and Ca with sulphate ions suggests evaporation (precipitation) from highly concentrated brine solution (Fitzpatrick *et al*, 2009).

Graphical display of the correlation can reveal the non-conservative nature and relative attenuations of elements. Chemistry of the crusts shows that sulphate is the conservative anion because of its high concentration and is usually unaffected by precipitation and adsorption processes. Plotting the concentration of elements against sulphate and pH reveals the behaviour of elements during hydro-geochemical processes. Uranium, V, Cr, Ni and other metals showed a non-linear pattern when plotted against sulphate (Figure 4-7).

The elements (U, V, Cr, Co, Ni, Zn, Cd, Pb and Cu) are non-conservative and react rapidly with changes in hydro-geochemical conditions. Low pH values (3-4), high concentrations of Co, Ni, Zn, Cd, U, As were observed. At a pH of 8, the concentrations of these elements decreased to nearly background levels. This could be attributed to their precipitation and co-precipitation with Fe. Cr and V, on the other hand showed the opposite trend (Figure 4-4). These elements are known to form soluble complexes at high pH. Uranium also behaves similarly, but it is not very apparent why its behaviour is different in this case.

Table 4-3 Spearman correlation analysis for elements in mineral salts

	Na	Mg	Ca	V	Cr	Mn	Fe	Co	Ni	Cu	Zn	Mo	Cd	Pb	U	As	Sb	Th	Cl	NO_3^-	PO_4^{3-}	SO_4^{2-}	pH
Na																							
Mg	0.67																						
Ca	0.31	0.46																					
V	-0.42	-0.50	-0.10																				
Cr	-0.36	-0.55	-0.22	0.89																			
Mn	0.20	0.21	-0.11	0.21	0.14																		
Fe	-0.22	-0.45	-0.09	0.88	0.85	0.27																	
Co	0.21	0.22	-0.17	0.15	0.21	0.86	0.29																
Ni	0.27	0.40	-0.01	0.08	0.18	0.72	0.20	0.92															
Cu	-0.02	0.01	-0.25	0.46	0.60	0.63	0.46	0.77	0.80														
Zn	0.26	0.37	-0.02	-0.05	-0.02	0.67	0.00	0.68	0.73	0.60													
Mo	-0.19	-0.26	0.15	0.76	0.76	-0.07	0.65	-0.22	-0.15	0.33	-0.16												
Cd	0.23	0.32	-0.05	-0.05	0.03	0.66	0.05	0.74	0.78	0.65	0.93	-0.18											
Pb	-0.11	-0.30	0.09	0.53	0.65	0.19	0.59	0.15	0.22	0.53	0.25	0.67	0.29										
U	0.32	0.35	-0.17	-0.37	-0.14	0.27	-0.22	0.54	0.62	0.39	0.52	-0.49	0.58	-0.03									
As	-0.03	-0.30	-0.14	0.23	0.43	0.08	0.48	0.26	0.26	0.22	0.08	-0.04	0.16	0.35	0.38								
Sb	-0.27	-0.46	0.14	0.64	0.75	-0.03	0.70	-0.05	-0.01	0.32	-0.03	0.75	-0.01	0.81	-0.27	0.43							
Th	-0.26	-0.27	-0.10	0.62	0.73	0.12	0.62	0.19	0.25	0.58	0.24	0.62	0.26	0.65	0.07	0.36	0.62						
Cl-	0.71	0.60	0.33	-0.50	-0.54	0.08	-0.35	-0.03	0.01	-0.24	0.18	-0.23	0.16	-0.10	0.06	-0.35	-0.30	-0.35					
NO_3^-	0.22	0.08	0.01	0.21	0.34	0.43	0.27	0.48	0.47	0.60	0.36	0.20	0.34	0.50	0.14	0.17	0.41	0.24	0.15				
PO_4^{3-}	0.04	0.14	0.08	-0.11	-0.02	0.35	0.02	0.30	0.32	0.27	0.41	-0.03	0.48	0.34	0.05	0.13	0.24	0.09	0.15	0.48			
SO_4^{2-}	0.73	0.72	0.19	-0.71	-0.60	0.22	-0.55	0.30	0.36	-0.04	0.37	-0.58	0.34	-0.33	0.63	-0.06	-0.53	-0.35	0.54	0.02	0.07		
pH	-0.34	-0.14	0.33	0.47	0.21	-0.01	0.22	-0.30	-0.28	-0.05	-0.05	0.57	-0.17	0.25	-0.70	-0.53	0.35	0.16	-0.06	-0.03	0.00	-0.57	
EC	0.64	0.53	0.16	-0.54	-0.40	0.29	-0.28	0.45	0.40	0.05	0.26	-0.49	0.32	-0.18	0.57	0.24	-0.35	-0.25	0.43	0.26	0.33	0.79	-0.72

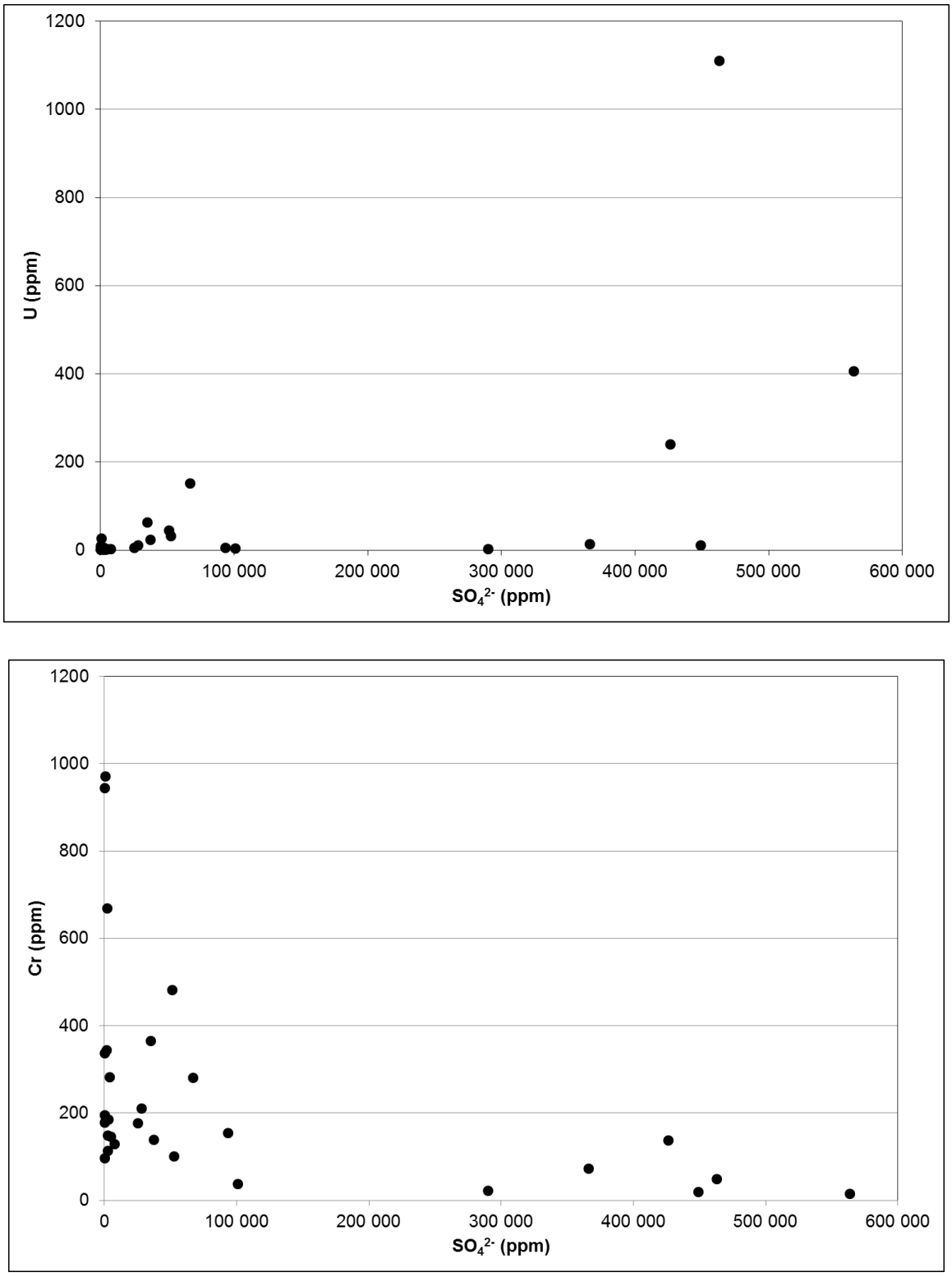

Figure 4-7 Relationship between sulphate and selected elements

Oxidation of sulphide material is usually followed by buffering action of calcium carbonate which controls the concentration of calcium and sulphate ions. The presence of dolomite in the area also contributes significantly to the buffering capacity in the samples.

According to Equeenuddin *et al.* (2010), the reaction of sulphide oxidation and carbonate buffering is consistent with a Ca^{2+}/SO_4^{2-} molar ratio of 2. Figure 4-8 shows Ca^{2+}/SO_4^{2-} ratio for most samples is less than 2, indicating that the are other mechanism affecting Ca and SO_4^{2-} other than calcium buffering reaction.

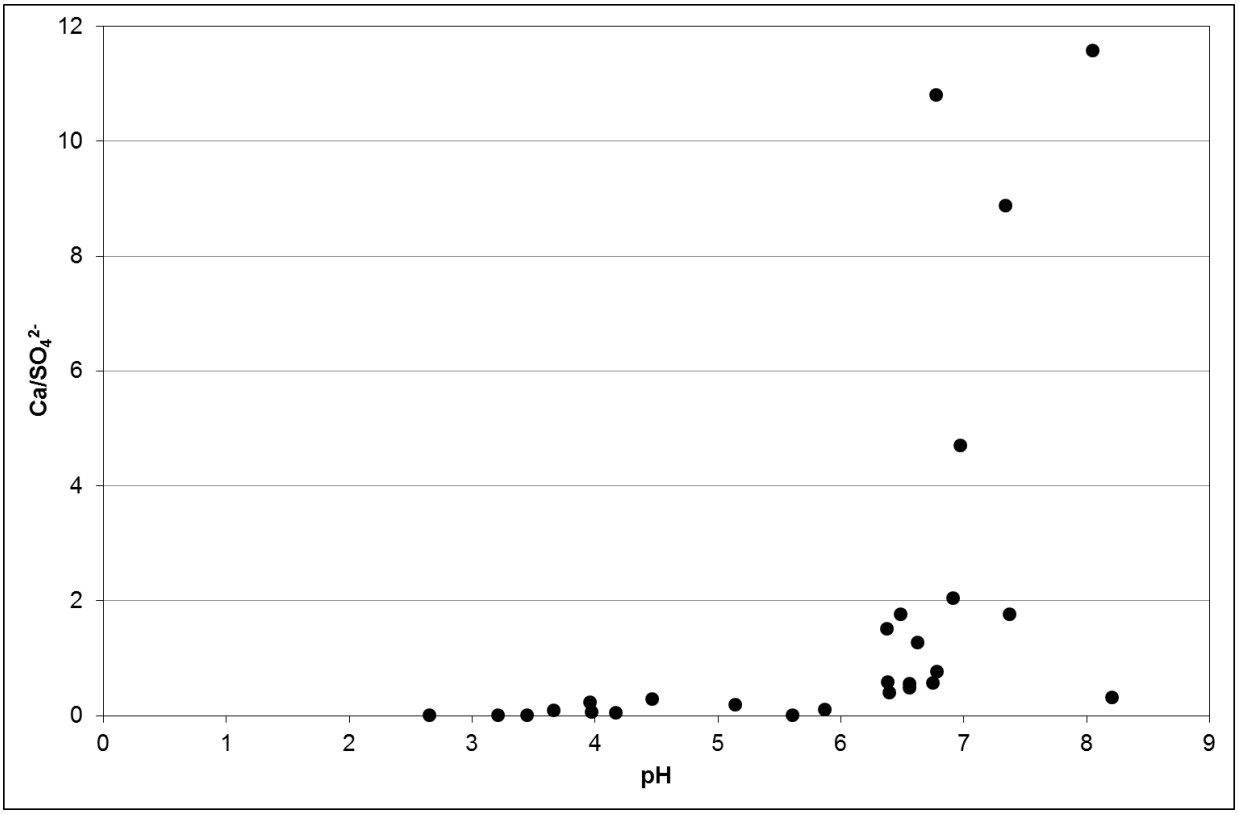

Figure 4-8 Ca/SO_4 ratio plotted against pH

4.1.3 Effect of land use and sample colour on the total concentration of elements

The Krustal-Wallis (ANOVA) test was used for comparison where there were more than three groups. Statistical analysis of the geochemical dataset and reflectance datasets was performed to determine differences between 1) different land use areas and the concentration of elements, and 2) colour of the samples and the concentration of elements.

A 95% level of significance was used for testing, meaning a *p-value* less than 0.05 was considered significant. Krustal-Wallis (ANOVA) test results are shown in Table 4-4. Geochemical variables V, Cr, Sb, SO_4^{2-}, and pH show statistical significance with land use. All other geochemical variables have p-values more than 0.05 meaning the difference between the means is not big enough to be considered statistically significant. pH is the geochemical variable with the lowest p-value. V, Cr, Co, U, As, SO_4^{2-}, pH and EC showed different levels among different colours (Table 4-4). For Co, U, As, SO_4^{2-}, pH, EC, Ni, high mean values are associated with white samples and V and Cr showed high mean values in red/yellow samples (Figure 4-9).

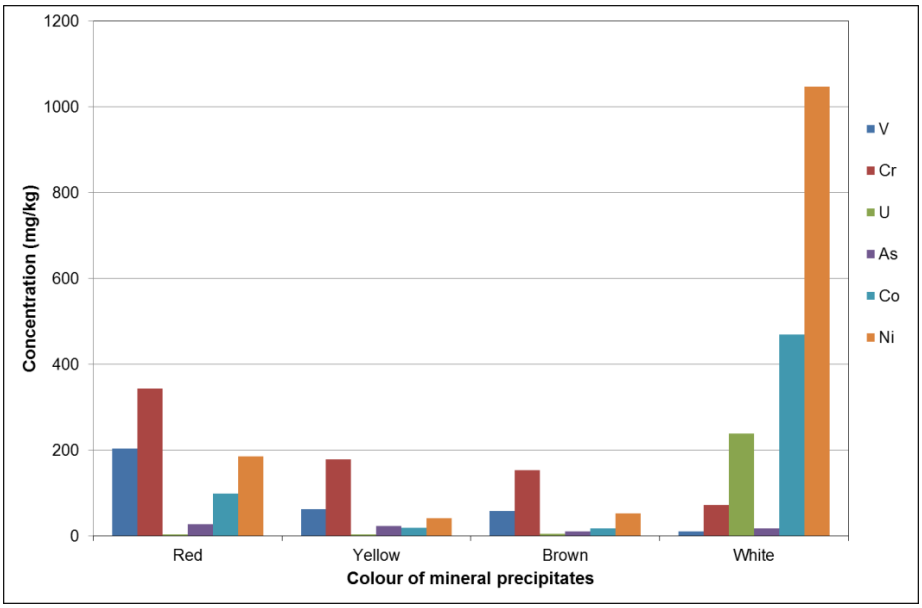

Figure 4-9 Median values of selected elements in different salt precipitates

Table 4-4 Results (p-values) of comparison between land use and colour (α = 0.05)

Element	Land-use	Colour	Element	Land-use	Colour
V	**0.0294***	**0.0202***	As	0.3866	**0.0363***
Cr	**0.0257***	**0.0109***	Sb	0.0908	**0.0018***
Co	0.3045	**0.0025***	Cl	0.71	0.6042
Ni	0.3439	**0.0043***	NO_3	0.5585	0.4381
Cu	0.3393	0.2176	PO_4	0.6068	0.4287
Zn	0.44	0.0865	SO_4^{2-}	0.0976	**0.0092**
Pb	0.1214	0.069	pH	**0.0053**	**0.0028**
U	0.3343	**0.0056***	EC	0.1049	**0.0112**

4.2 Geochemical assessment of contamination levels

Several methods were used to assess the quality of the collected crusts. Firstly, the results of the chemical analysis of soil crusts were compared to the results of the chemical analysis of the mine waste residues as well as groundwater. Enrichment factors and geochemical indices were determined to establish the degree of contamination.

4.2.1 Enrichment factors

An enrichment factor (EF) is used to quantify the level of contamination of the environment. It is a ratio that describes the magnitude at which the contaminant is enriched above what is considered background value. This ratio is defined as:

$$Ef = \frac{(M/R)_{sample}}{(M/R)_{background}}$$ *Equation 12*

where M is metal concentration and R is concentration of a reference element.

The appropriate reference metals are those not subjected to contamination by human sources. An element qualifies as a reference if it is of low occurrence variability and is present in the environment in trace amounts. Scandium (Sc) was chosen as reference element. A subsoil sample from an adjacent bare field was taken as a reference point and was used for EF calculations.

Elements which are naturally derived from the environment have enrichment values of nearly 1, while elements affected by human activities have enrichment values of greater magnitudes. If the EF of an element is greater than 1, this indicates that a contaminant is more abundant in soil relative to its regional background abundance (and may indicate human influences). If the EF values are greater than 5, they are considered to be contaminated with related metals (Loska *et al*, 2004). Table 4-7 shows contamination levels according to EF indices. As the EF values increase, the contributions of the anthropogenic origins also increase (Loska *et al*, 2004).

Table 4-5 Classes of contamination by metals according to EF indices

Value	**Degree of Contamination**
< 2	deficiency to minimal
2--5	moderate enrichment
5--20	significant enrichment
20--40	very high enrichment
>40	extremely high enrichment

Calculated EF values are presented in Figure 4-10. The majority of the elements show moderate to significant enrichment. There is a very high enrichment for Cr, Co, Ni, Cu, Zn, Cd and Th. The metal enrichment factors in mineral crusts follows the order Cd> Zn> Co> Ni> Cu> Th> Cr > Mo > V> Pb> U.

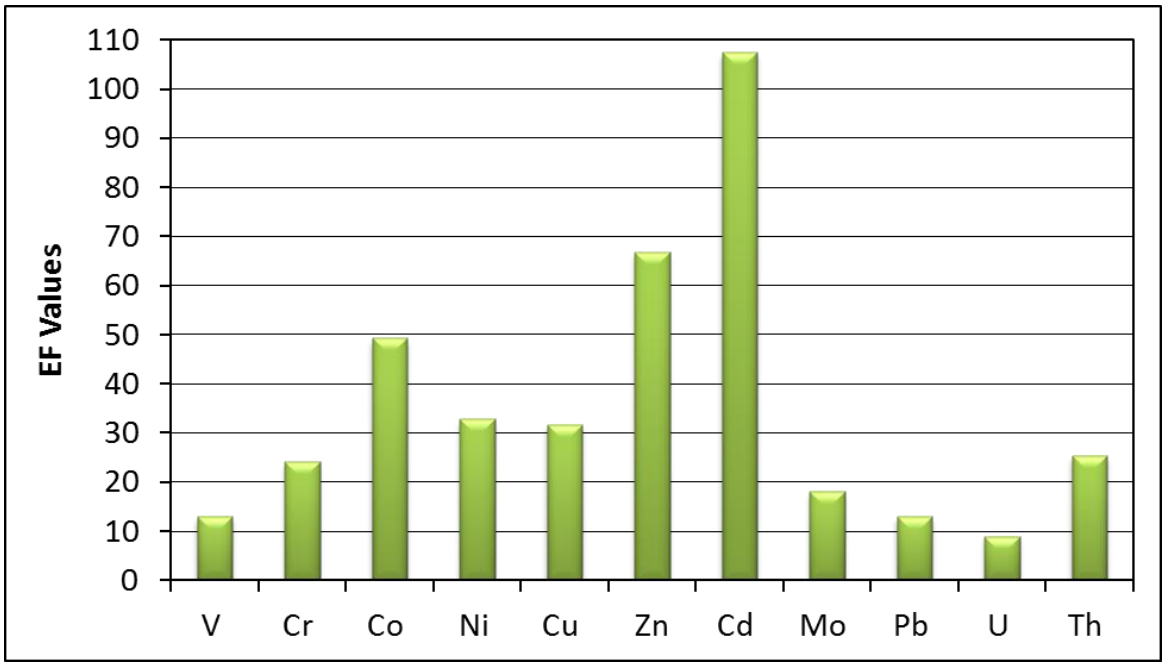

Figure 4-10 Variation of EF values for selected element

4.2.2 Index of Geo-accumulation

The geo-accumulation index is used to evaluate metal accumulation in sediments when compared to the background. This index measures the degree of contamination by a metal and is calculated as follows:

$$I_{geo} = Log_2 \ (C_n / 1.5 \times B_n) \qquad \textit{Equation 13}$$

where C_n is the total concentration and B_n is the background value.

Natural variation of the background value is adjusted by the factor of 1.5 (Kalebder and Ucar, 2013). The average concentrations of borehole soils from the Witwatersrand Basin were taken as geochemical background values.

Table 4-6 Classes of contamination by metals according to Igeo indices

Value	Degree of Contamination
0	Unpolluted
0 - 1	Unpolluted to moderately polluted
1--2	Moderately polluted
2--3	Moderately to highly polluted
3-- 4	Highly polluted

Calculated Igeo values are presented in Figure 4-11. Igeo values greater than 5 were obtained for Co, Ni, Cu, Zn, Cd, Pb and U, indicating metal enrichment in precipitate samples. The remainder of the elements fell into class 1, indicating no pollution to moderate pollution.

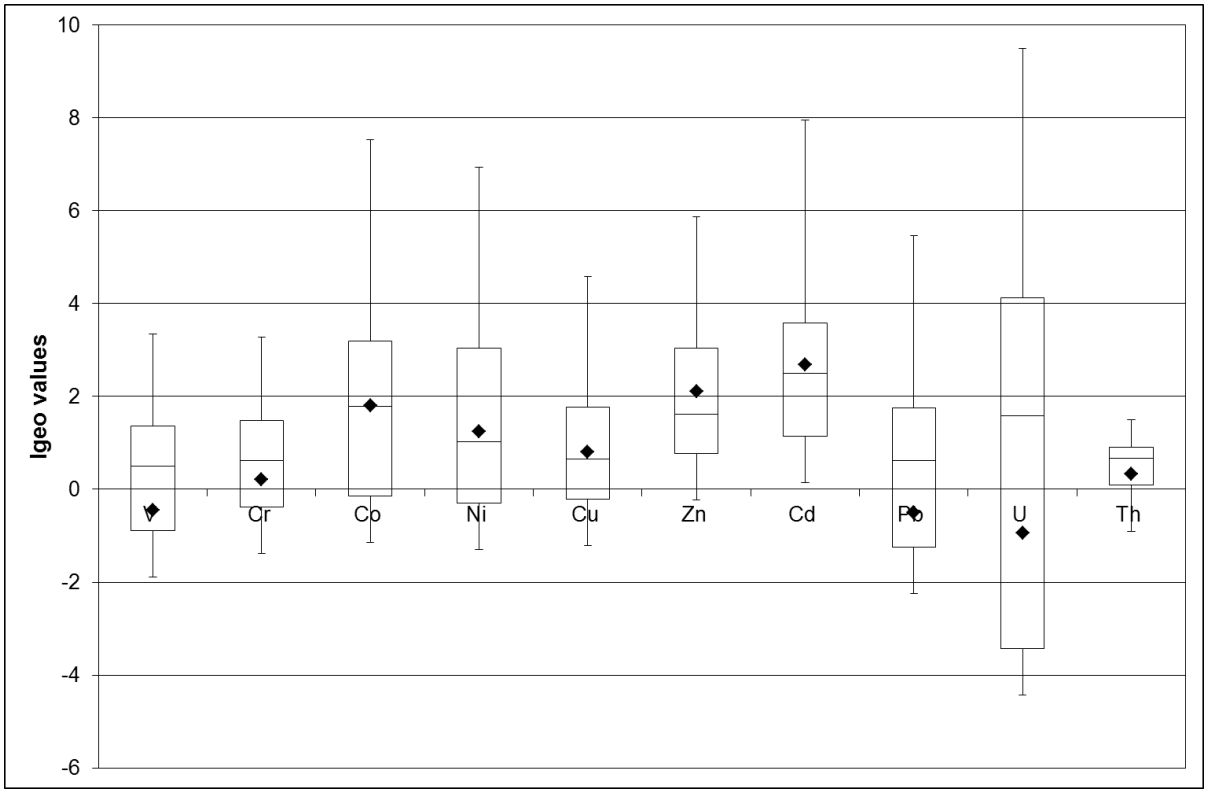

Figure 4-11 Variation of Igeo for selected elements

4.2.3 Pollution Load Index

The contamination factor (CF) is used to quantify the level of contamination by a metal. The contamination factor is ratio of metal concentration and background metal. Contamination factor is expressed as:

$$CF = \frac{Concentration\ of\ a\ metal}{Background\ value\ of\ metal}$$ *Equation 14*

Pollution Load Index (PLI) is used to define the total contamination effect of the metals. This index is the geometric mean of the concentration of different trace metals present in the study area. It is expressed as:

$$PLI = \sqrt[n]{Product\ of\ n\ number\ of\ CF\ values}$$ *Equation 15*

Where CF is the contamination factor and *n* is the number of metals (Kalender and Ucar, 2013).

Table 4-7 Classes of contamination by metals according to PLI indices (Kalender and Ucar, 2013)

PLI Value	**Degree of Contamination**
>1.5	Nil to very low
1.5-2	Low
2--4	Moderate
4--8	High
8--16	Very High
16--32	Extremely High
>32	Ultra high

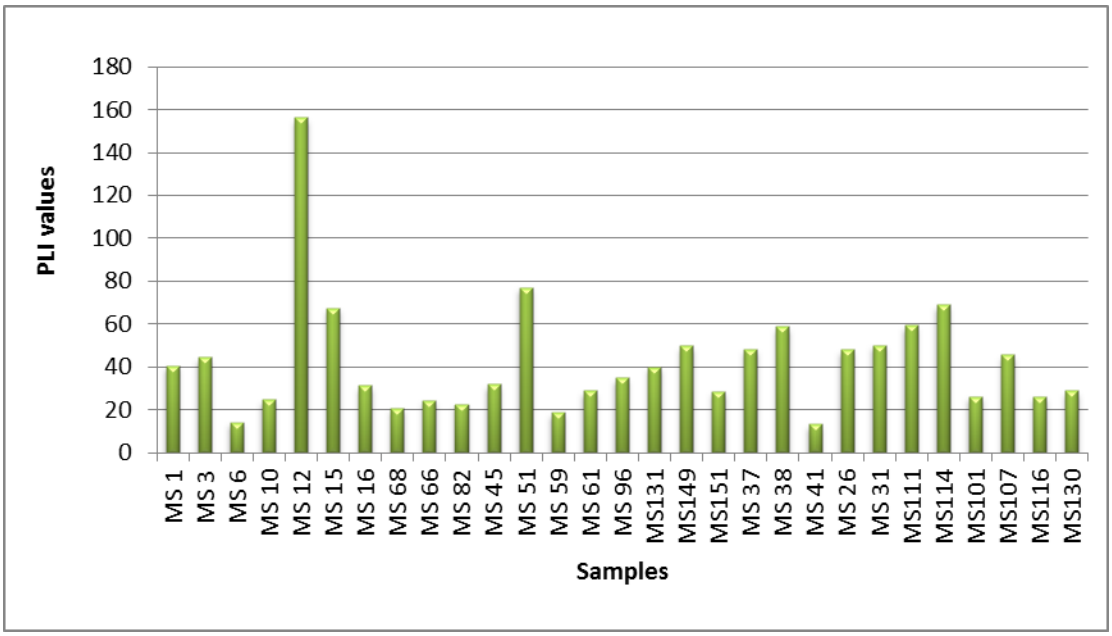

Figure 4-12 Variation of calculated PLI values

Variation of calculated PLI values is shown in Figure 4-12. Calculated PLI values ranged from 14 to 156 indicating extremely high contamination levels in all sampling sites. Extremely high PLI values were associated with wetlands and bare fields samples. Variation of PLI showed a similar trend to that of EC, SO_4^{2-} and to a lesser extent pH.

4.3 Mineralogy and geochemical modelling

4.3.1 X-ray diffraction and SEM mineralogical phases

Representative samples from all four types of precipitates were analysed for mineralogical composition. The XRD is a semi- quantitative method; it does not have the exact quantification limit (LOC). A total of 12 precipitates were analysed by X-Ray diffraction and

the results accuracy ±5% are presented in Table 4-8. The main aim of mineralogical analysis was mineral identification and not for mineral quantification.

Table 4-8 X-ray diffraction mineral weight percentage for selected mineral precipitants

Mineral	Ideal Formula	MWS 31	MWS 32	MWS 40	MWS 44	MWS 59	MWS 66	MWS 82	MWS 101	MWS 131	MWS 147	MWS 149	MWS 151
Gypsum	$CaSO_4 \cdot 2H_2O$	Trace	Trace	3	7	Trace	-	5	Trace	-	2	Trace	4
Quartz	SiO_2	5	2	4	27	86	Trace	88	96	16	77	85	87
Kaol/Chlor/Mica	$Al_2Si_2O_5(OH)_4$ / ClO_2	-	-	-	-	11	-	7	-	10	13	12	6
Jarosite	$KFe^{3+}3(OH)_6(SO_4)2.$	-	-	2	-	Trace	-	-	3	-	8	2	2
Alunogen	$Al(H_2O)_6]_2(SO_4)_3 \cdot 5H_2O$	-	2	-	2	-	-	-	-		-	-	-
Hexahydrite	$MgSO_4 \cdot 6H_2O$	9	20	58	-	Trace	-	Trace	-	-	-	-	-
Blodite	$Na_2Mg(SO_4)_2 \cdot 4H_2O$	-	-	33	-	-	-	-	-	-	-	-	-
NH-Mn Fluoride	$(NH_4)_2(MnF_6)$	23	-	-	-	-	12	-	-	40	-	-	-
Apjohnite	$MnAl_2(SO_4)_4(H_2O)_{22}$	19	23	-	63	-	87	-	-	34	-	-	-
Tamarugite	$NaAl(SO_4)_2(H_2O)_6$	42	52	-	-	-	-	-	-	-	-	-	-

The results of the mineralogical analysis are presented in Table 4-8 can be summarized as follows:

Silicate minerals

The dominant mineral in all precipitates is quartz. The content of quartz ranged from 1 wt. % to 96 wt. % and high quartz content is associated with red and yellow precipitates. Feldspar minerals micas and microcline ranged from 1 wt. % to 10 wt. % in red and yellow crusts. Altered mica in the form of serpentine was detected in white crusts with a concentration of 5 wt. %. Additionally, kaolinite and chlorite were also detected. In all the samples, the concentration of

these clay minerals was 5 wt. % or lower. The other portion of clay minerals remained undifferentiated, and is reported as Interstratification.

Sulphate and sulphide minerals

Chalcopyrite, pyrite, and other dominant minerals in the tailings storage facilities and mineralized ore body were not detected in the mineral efflorescent crusts. Jarosite was the most common sulphate mineral in the samples. Jarosite ($KFe\ (SO_4)_2\ (OH)_6$) concentration ranged from 1 wt. % in MWS 59 to 8 wt. % in MWS 147. Gypsum is another dominant mineral with a concentration range of 1wt. % to 7wt. %. Trace amounts of gypsum occurred in MWS 59, MWS 66, MWS 101 and MWS 131. In all the samples, gypsum was found to be occurring with jachymovite, a uranium sulphate mineral. Jachymotive ($((UO_2)_8(SO_4)(OH)_{14} \bullet 13H_2O$) occurred in traces and it is not reported with the main results. Hexahydrite ($MgSO_4 \bullet 6H_2O$) was found in high concentrations, ranging from 1 wt. % to 58 wt. % with white crusts containing approximately 20 wt% and brown crusts containing about 58 wt. % hexahydrite. Apjohnite ($MnAl_2\ (SO_4)_4(H_2O)_{22}$) is a manganese aluminium sulphate salts that occurred in high concentrations in white mineral crusts only. Its concentration ranged from 20 wt. % to 87 wt. %. Tamarugite ($Na\ Al\ (SO_4)_2(H_2O)_6$), a sodium aluminium sulphate was associated with apjohnite and occurred in concentrations that ranged from 42 wt. % to 52 wt. %. Tamarugite and apjohnite in samples MWS 31, MWS 32, MWS 44, MWS 66 and MWS 131 is associated with high contents of Cd, U, Ni and As. Fibroferrite ($Fe(OH)(H_2O)_2SO_4$) is another sulphate mineral that was detected at low concentrations of 3 wt. %. Other sulphate minerals found at low concentrations include alunogen ($Al_2\ (SO_4)_3 \bullet 17H_2O$) and blodite ($Na_2Mg\ (SO_4)_2 \bullet 4H_2O$).

Other minerals

Hematite and goethite were only detected in one sample and at low concentrations of about 3 wt. %. Aragonite is the only carbonate mineral that was detected in low concentrations of 1 wt. % or lower. The most diverse mineral compounds detected are Fluellite ($Al_2PO_4F_2$ $(OH)(H_2O)_7$) and Ammonium Manganese Fluoride ($(NH_4)_2(MnF_6)$). These minerals are associated with white mineral salts and are occur in high concentrations ranging from 5 wt. % to 40 wt. %.

In addition to XRD analysis, the mineral crusts were subject to analysis by Scanning Electron Microprobe (SEM) analysis.

Na-Mg bearing sulphates

Blodite (Na_2Mg $(SO_4)_2$ $\bullet 4H_2O$) and picromerite (K_2Mg $(SO_4)_2$ $\bullet 6H_2O$) are the dominant minerals in white samples. Blodite is not well crystallized, and occurs as fine grained material. Blodite also forms tubular or lath-shaped crystals in a tamarugite matrix. Picromerite shows a prismatic structure and is associated with halite and hexahydrite.

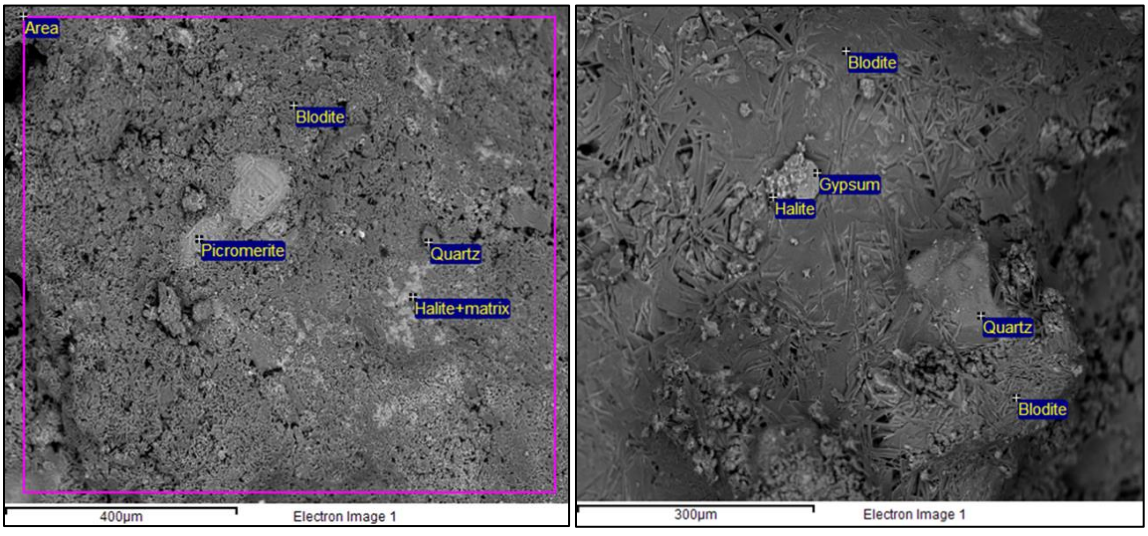

Figure 4-13 SEM images of Blodite and Picromerite

Mg-bearing sulphates

Hexahydrite ($MgSO_4 \bullet 6H_2O$). and wupatkiite ($(Co,Mg)Al_2 (SO_4)_4 \bullet 22H_2O$) are the dominant Mg-sulphates in all salt precipitates. Hexahydrite shows thick short crystal that looks blocky. Hexadrite also occurs as fine grains between Mn-Mg-sulphur matrix. Wupatkiite shows feathery crystals intergrown with hexahydrite. Wupatkiite crystals form aggregates of curved crystals that show light and dark colour shades. Alunogen was present in colloidal form.

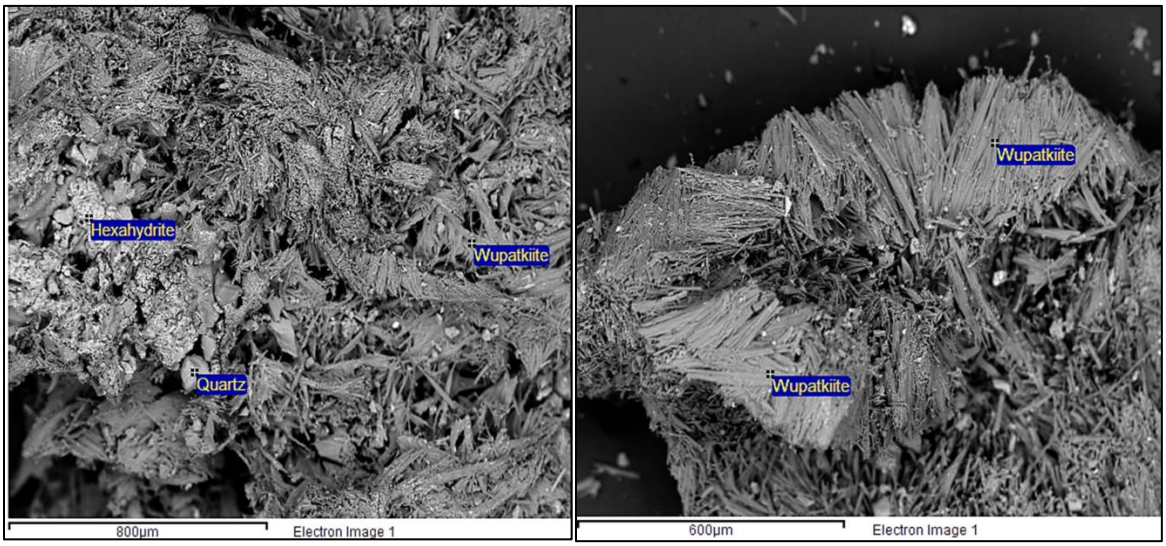

Figure 4-14 SEM image of Wupartkiite and Hexahydrite

Al bearing sulphates

Tamarugite ($Na\ Al\ (SO_4)_2(H_2O)_6$) and apjohnite ($MnAl_2\ (SO_4)_4(H_2O)_{22}$) are the dominant Al-sulphates in the samples. Tamarugite shows compact, platy crystals and it is also recognised as intergrowths in apjohnite and hexahydrite matrix. Apjohnite shows thin needle-like crystals forming fibrous aggregates.

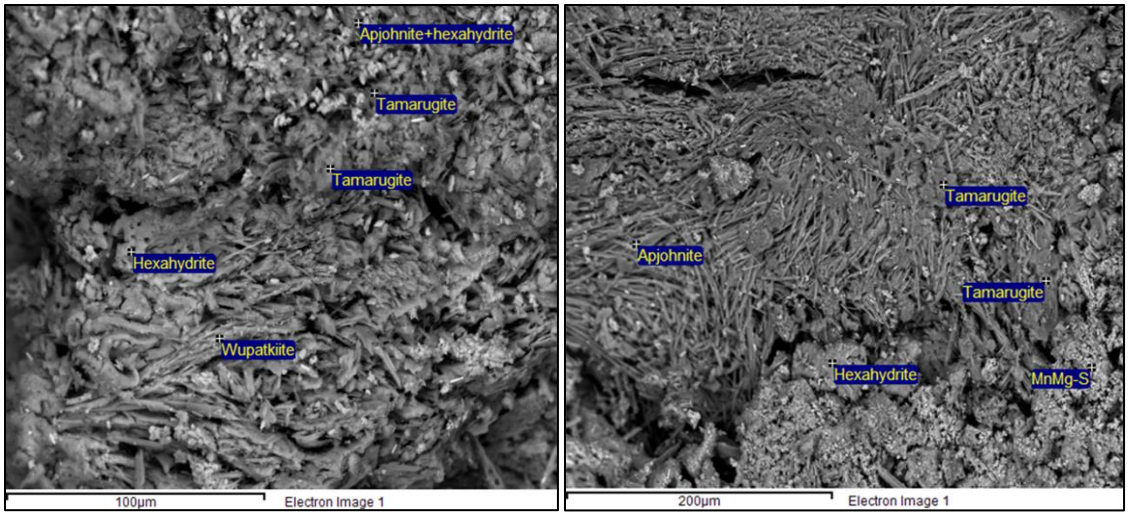

Figure 4-15 SEM images of Tamarugite, Apjohnite with Mn-Mg-S matrix
Fe bearing sulphates

Jarosite ($KFe(SO_4)_2(OH)_6$) appears to occur in colloidal form and it is not well crystallized. SEM images indicate colloidal iron that has not crystallized. Jarosite is associated with platy crystals of mica minerals (muscovite appears to be covered with iron). Jarosite also occurs as coating gypsum grains. High iron content associated with jarosite indicates the presence of iron hydroxides.

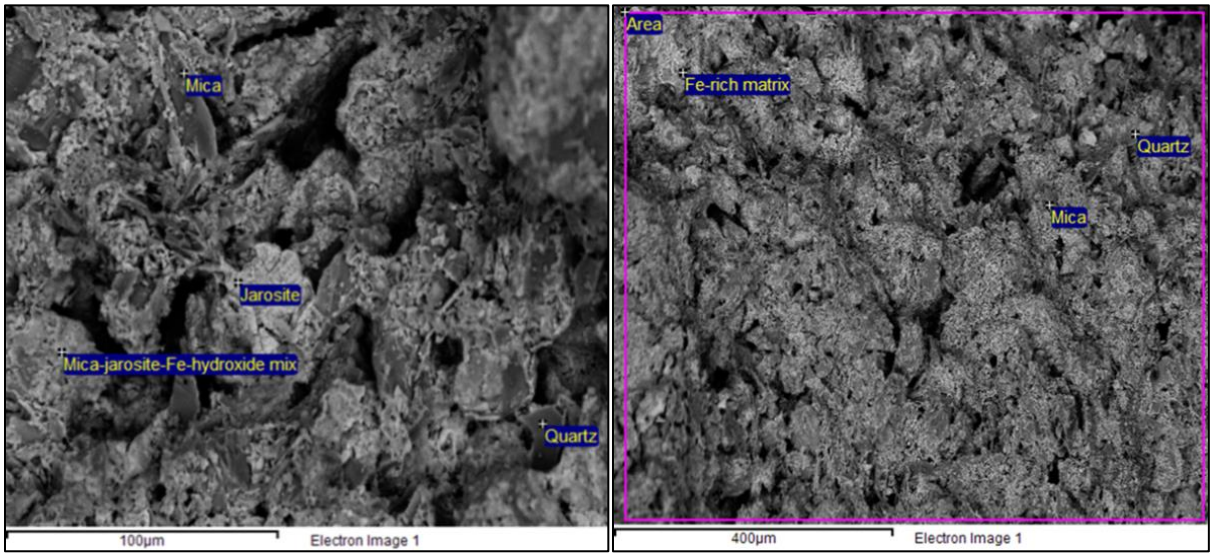

Figure 4-16 SEM image of Jarosite and Fe-rich matrix.

Ca-bearing sulphates and other minerals

Gypsum ($CaSO_4 \bullet 2H_2O$) is recognised as single crystals in alunogen- blodite matrix. Gypsum is covered by halite.

The crystal matrix of the minerals was dominated by chlorine. Fine crystalline habits and the rough texture (disorder lattices) indicate that evaporation occurred from a highly supersaturated groundwater. The crystal sizes of apjohnite, blodite, wupatkiite and tamarugite are generally small, indicating fast crystallization processes. The poor crystalline nature of jarosite, alunogen and hexahydrite are indicative of their high solubility.

4.3.2 Geochemical modelling

In order to identify mineral precipitates that would occur when the salt efflorescent dissolve in water, saturation indices were determined using the PHREEQC geochemical modelling code based on the Wateq4f database. Saturation indices can be defined as the concentration of the dissolved mineral components in saturation with the solution and is expressed as:

$$\text{Saturation Index (SI)} = \log \left(^{IAP}/_{Ksp}\right) \qquad \textit{Equation 16}$$

Where IAP is the ion activity product of the solution and Ksp is the solubility product. An SI value of zero (SI=0) indicates equilibrium between mineral solution and saturation. SI greater than zero indicates super-saturation of the mineral and precipitation will occur. An SI smaller than zero indicates under-saturation and mineral dissolution will occur (Sracek *et al*, 2010)

Representative samples were leached with deionised water. The chemical results from leachate sample analysis, shown in Table 4-9 were used as parameters for geochemical modelling.

In the experiment, evaporation was initiated with 1000 grams of water. Because oxidation-reduction potential information and dissolved oxygen content for the solutions were not determined, modelling was performed twice for each sample. In the first model, a default pe value of 4 was used and the pe value varied depending on the constituents in the solution.

Table 4-9 Physical parameters and anions of the leachates used in the evaporation experiment.

	pH	EC	Cl	SO_4^{2-}	Nitrate as N	Ortho Phosphate
		(µS/cm)	mg/l	mg/l	mg/l	mg/l
MWS 10	8.049	238	33	46	16	0.7
MWS 38	8.204	21.2	78	165	3	<0.2
MWS 51	3.975	2250	-	2 740	<0.2	<0.2
MWS 68	6.393	424	<5	1 970	<0.2	<0.2
MWS 116	6.975	96.4	<5	266	<0.2	<0.2
MWS 149	3.662	2390	14	1 051	0.6	<0.2

In the second model, the solutions were equilibrated with atmospheric oxygen.

It was assumed that the solutions were in equilibrium with the atmosphere. Assuming that the atmospheric pressure is approximately 80 kPa (near Johannesburg), the partial pressure of oxygen is 16.8 kPa or 0.165 atm (oxygen contributes up to 21% of the total atmospheric gases). The saturation index for a gas is equal to log (gas pressure/1 atm). Therefore, the solutions were equilibrated with atmospheric oxygen by defining a saturation index of -0.78. Similarly, the atmosphere consists of 0.04% of carbon dioxide (0.0312 kPa or 0.000315 atm). Therefore, the saturation index used for CO_2 was -3.5.

Solutions were allowed to equilibrate (using the MIX function). Table 4-10 summarises charge balances and pe values of the systems once they were equilibrated with atmospheric oxygen and carbon dioxide. Negative charge balances indicate excess abundance of anions. Positive charge balances indicate abundance of cations. The charge balances were quite poor. Ideally, charge balances should be within ±5%. Their deviation from this suggests that some analytes were not

taken into account. Because alkalinity was not measured, initial default pe value of 4 was used for modelling. When the solutions were equilibrated with atmospheric oxygen, the pe value was allowed to change in order to provide redox equilibrium in the system.

Table 4-10 Charge balances and pe values of the solutions

Solution number	Charge balance (%)	pe
MWS 10	-27	12.5
MWS 38	+90.5	12.4
MWS 51	-61.2	16.6
MWS 69	-92.4	15.8
MWS 116	-65.5	14.16
MWS 149	+ 8.54	16.92

Several minerals followed the ideal saturation index pattern. Some of these minerals are silicate admixtures, which would not be expected to precipitate at a rate comparable to evaporation at atmospheric pressure and temperature. Therefore, silicate admixtures have not been selected as equilibrium minerals even though they do become oversaturated. However, quartz has been defined as an equilibrium phase as there have been reports of low temperature quartz precipitating from exposed solutions. Iron-bearing minerals such as $Fe(OH)_3$ were oversaturated before evaporation began. Their precipitation could be kinetically hindered hence their oversaturation in the starting solution. It is possible for these minerals to precipitate in the environment and their absence in the evaporation profile is merely because they do not follow the ideal pattern. Observations and actions for specific samples can be summarized as follows:

1. **MWS 38:** Evaporation models for MWS 38 are shown in Figure 4-18. This solution had a high pH and a large positive charge balance. Therefore, an additional run was undertaken in which the charge discrepancy in the solution was reduced by allowing the software to introduce carbonate ions until the solution was charge neutral. The solution was still equilibrated with the atmospheric gases.

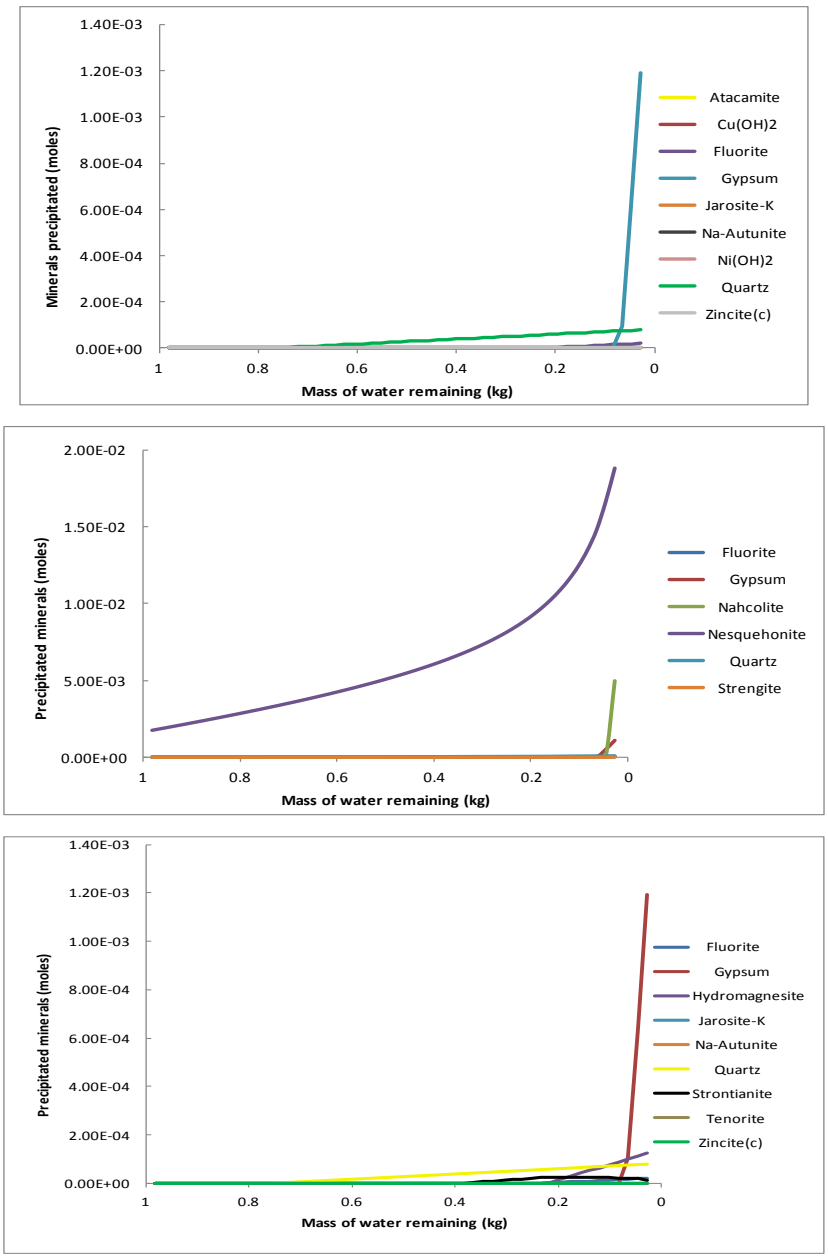

Figure 4-17 Evaporation model of minerals expected to precipitate from MWS 38: a) Evaporation profile with no equilibrated gases and no charge balance b) With charge balance on carbonate species and equilibration with oxygen c) Evaporation profile with no charge balance and equilibration with atmospheric gases.

2. **<u>MWS 51:</u>** Evaporation models for MWS 51 are shown in Figure 4-18. Without the addition of oxygen, the pe of the solution remains low (less than 4). This was not the case

in the above solutions (MWS 10 and MWS 38) because the solution contained a larger amount of redox active elements which equilibrated to define a greater pe (of approximately 12 and 11 respectively). As such, when no minerals are allowed to precipitate in the initial saturation indices observation model, the model predicts the over saturation of sulphide and ore minerals which is very unlikely in an aerobic, oxic environment. The precipitation of gypsum removes the sulphur from the system and the sulphide minerals approach saturation but do not become oversaturated.

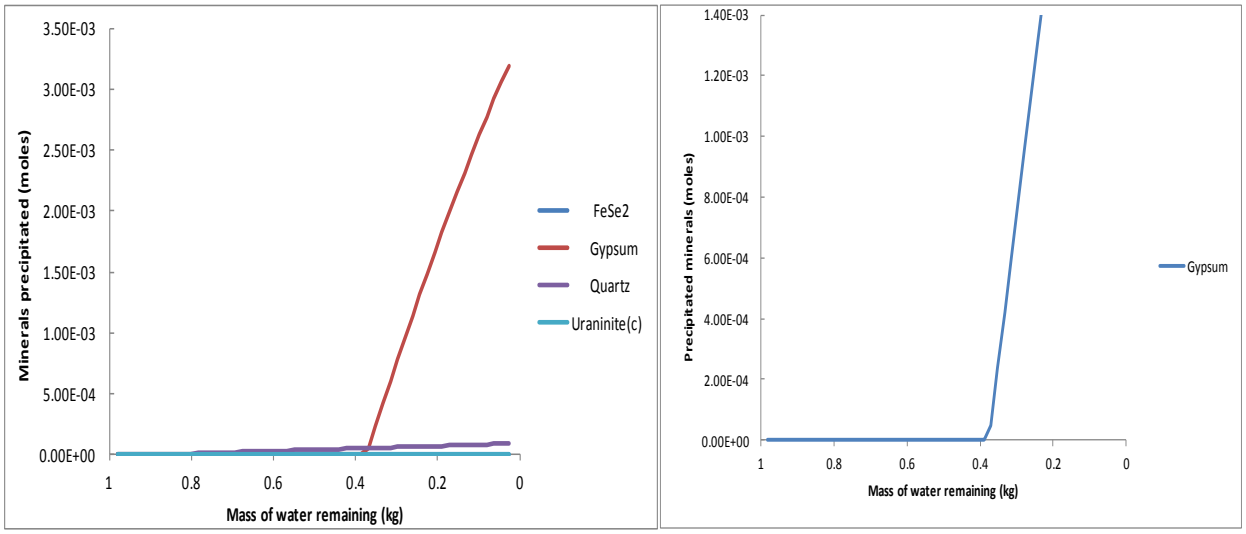

Figure 4-18 Evaporation model of minerals expected to precipitate from MWS 51, a) Evaporation profile with no equilibration of gases b) Evaporation profile with the equilibration of atmospheric gases

With the equilibration of atmospheric gases, the model predicts only the formation of gypsum and not of the ore minerals as seen in the model above.

3. **<u>MWS 68:</u>** Evaporation models for MWS 68 are shown in Figure 4-20. Looking at the same model and zooming in on the jarosite curves, the model predicts the complete dissolution of the solid solution jarosite (sodium, hydronium and potassium solid

solution) and the subsequent precipitation of the potassium end member. This occurs towards the end of the evaporation sequence when there is only 135g of water remaining from an initial amount of 1 kg.

Jarosite is oversaturated from the start of the modelling process when the solution is equilibrated with atmospheric oxygen. The equilibration transforms iron (II) into iron (III). Iron (III) is present in jarosite and as such, jarosite is over saturated from the start. The conversion of iron (II) to iron (III) is a slow process in acidic solutions (below pH 3) but occurs significantly quicker at higher pH values. The modelling of the evaporation of this solution would be improved if dissolved oxygen content or Eh measurements were provided. Supposing that the addition of oxygen was modeled first, followed by the evaporation of water from the solution, the evaporation profile would change to the model presented in Figure 4-20.

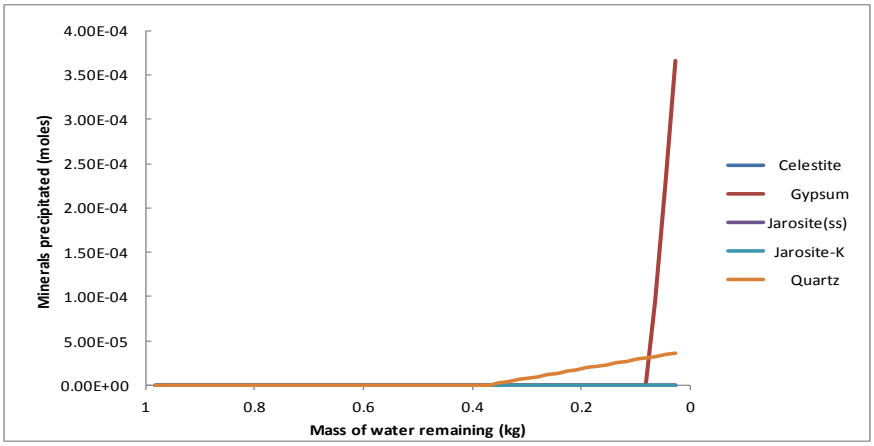

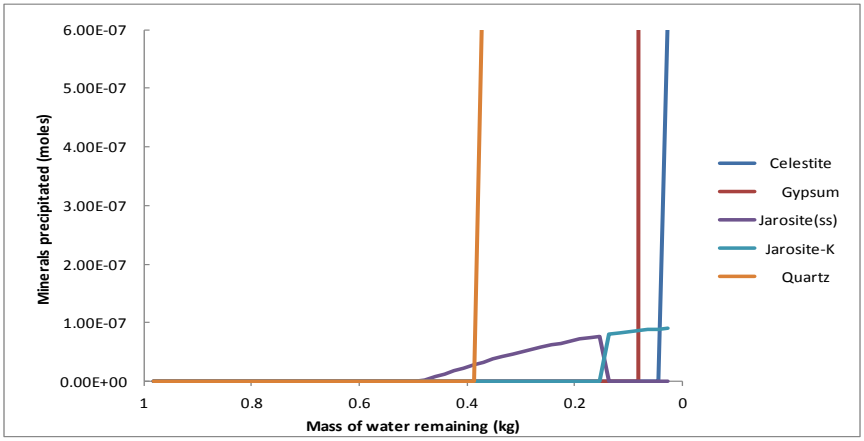

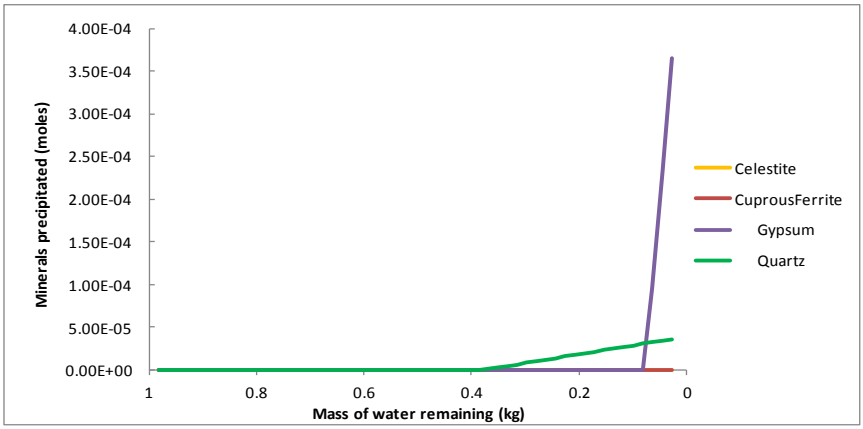

0Figure 4-19 Evaporation model of minerals expected to precipitate from MWS 68, a) Evaporation profile without equilibration of gases, b) Jarosite curve of the same model, c) Evaporation profile assuming complete equilibration with atmospheric gases

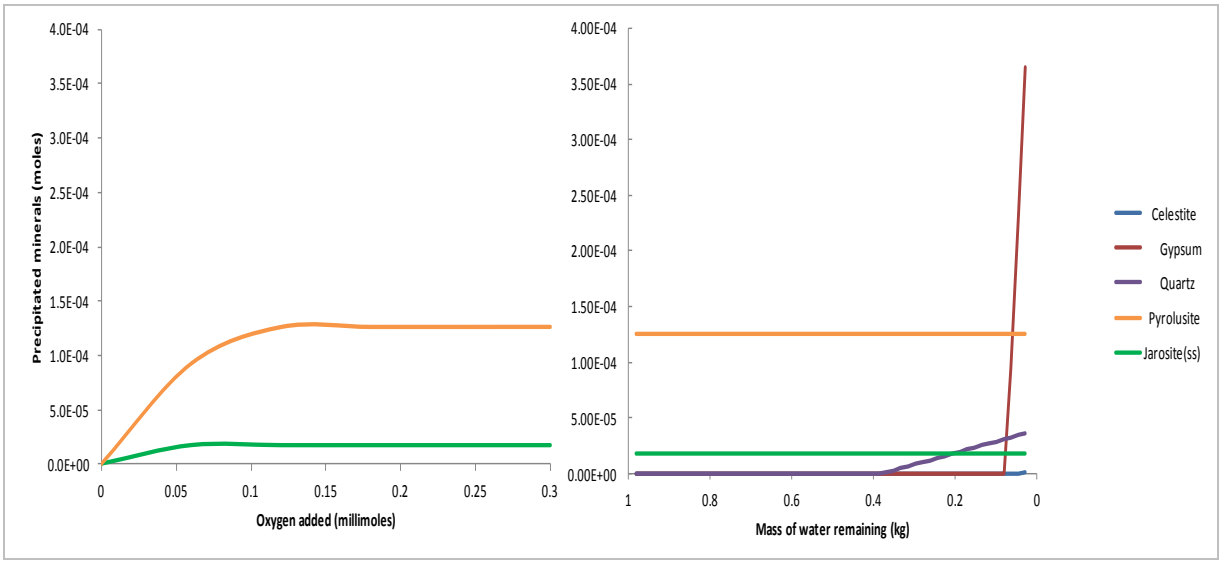

Figure 4-20 Evaporation model of minerals expected to precipitate a) when equilibrated with oxygen b) and then with water

4. **<u>MWS 116:</u>** For the solutions equilibrated with atmospheric oxygen, the solid solution and potassium jarosites and pyrolusite are saturated at the start of the modelling once (similar to MWS 68). Evaporation profile without jarosite and pyrolusite as equilibrium minerals is shown in Figure 4-21 and Figure 4-22 shows an evaporation model without atmospheric gases.

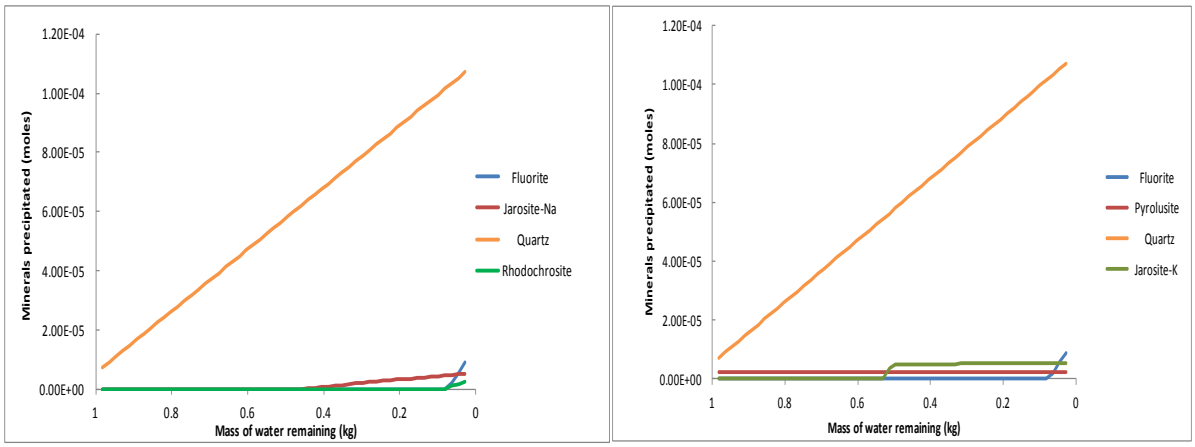

Figure 4-21 Evaporation models of minerals expected to precipitate in equilibrium with atmospheric gases a) modelled without oversaturated solids, b) when solids jarosite and pyrolusite are taken into account

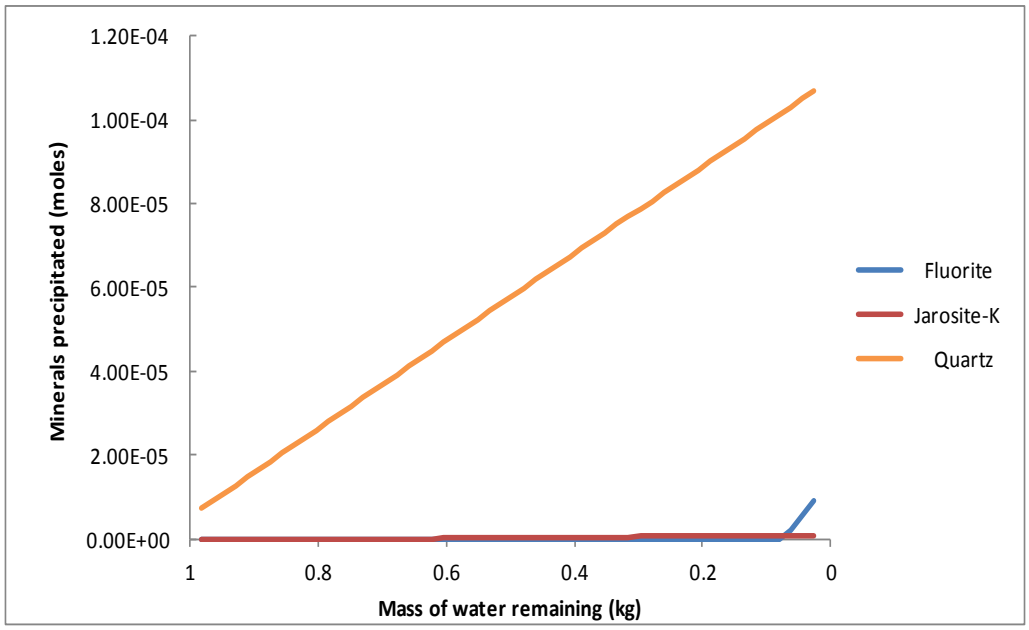

Figure 4-22 Evaporation model of minerals expected to precipitate without equilibration of gases.

5. **MWS 149:** This solution contains significant proportions of redox active elements. As such, upon equilibration of the solution alone without any atmospheric gases, the pe is 15.8. Therefore, most of the iron is speciated as iron (III) and jarosite is over saturated from the start of the modelling process. Looking at the minerals which follow the "ideal" pattern (that is start as undersaturated and become oversaturated), the predicted sequence of precipitation is shown in Figure 4-23a and evaporation model for the solution when equilibrated with atmospheric gases in Figure 4-23b. The model does not change when equilibrated with atmospheric gases because the pe of the original solution is already high.

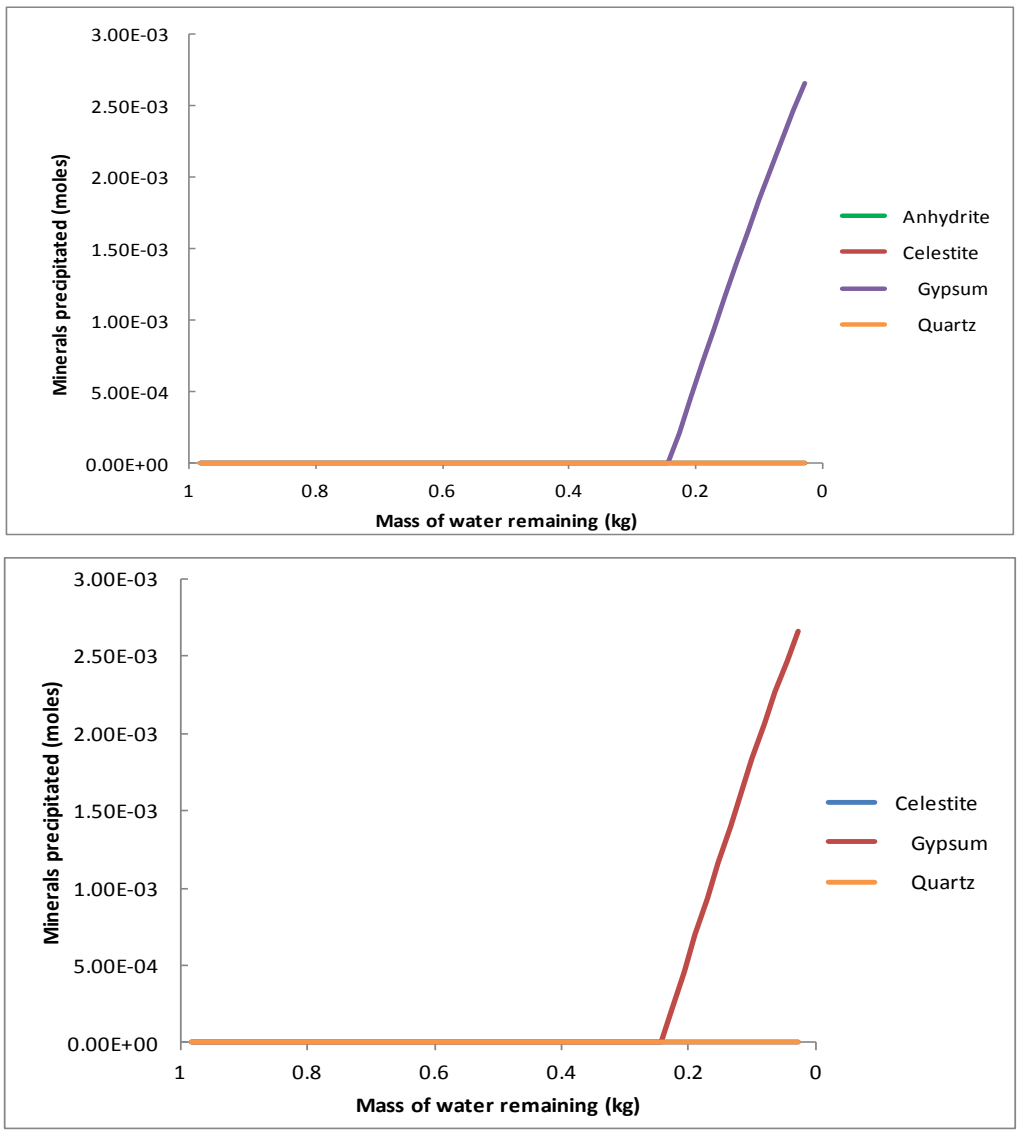

Figure 4-23 Evaporation model of minerals expected to precipitate a) without atmospheric gases, b) when equilibrated with atmospheric gases.

4.3.3 Relationship between XRD and geochemical mineral phases

Field investigations revealed diverse sulphate minerals that are highly unstable and their occurrence is controlled by humidity and temperature variations. Identification of mineralogical phases by X-ray diffraction supports the field observation and suggests that the sulphate minerals precipitate in the series illustrated in Figure 4-24.

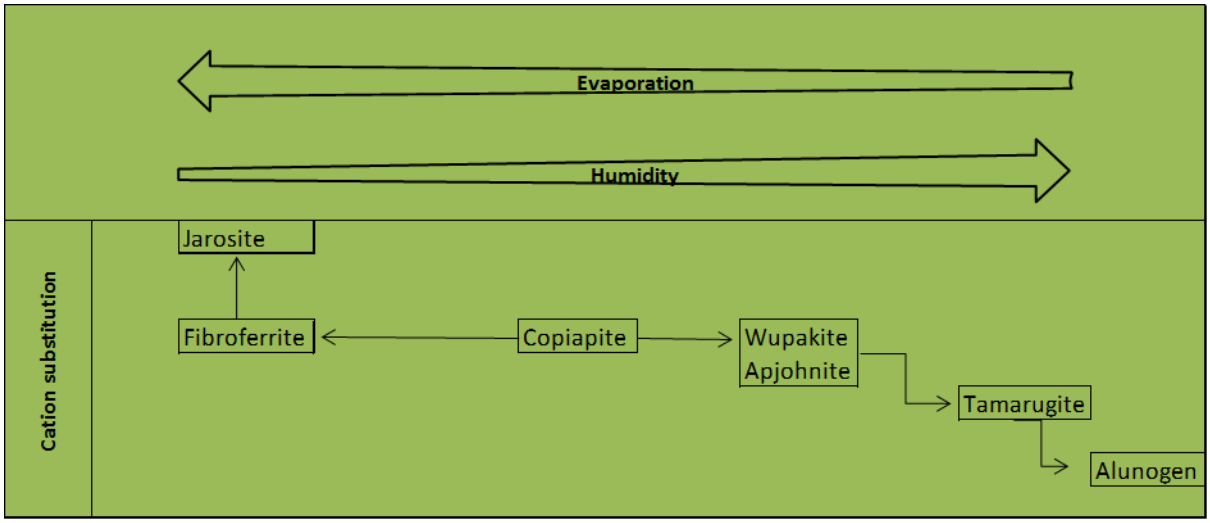

Figure 4-24 Generalised precipitation sequence from XRD results, showing the relationship between evaporation, humidity and cation substitution (Adapted from Onac et al, 2003).

The series of apjohnite through to tamarugite and alunogen indicates high humidity and low evaporation conditions (wet conditions). The sequence of epsomite ($MgSO_4.7H_2O$) to hexahydrite ($MgSO_4.6H_2O$) to starkeyite ($MgSO_4.4H_2O$) in Table 4-8 also indicates decreasing moisture contents and high evaporation rates (dry conditions).

Geochemical modelling results indicate that carbonate minerals have the highest saturation indices. Salt leachates are under saturated with Al-mineral phases. High saturation indices can be explained by the pH of the samples and Al minerals precipitates at low pH conditions. The precipitation of gypsum and other sulphate minerals is largely influenced by the concentration of salts. Calcite, gypsum and fluorite precipitate earlier because of higher total concentrations. High salt content also causes these minerals to precipitate in large quantities. Anhydrite, celestite and magnesite are at or near equilibrium in water. These minerals were not detected by XRD, and their presence can be interpreted as amorphous phases. Detected sulphate salts apjhonite and tarmarugite are both below saturation point. Their presence suggest that they formed by evaporation.

Table 4-11 tabulates predicted mineral phases and observed mineral phases. Detected and predicted mineral phases correspond very well. Evaporation results show that upon dissolution, iron and sulphate remain dominant ions. The difference between detected and predicted minerals shows the incorporation of metals in these minerals. Dissolution releases metals and acid components that were incorporated in the minerals. The dominance of jarosite after dissolution indicates persistent acidic conditions.

Table 4-11 Predicted XRD and ASD interpreted mineral of selected salt precipitates

Sample	Predicted	Detected (XRD)	ASD interpreted
MWS 38	Flourite Gypsum Jarosite-K Magnesite	Hexahydrite Fibroferrite Epsomite	Anhydrite Hematite
MWS 51	FeS_2 Gypsum	Aragonite Jarosite	Geothite Hematite
MWS 68	Celestite Gypsum Jarosite-SS, Jarosite-K	Gypsum Apjonite Alunogen	Copiapite Gypsum Thernadite
MWS 116	Fluorite Jarosite Rhodochrosite	Aragonite Hematite	Thernadite Geothite Hematite Copiapite
MWS 149	Gypsum	Gypsum Jarosite	Gypsum Jarosite Thernadite

4.4 Spectral characteristics

The preceding section gave results for XRD analysis and geochemical modelling. Similarities and discrepancies in mineral identification between the two techniques were highlighted and explained. The following section presents results for spectral characterisation using the ASD hand held spectrometer.

4.4.1 Analysis of reflectance spectra

The reflectance spectra collected from mineral crusts were subjected to qualitative and quantitative analysis to determine mineral end-members. Qualitative analysis involved the comparison of the reflectance spectra with spectra of known end members. It also involves the characterisation of wavelength parameters like depth, width, area, asymmetry and position of lowest reflectance points.

The 400 – 2500 nm part of the electromagnetic spectrum is particularly useful for mineral identification. This region was divided into two parts namely the 400 – 1300 nm and 1300 – 2500 nm parts. Mineral absorption features in the Visible and Near Infra-Red (VNIR) (400 – 1300 nm) are caused by electrical processes of transitional metals like Fe, Pb, Ti, Cu, Co, and Cr. In the shortwave infrared (SWIR) region (1300 – 2500 nm), absorption features are caused by vibrational processes of OH, H_2O, NH_4, SO_4^{2-} and CO_3. Vibrational absorption features only occur at wavelengths greater than 940 nm and are usually sharper and more defined than electric absorption features. The visual inspection of the spectra (Figure 4-25) from all the samples indicated that mixtures of quartz, carbonates, clays minerals and organic matter were present.

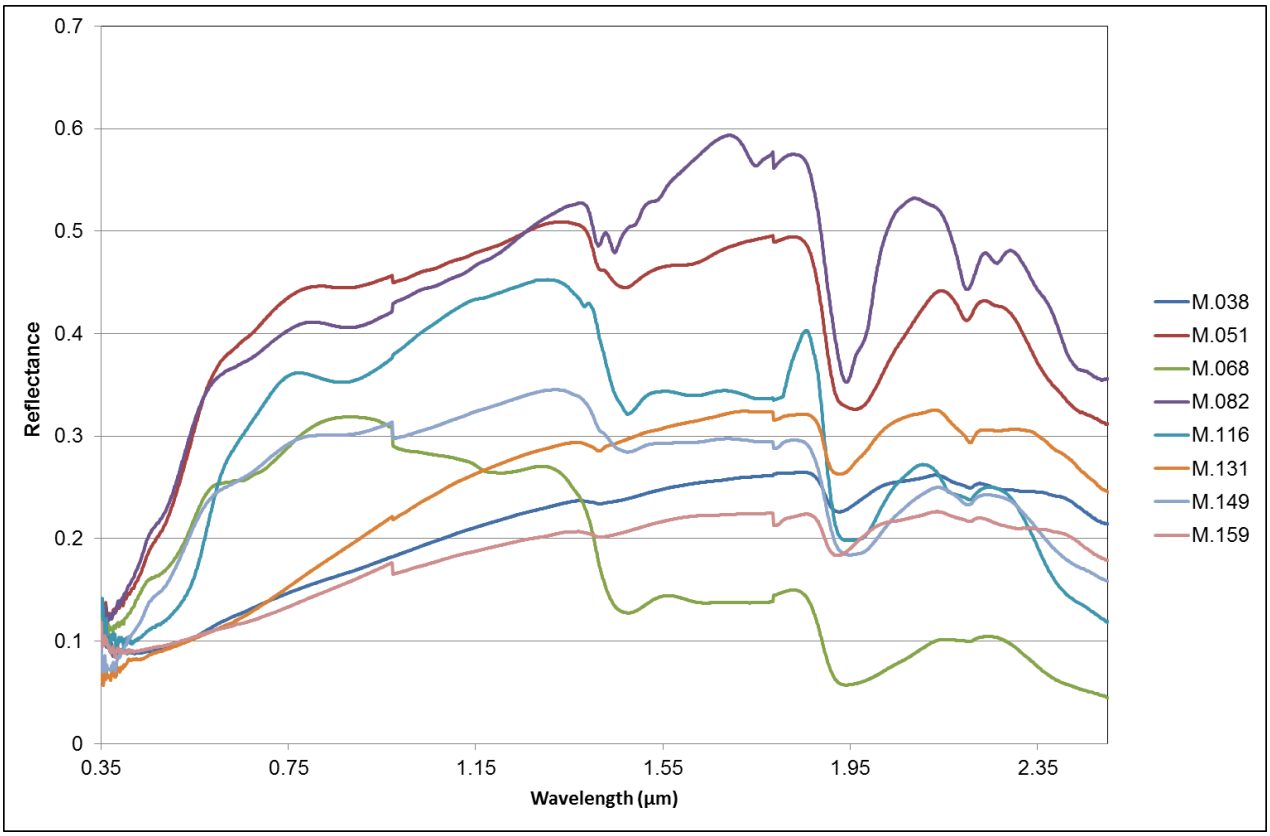

Figure 4-25 Reflectance spectrum of selected samples with wavelength positions that were used in mineral interpretation

4.4.2 Identified minerals and their diagnostic absorption features

The analysis of reflectance spectra were used to identify minerals Spectrally interpreted minerals are listed in Table 4-12 and consisted mainly of Smectite minerals, Fe-oxide and sulphate minerals.

Smectite mineral group

The dominant clay minerals in all the samples are the smectite group minerals. This group includes montmorrillonite and vermiculite. Prominent Al-OH absorption features at 1.417 nm, 1.91 nm and 2.20 nm are clearly visible. The depths of the absorption features in

Figure ***4-26*** were useful in discriminating between montmorrillonite and vermiculite.

Table 4-12 Minerals identified in spectral analysis

Sample	Microcline-albite	Nepheline	Thernadite	Jarosite	Geothite	Hematite	Copiapite	Montmorillonite/vermiculite	Anhydrite	Kaolinite	Natroli	Gypsum	Eugsterite
M.031	x	x	x					x	x				
M.038						x		x	x				
M.040	x					x	x	x					
M.051	x					x		x				x	
M.059	x	x	x		x				x	x	x		x
M.068		x	x				x				x	x	x
M.082		x								x		x	x
M.116	x		x		x	x	x	x		x	x		
M.131	x	x			x	x			x				
M.147			x	x				x				x	
M.149		x	x	x							x		x
M.159				x		x			x				

Two types of montmorrillonite can be differentiated. Natronite is the Fe^{3+} end-member and Sauconite, the Zn-containing end-member of montmorrillonite. The Fe-OH diagnostic absorption feature of Natronite was identified around 2285 nm. The diagnostic Zn-OH absorption feature of Sauconite at 2298 nm is less well-defined.

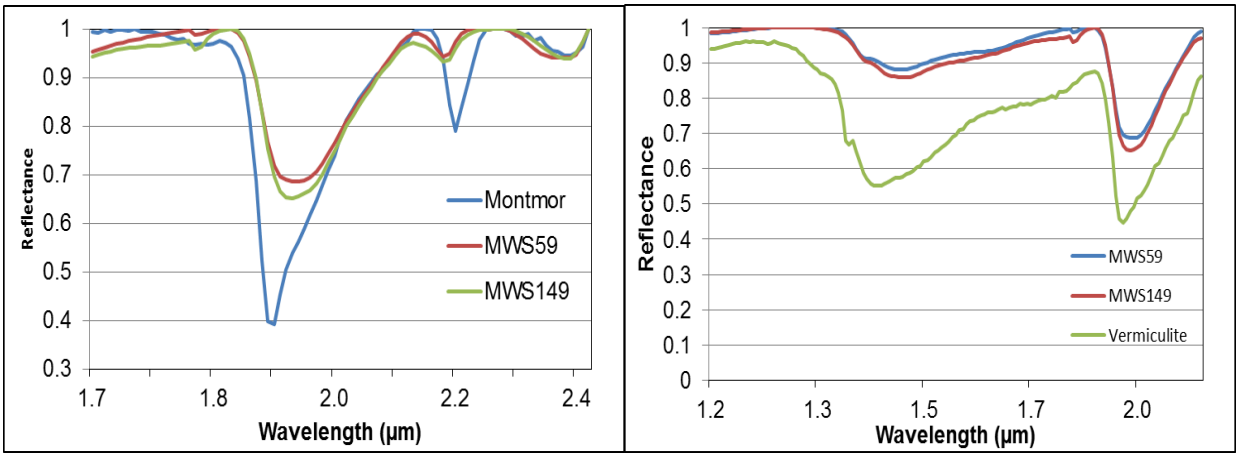

Figure 4-26 Continuum removed reflectance spectra of a) Montmorrillonite and b) Vermiculite.

Fe-Oxide mineral groups

Characteristic absorption features of iron oxides occur at 400-450, 510 – 550, 700, 870 and 1000 nm, because of Fe^{2+} and Fe^{3+} activity. Iron oxides also show a concave shape to the spectra between 450 – 850 nm. In soil mixtures, this concave shape is narrower and less absorption occurs when goethite is dominant. Figure 4-27a show that mixtures abundant in hematite have wider concavity and greater absorption.

Absorption intensities (after continuum removal) at 550 and 900 nm are useful in distinguishing Fe-oxides from sulphate minerals Figure 4-27b shows that goethite is the dominant hydroxide mineral present in most samples. It evolves from ferrihydrite in the presence of sulphate. Over time, with limited sulphate (and increased liming) goethite evolves into hematite. In the study area, goethite is associated with hematite and magnetite, both Fe oxides but with different crystal composition. The presence of iron oxide absorption features at 900 nm is consistent with red ochre samples.

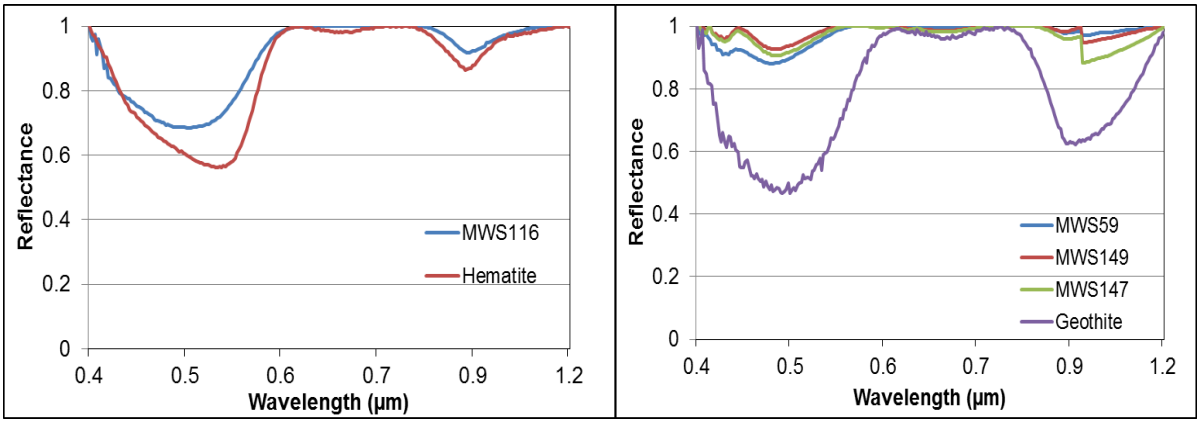

Figure 4-27 Continuum Removed reflectance spectrum of a) Hematite and b) Geothite

Sulphide and sulphate minerals

Sulphide minerals have low reflectance and are not easily identifiable using reflectance spectra except in areas where they are exposed or occur in high concentration (Montero *et al*, 2005). Pyrite and pyrrhotite are the common sulphide minerals in the study area. Pyrrhotite is readily oxidised and therefore it would be expected to occur in fresh unoxidised tailings. Pyrite was only detected in one sample and this is in agreement with prior knowledge that there was limited pyrite in the tailings material. Dominant iron-free sulphates in the area include anhydrite, gypsum, eugsterite, blodite and thenardite. Copiapite and pyrrhotite are the main iron sulphate and sulphide minerals, respectively found in the study area. The spectrum of these minerals is dominated by water related absorption features (Table 4-13). Thenardite, anhydrite and pyrrhotite do not have water or hydroxyl in their crystal structures and therefore do not have water absorption bands in these regions.

Table 4-13 Wavelength position of absorption features caused by water and metal bonding

Mineral	1.4 region	1.9 region	2.0 - 2.5 region
Gypsum	1.45	1.95	2.20, 2.42
Eugsterite	1.44	1.94	2.2
Blodite	1.47	1.95	2.2
Copiapite	1.45	1.95	2.2

Eugsterite and blodite are dominant evaporate minerals. Copiapite in **Error! Reference source not found.** shows low reflectance because of water content. Evaporation of saline solution causes gypsum to precipitate first and thenardite precipitate over gypsum. This may explain the dominant spectral signature of thernardite in Figure 4-28. Blodite precipitates after thernadite. Flat VNIR signature in Figure 4-28 may point to well defined crystalline structure of sulphate minerals.

4.4.3 Relationship between spectral mineral end-members and XRD mineral phases

As discussed in Section 4.3.1, X-ray diffraction results confirmed the existence of clays and mica minerals. No pyrite was detected by XRD and minor amounts of goethite, hematite and jarosite were detected. This implies that these minerals occur in quantities below the detection limit of the XRD method, and that pyrite has been oxidised to goethite and hematite. Copiapite was interpreted as fibroferrite. The observed association of hematite and geothite is indicative of coating. Because of similar chemical structure and reflectance spectrum, the XRD method is not able to differentiate between different iron oxyhydroxides minerals.

It is possible that the samples lost water and became dry during the period of spectral signature collection and XRD analysis. Because of overlapping major water absorption features, gypsum and sulphate salts were difficult to differentiate. This can also be interpreted as sulphates precipitating in clay minerals or reoccurring with clay minerals. Blodite, apjohnite, and

tamarugite, which were identified using XRD analysis, could not be identified by spectral analysis since known spectral signatures for these minerals were not available in existing spectral libraries.

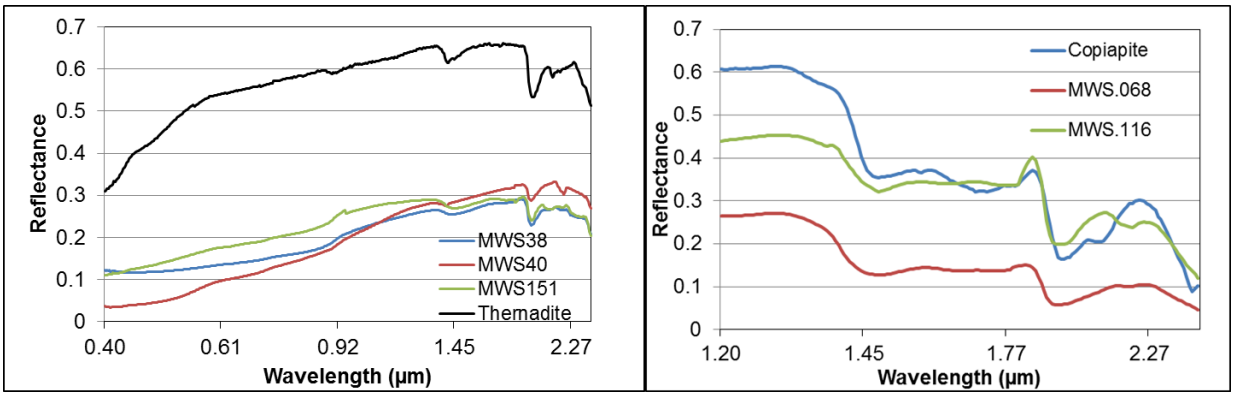

Figure 4-28 Reflectance spectrum of Thernadite and Copiapite

4.5 Correlation between spectral charactersitics and geochemistry

Results of Spearman correlation between single wavelength and element concentration are presented in Figure 4-29. The structure of correlation is the same; it is the strength of the correlation that varies. Correlograms show that a strong correlation occurs around the iron and iron oxide absorption feature at around 550 nm. The broad area between 700 -1400 nm is linked to the strong absorption feature band of the ferrous ion centered at 1100 nm. Strong absorptions at 1400 nm and 1900 nm are related to water bands and hydroxyl absorption. Absorptions at 2195 nm indicate metal-OH bonding in clay minerals like montmorollite (Crowley *et al*, 2003; Fan *et al*, 2012). At 2195 nm it means Cu, U, Ni, Co, and SO_4^{2-} are associated with clay mineral absorption features and As, Cr, V, pH and Fe show negative correlation with clay absorption features. Another notable strong correlation occurs at 2350 nm. This feature is caused by carbonate absorption. The carbonate absorption feature shows correlation trends similar to the

water and hydroxyl band features. Collelograms in Figure 4-29 also show correlation coefficients change from positive to negative at 550 nm and 790 nm regions and from negative to positive at 790 nm to 1300 nm. This correlation trend can be interpreted to present regions sensitive to element concentrations.

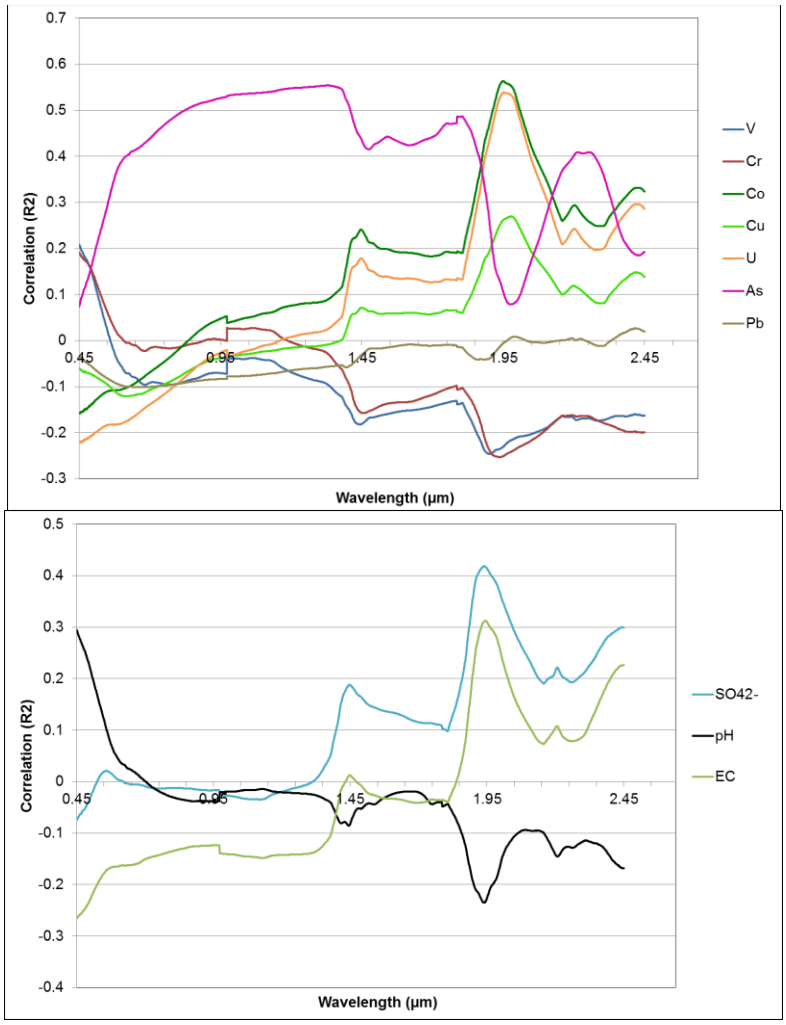

Figure 4-29 Collelogram of reflectance spectra and geochemical variables (n=29)

4.5.1 Correlation of geochemical variables with spectral parameters (QAF)

The degree of correlation between Quantitative Absorption Feature (QAF) variables defined in section 3.6.1 and geochemical variables was determined using Spearman correlation coefficient and the results are shown in Table 4-14. Lead (Pb) showed weak negative correlation with 2.2 µm Depth and 2.2 µm Area variables. Cu showed a negative statistically significant correlation with the 2.2 µm Depth parameter. Other metals did not show any significant correlation with spectral variables. SO_4, EC and TDS showed low significant correlation with 1.4 µm Area, 1.4 µm Depth, 1.9 µm Area, 1.9 µm Depth variables. The pH showed significant correlation with 1.4 Asym, 1.9 Asym and 2.2 Asym parameters.

Table 4-14 Correlation coefficients between spectral parameters variables and geochemical variables

	1.4Depth	1.4Area	1.4Asym	1.9Depth	1.9Area	1.9Asym	2.2Depth	2.2Area	2.2Asym
V	0.16	0.23	-0.17	0.15	0.11	-0.09	-0.04	0.01	-0.07
Cr	0.15	0.18	-0.06	0.17	0.11	0.07	-0.09	-0.04	-0.09
Ni	-0.12	-0.10	0.01	-0.20	-0.20	-0.01	-0.23	-0.21	-0.16
Cu	-0.10	-0.05	-0.08	-0.13	-0.15	0.07	**-0.33****	-0.29	-0.02
Zn	-0.06	-0.08	-0.28	-0.22	-0.17	-0.09	-0.21	-0.21	0.05
Pb	0.09	0.11	-0.30	-0.02	-0.07	-0.03	**-0.40***	**-0.34****	0.30
U	-0.15	-0.20	0.25	-0.16	-0.16	0.17	-0.02	-0.09	-0.17
As	0.19	0.11	0.14	0.08	0.06	0.21	0.20	0.15	-0.23
Cl	-0.13	-0.10	-0.05	**-0.32****	-0.25	**-0.32****	-0.24	-0.19	0.14
NO_3	-0.15	-0.12	0.01	-0.26	-0.28	0.12	**-0.43***	**-0.38***	**0.40***
SO_4^{2-}	**-0.33****	**-0.37***	0.23	**-0.39***	**-0.39***	-0.02	-0.11	-0.08	-0.13
pH	0.19	0.28	**-0.50***	0.20	0.20	-0.43	-0.17	-0.15	**0.35****
EC	**-0.41***	**-0.45***	**0.36****	**-0.36****	**-0.43***	0.22	0.06	0.15	-0.20

Correlation is significant at the 0.05 level (2-tailed). **Correlation is significant at the 0.01 level (2-tailed).

4.5.2 Regression results with non-spectral data

Data transformation is necessary before regression analysis to normalise potentially skewed distributions. The log transformation was applied after studying the shape characteristics of the QAF parameters. The results of the Shapiro-Wilk normality tests before and after transformation are shown in Table 4-15. In multiple regression analysis, several variables are used to determine their influence on the dependent variable. The relationship between dependent and independent variables is presented as the line based on the least sum of squares. The model is summarized by R^2 which is the variance that can be explained by the regression model. The Adjusted R^2 indicates variance that will be obtained when the model is calculated with new data. Using the SAS Enterprise software, statistics were tested for significance at the 95% level of confidence.

Table 4-15 Normality test for QAF parameters (n=30)

	Before transformation	After transformation
	S-W	S-W
1.4Depth	0.0003	
1.4Area	0.0001	
1.4Asym	0.0001	
1.9Depth	0.0512	0.0001
1.9Area	0.0043	
1.9Asym	0.0011	
2.2Depth	0.2139	0.0011
2.2Area	0.0008	
2.2Asym	0.0006	
MAX0.69D1	0.0001	
MAX0.98D1	0.0711	
MIN1.411D1	0.0006	
MAX1.423D1	0.0001	

MIN1.89D1	0.0076	
MAX2.2D1	0.1473	0.0001

The 15 QAF variables listed in the first column of Table 4-15 were used to describe geochemical variables. Only three geochemical variables, V, SO_4^{2-} and pH showed a significant relationship with spectral variables. Figure 4-30 shows the regression coefficients of spectral parameters for the models. Regression loadings show that variation of V, Cr and SO_4^{2-} is explained in 1400nm and 2200nm regions and to a lesser extent by 500 nm - 610 nm regions. The three regions gave good prediction estimates ($R^2 > 0.9$). However, QAF parameters did not explain the variation of other geochemical models.

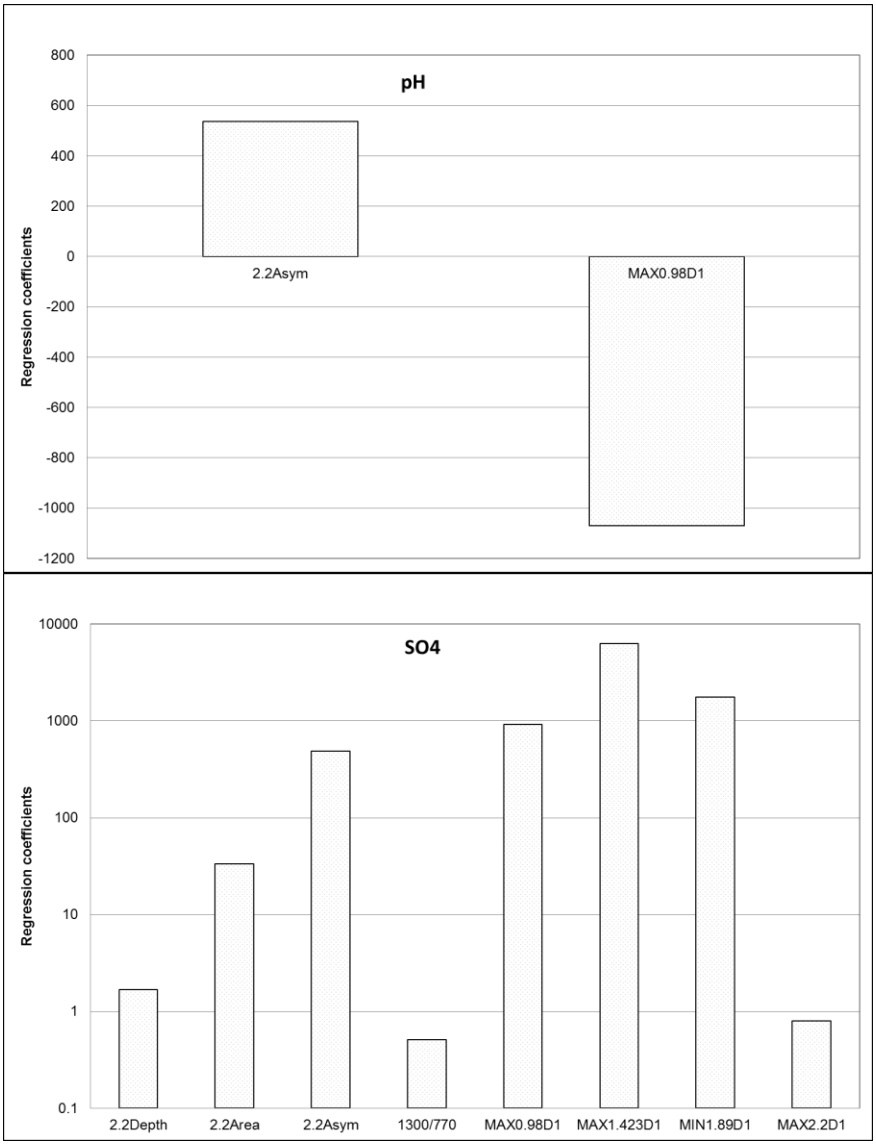

Figure 4-30 Significant spectral parameters for pH and SO_4^{2-} variables.

4.5.3 Spectral indices for salts

There are numerous soil indices that have been developed for salt detection and identification. The most common indices are for soil colour. Soil colour indices are used to elucidate soil quality, weathering and oxidation reactions (Khan *et al*, 2001). Indices to quantify soil colour are also useful in agriculture and pollution studies because soil colour is the function of organic matter, Fe oxides, carbonates and other substances. The most useful indices for soil salinity

according to Khan *et al* (2001) are Normalized difference salinity indices (NDSI), Salinity indices (SI) and Simple Index and Table 4-17 shows the equations of these indices.

Table 4-16 Soil Indices for soil colour characterization

Spectral Index	Equation	Property
Brightness Index (BI)	$(R^2+G^2+B^2)/3.0)0.5$	Mean soil reflectance
Saturation Index (SI001)	(R – B)/(R+B)	Index spectral slope
Hue Index (HI)	(2*R-G-B)/(G-B)	Dominant wavelength
Coloration Index (CI)	(R-G)/(R+G)	Hematite/Hematite+Goethite ratio
Redness Index (RI)	$R^2/(B*G^3)$	Hematite content

Table 4-17 Spectral indices for salinity (Khan et al, 2001)

Index	**Equation**
Normalized Difference Salinity Index (NDSI)	NDSI = (0.63 to 0.69 μm) - (0.9 to 0.76-μm)/ (0.63 to 0.69 μm) + (0.76 to 0.9 μm)
Simple Ratio (SR)	SR = 0.75 - 0.90 μm / 0.63 - 0.69 μm
Normalized Difference Salinity Index (NDSI(1))	NDSI = (10.40-12.5μm) – (0.75 .90μm)/ (10.40-12.5μm) +(0.750.90μm)
Salinity Index (SI)	SI = {(0.43-0.515μm) × (0.63-0.690 μm)}1/2
SI 1	SI = √ (G*R)
SI 2	SI =√ (G2 +R2 +NIR2)
SI 3	SI =√ (G2*R2)

The above spectral indices were determined to identify spectral regions sensitive to salinity. In this study, the blue band was defined as a region from 400 nm – 490nm, the green band as 491 nm – 580 nm, the red band as 620 nm – 780 nm and NIR band as 790 nm - 890 nm. The statistical variability of spectral indices is shown in Table 4-18. The measured EC and pH of samples were considered as measure of salinity. Correlation between soil indices and the measure of salinity are shown in Table 4-19.

Table 4-18 Explanatory statistics for all calculated spectral variables (n=29).

Variable	Mean	Std Dev	CV(%)
NDSI	-0.11	0.05	-49.06
SR	1.25	0.15	11.60
NDSI (1)	0.05	0.18	388.53
SI	0.02	0.01	76.24
SI 1	0.18	0.08	43.13
SI 2	0.37	0.15	39.06
SI 3	0.27	0.11	42.94
BI	0.02	0.01	77.08
SI_0001	0.30	0.15	48.64
HI	6.94	3.63	52.24
CI	0.19	0.09	48.30
RI	275.84	384.83	139.51

Table 4-19 Correlation between pH, EC and spectral measurements of soil salinity

	pH	EC
NDSI	0.12	-0.07
SR	-0.12	0.07
NDSI (1)	-0.05	0.08
SI	0.22	-0.25
SI 1	0.16	-0.19
SI 2	0.08	-0.12
SI 3	0.16	-0.18
BI	0.17	-0.18
SI_0001	**-0.42**	**0.46**
HI	0.14	-0.11
CI	**-0.40**	**0.44**
RI	-0.33	0.37

Only spectral indices SI_0001 and CI showed significant correlation with salinity content. SI and CI showed negative correlation with pH and positive correlations with EC.

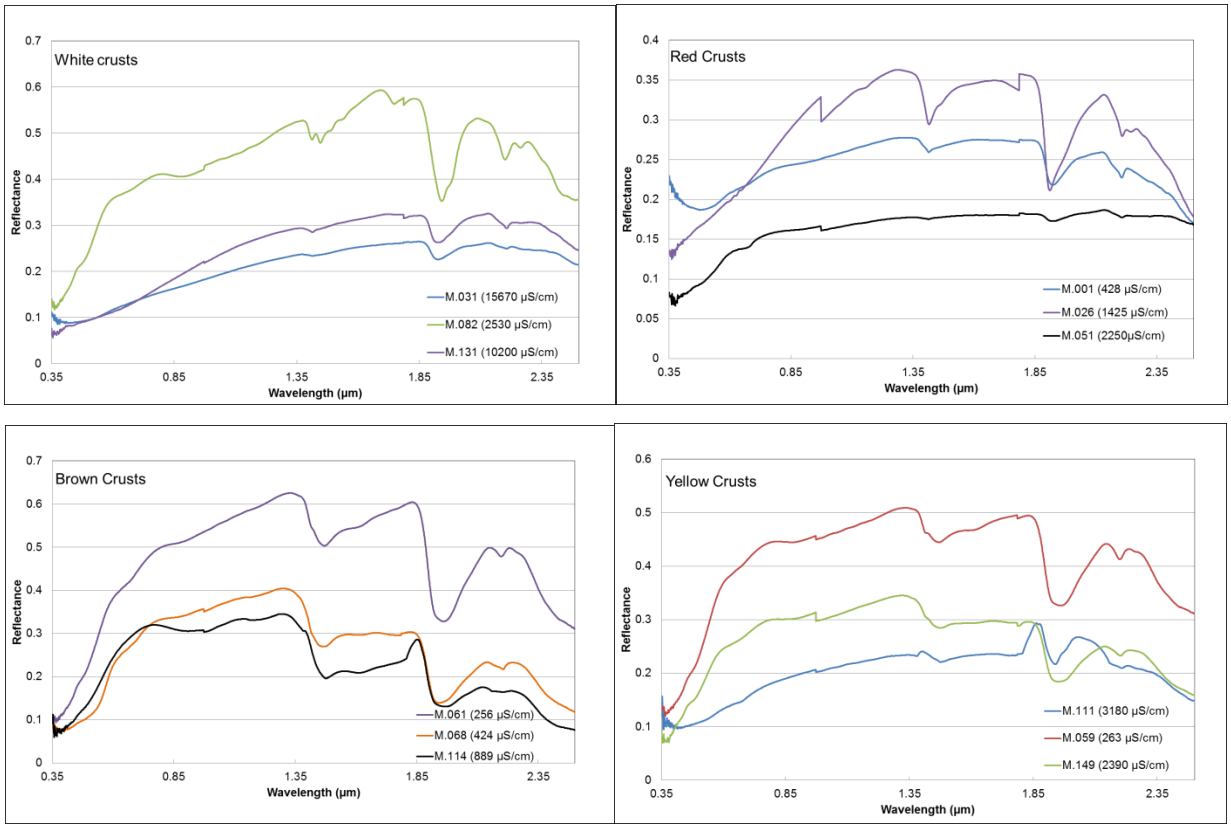

Figure 4-31 Variation of soil reflectance in various sample colours

The investigation of the reflectance spectra and how it varies with the EC of salts was also performed. In order to enhance sensitive bands, the first derivative spectrum was drawn for comparison. Figure 4-32 shows reflectance spectra and FD spectra of efflorescent salts with varying EC divided according to colour. These graphs show regions around 1400 nm and 1800 nm as the main indicators of salinity.

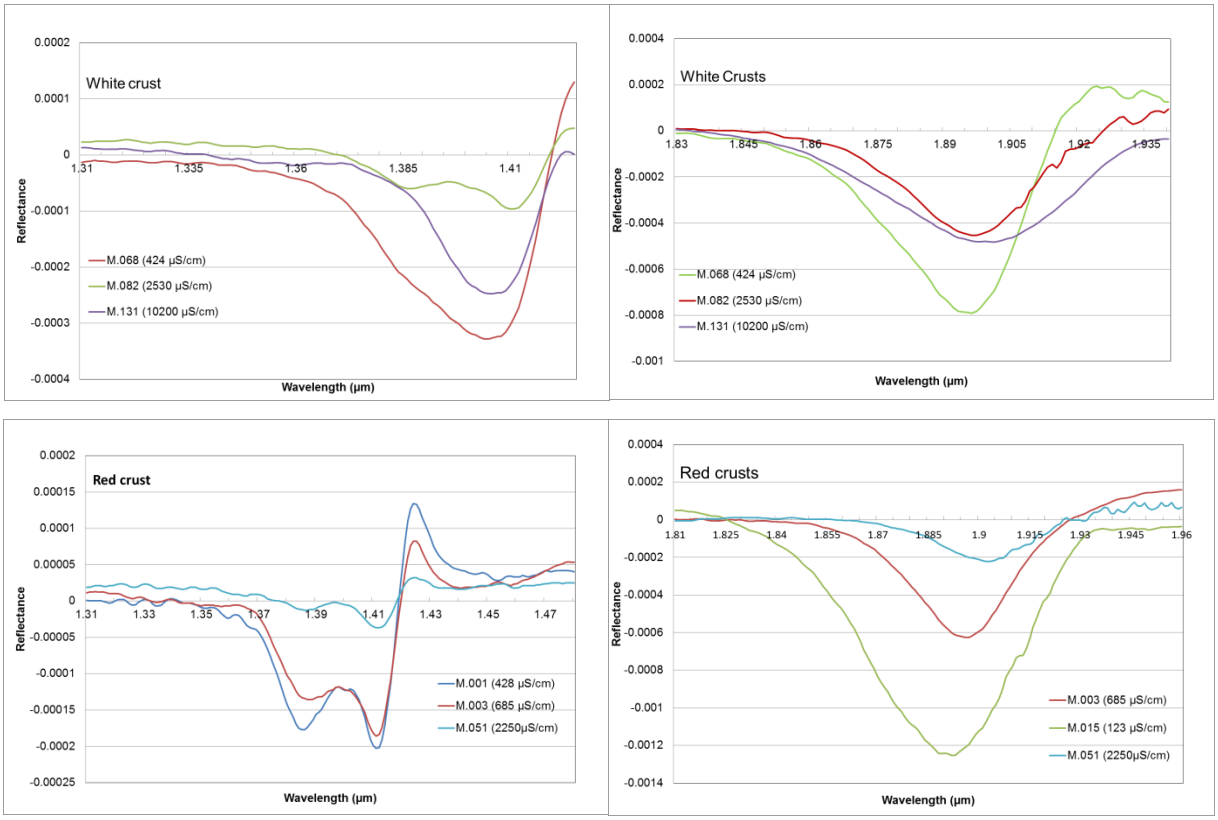

Figure 4-32 The influence of salinity in spectral reflectance of salts

4.5.4 Partial Least Squares Regression

Partial least squares regression (PLSR) is a quantitative multivariate technique used to analyse the correlation between variables and model several response variables simultaneously. PLSR was performed on the measured geochemical variables and wavelength range between 400 and 2400 nm using 29 analysed samples. The PLSR results depend on pre-processing techniques and the number of factors selected.

To account for albedo effects, the mean-centre normalisation technique was used (Viscarra Rossel *et al*, 2006). For spectral smoothing, the Savitzky-Golay filter, second polynomial was used. Savitzky-Golay smoothing is an averaging technique that calculates polynomial regression

on the distribution to determine the smoothed value for each point (Xie *et al*, 2012). This filter is preferred because it preserves the shape parameters (relative maximum, minimum and width) of the spectra while removing baseline effects (Ramoelo *et al*, 2013). The leave-one-out cross-validation method was performed to determine the number of factors or latent variables to be fitted in a model. Mean centred data was used for constructing all PLSR models.

To evaluate the performance of regression models, bootstrapping statistics were determined. Bootstrapping is useful when working with limited samples, it iteratively resample the data set, and in turn improving prediction accuracy of the model (Ramoelo, 2013). The same number of optimal factors used in model development was used for validation with the total number of 30 bootstraps.

These PLSR results are a set of calculated values and the performance of the model is assessed by the root mean square error of prediction (RMSEP), coefficient of determination (R^2) and rapid prediction deviation (RPD). Evaluation parameters RMSEP, R^2 and RPD were determined using the following:

$$R^2 = \frac{\sum_{i=1}^{n}(\hat{y}i - \hat{y})\,2}{\sum_{i=1}^{n}(\hat{y}i - \hat{y})\,2} \qquad \textit{Equation 18}$$

$$\text{RMSEP} = \sqrt{\frac{\sum_{i=1}^{n}(\hat{y}i - \hat{y})2}{n}} \qquad \textit{Equation 19}$$

$$\text{RPD} = \frac{\text{SD}}{\text{RMSEP}} \qquad \textit{Equation 20}$$

Where n is the number of samples, $\hat{y}_i$ = is the measured value, $\hat{y}$ is the predicted value and SD is the standard deviation.

High R^2 values indicate strong linear between measured and predicted values. RMSEP present the amount of variables not accounted for by the model, and this error should be low. RPD

indicated the capabilities of the model to accurately predict variables by taking into account the variable's variability (Xie *et al*, 2012). Following Luleva (2007), Viscarra Rossel (2006) and Wu *et al* (2007), RPDs in this study were classified as follows:

RPD greater than 2.0 as good

RPD 1.4 – 2.0 as reasonable (acceptable accuracy).

RPD less than 1.4 as not reliable (poor accuracy)

The results of PLSR models are tabulated in Table 4-20. PLSR prediction results are reliable for major elements. Generally, the coefficient of determination is low for the selected elements. Reliable prediction results were obtained for SO_4^{2-}, and EC. These elements showed high concentration levels with limited variability.

In order to display regions of spectral significance, partial coefficients for each wavelength are shown in Figure 4-33. The PLS plots show the correlations between significant wavelength regions and prediction model as peaks and valleys. The important wavelengths for all geochemical variables are 1400 nm, 1800 nm – 2100 nm and 2200 nm. Non-spectra regression also reported the similar results around these regions. PLS coefficients in Figure 4-33 show patterns similar to the patterns obtained by in correlation analysis (Figure 4-29).

PLSR regression coefficients in Figure 4-33 show major absorptions around 1400 nm and 1900 nm. This provides further proof that clay minerals absorb these elements. High clay content leads to high metal content and this in turn leads to a decrease in reflectance because of absorption. Clay absorption features are narrower than Fe absorption feature at 525 nm. This means the absorption capacity of clay minerals is stronger than that of iron minerals.

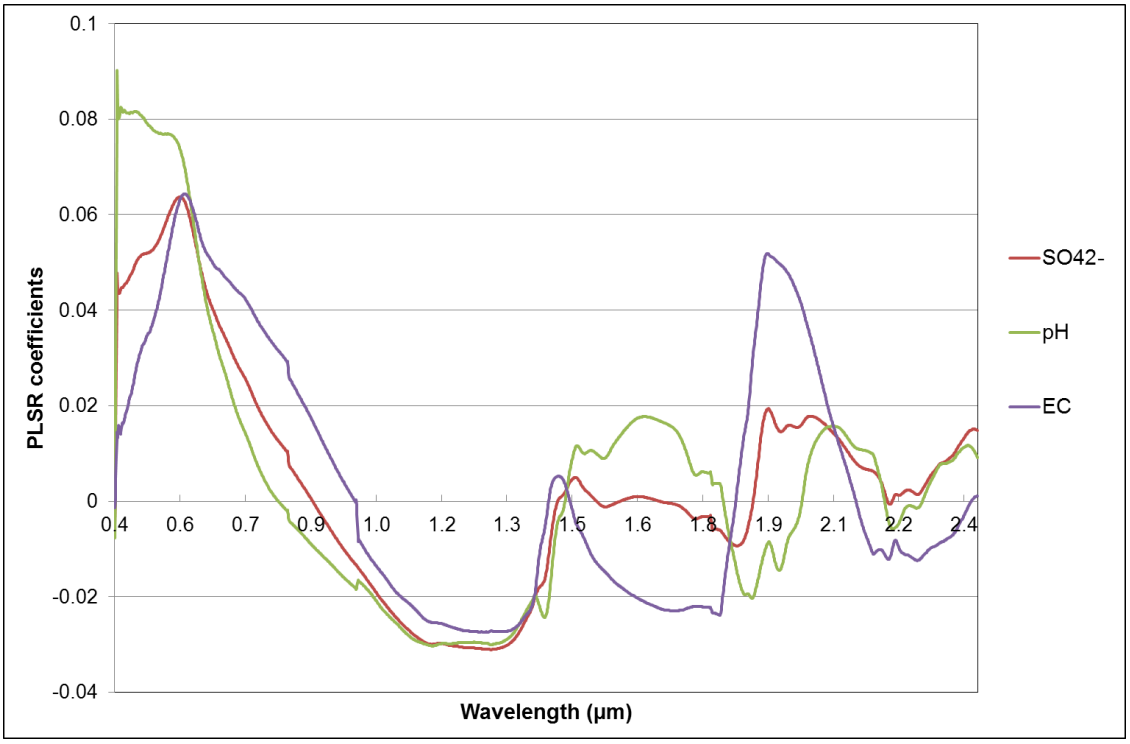

Figure 4-33 PLSR coefficients showing the contribution of each wavelength for development of geochemical models

Table 4-20 lists results of PLSR models for different spectral transformations on VIR, NIR and SWIR spectral ranges. Generally, the First Derivative (FD) transformation technique outperformed all other spectral techniques. The FD method produced high retrieval accuracies for SO_4^{2-} and stable estimation results for pH and EC. Continuum Removal is the second most important transformation technique. Original reflectance performed better than Log (1/R) transformation. By comparison, model results from the full wavelength range (400 – 2400 nm) outperformed the VIR, NIR and SWIR regions. The SWIR region showed reliable prediction accuracies with low prediction errors. Generally, low estimation accuracies can be attributed to high sample variability and geochemical behaviour of elements.

Prediction accuracy can be improved by reducing the wavelength range by making use of significant regions. QAF regression and PLSR coefficients show that better predictions for SO_4^{2-}

and pH can be found between 1400 – 2200 nm. The ranges between 960 nm – 1850 nm and 2100 nm and 2400 nm are useful for predicting electrical conductivity (EC).

Table 4-20 Performance of spectral transformation techniques for estimating geochemical variables using PLSR with bootstrapping (n=29).

		VIR-NIR-SWIR				VIR				NIR				SWIR			
Trans	Element	R^2	RMSEP	ME	RPD	R^2	RMSEP	ME	RPD	R^2	RMSEP	ME	RPD	R^2	RMSEP	ME	RPD
None	SO_4^{2-}	0.38	0.87	-0.10	1.29	0.43	0.84	0.03	1.33	0.42	0.84	0.01	1.33	0.29	0.93	-0.01	1.20
	pH	0.22	0.20	-0.01	1.15	0.32	0.19	-0.01	1.20	0.12	0.21	-0.01	1.08	0.08	0.22	0.02	1.03
	EC	0.41	0.78	-0.03	1.32	0.31	0.84	0.09	1.22	0.34	0.82	0.01	1.25	0.22	1.75	0.30	0.58
CR	SO_4^{2-}	0.29	0.93	-0.02	1.20	0.16	1.02	-0.01	1.10	0.21	0.98	-0.09	1.14	0.23	0.96	0.00	1.16
	pH	0.29	0.20	0.00	1.16	0.15	0.21	-0.01	1.10	0.26	0.20	0.02	1.18	0.24	0.96	0.06	1.16
	EC	0.40	0.78	-0.03	1.31	0.24	0.88	0.01	1.17	0.29	0.85	-0.05	1.20	0.35	0.81	-0.03	1.26
FD	SO_4^{2-}	0.58	0.71	-0.08	1.56	0.52	0.76	-0.03	1.47	0.48	0.79	-0.03	1.41	0.58	0.73	-0.10	1.53
	pH	0.41	0.18	0.00	1.30	0.37	0.19	0.00	1.24	0.23	0.20	0.00	0.16	0.45	0.17	0.01	1.34
	EC	0.43	0.76	-0.01	1.35	0.35	0.81	0.01	1.27	0.38	0.80	0.03	1.28	0.43	0.76	0.02	1.35
Log	SO_4^{2-}	0.37	0.84	0.04	1.23	0.08	0.97	-0.03	1.06	0.25	0.88	0.02	1.17	0.36	0.82	-0.05	1.26
	pH	0.37	0.89	-0.17	1.25	0.20	0.98	-0.05	1.14	0.21	0.98	-0.05	1.14	0.26	0.97	-0.19	1.15
	EC	0.40	0.18	0.02	0.13	0.20	0.20	0.00	1.13	0.20	0.20	0.01	1.13	0.42	0.18	0.00	1.28

Estimation accuracies can also be improved by using first derivative (FD) spectra. Stable and accurate predictions from FD spectra supports the argument by Wu *et al* (2007) that low resolution spectra with broader sampling intervals leads to higher prediction estimates than high resolution spectra. First Derivative transformation compresses the whole spectrum into few spectral (low resolution) bands, reduces signal to noise ratio (SNR) and enhanced absorption features.

4.5.5 Determination of important wavelengths in PLSR models

Partial least square regression (PLSR) weights (B coefficients) are used to determine the contribution of each wavelength in PLS models (Wold *et al*, 2001; Viscara-Rossel *et al*, 2006). The direction of the relationship between independent and dependent variables is represented by a negative or positive sign. The bigger (positive or negative) the coefficient in a specific wavelength, the stronger is the contribution to the model.

PLSR weights of normal reflectance spectra are drawn to highlight regions of spectral significance. Standard deviation of each dependent variable is used as a threshold value (Rong, 2009). Wavelengths bigger than the threshold value are considered significant. Standard deviation of PLSR weights of elements that showed reliable predictions estimates are shown in Table 4-21. Figure 4-34 shows B coefficients used in PLSR prediction models. Table 4-22 summarizes wavelength regions with bigger threshold values.

Table 4-21 B-coefficient standard deviation of selected geochemical variables

Element	SO_4^{2-}	pH	EC
STDev	0.04	0.01	0.04

Table 4-22 Significant spectral regions selected by PLSR weights

Element	Negative (nm)	Positive (nm)	Important wavebands (nm)
SO_4^{2-}	401-478	557-794 1861-2014	401-478 1861-2014
EC	1547-1777 401-500	741-900 1866-1987	401-500 1866-1987
pH	1914-1982 2149-2257	1584-1707 2016-2103	2149-2257

For all elements, wavelength regions around 1500nm, 1800-2100nm, 401-562nm and 2100-2260 nm show a significant contribution to PLSR models. Basically, there are the regions of known absorption features of clay and iron bearing minerals (Williams *et al*, 2002).

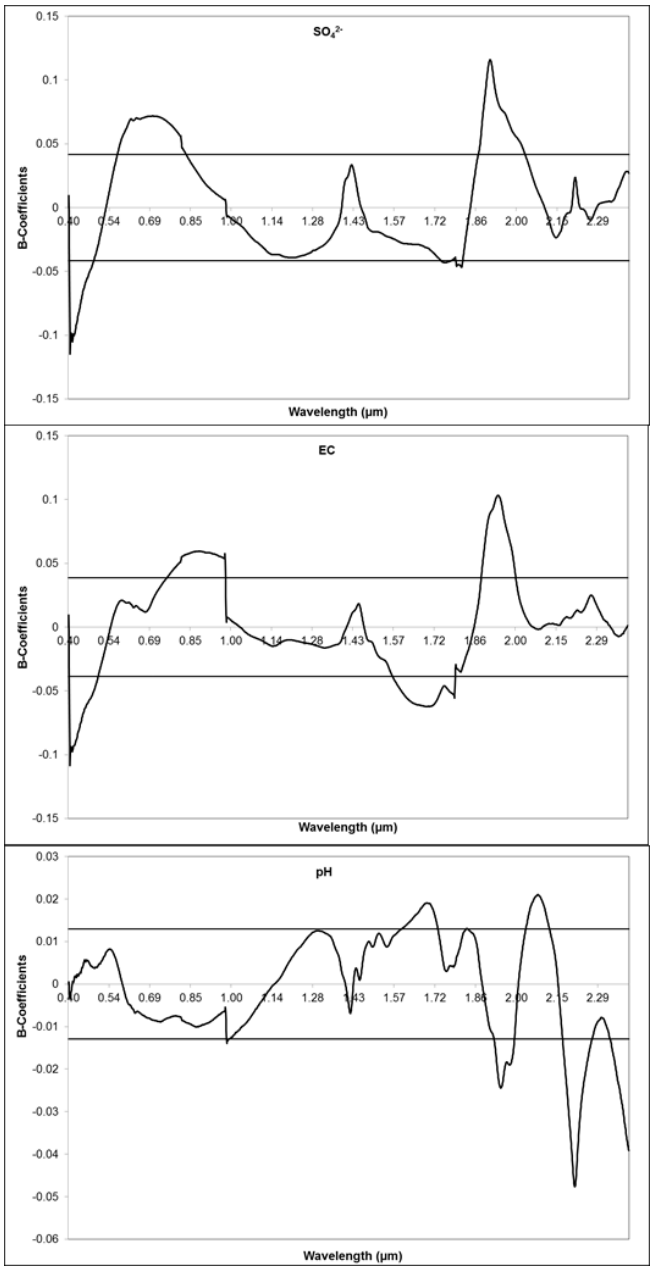

Figure 4-34 B coefficients (blue line) for SO_4^{2-}, EC and pH PLSR models. Black threshold lines are defined using standard deviation.

5 Conclusion and recommendations

Four types of salt precipitates were distinguishable using the Munsell colour chart as red precipitates, yellow precipitates, brown/gray precipitates and white precipitates. Precipitate groups showed high variation in terms of bulk chemistry. The content of major ions in all precipitates was similar. Red precipitates, and to a lesser extent Yellow precipitates are highly enriched in Siderophile elements such as V, Cr, Cu and As. White precipitates showed high enrichment of chalcophile elements Co, Ni, Zn and U. Lead (Pb) is the only element that showed enrichment in brown crusts. Sulphate (SO_4^{2-}) and Chlorine (Cl^-) showed high enrichment in all types of salt precipitates. These anions, together with soluble cations are responsible for high EC levels of the precipitates upon dissolution. Bulk chemistry and geochemical modeling revealed that elements such as Co, Cr, Ni, Pb, Zn and U occur in particulate solids at higher pH conditions and as free cationic species in low pH conditions.

Four geochemical indices were used to evaluate pollution levels associated with efflorescent precipitates. High PLI, Igeo and EF levels for major and trace elements occurred in wetland and bare field precipitates. The range of Pollution load index (PLI) indicated very high to ultra-high pollution levels. Compared with local water and soil standards, salt precipitates have up to 2 times high metal content. These results indicate that these salts act as hyper-accumulations of metals by incorporating them into their structure.

Near-infrared reflectance spectrum (350-2500 nm) of efflorescent salts was measured using the ASD Fieldspec Pro Spectrometer to study mineralogical and geochemical characteristics in order to assess contamination related to mine wastes. In the SWIR region clay minerals of the smectite group were dominant. Gypsum, jarosite and anhydrite are the most prominent sulphate minerals identified in the SWIR region. Aluminium sulphate salts were identified as thernadite,

eugusterite and blodite. Comparison of spectral identifiable minerals and XRD and SEM analysis results show some similarities with minor discrepancies. Clays and mica minerals showed good agreement in both methods. Efflorescent mineral precipitates consist of 5 types of sulphate mineral groups, namely;

Na, Mg Sulphite mineral Blodite

Mg sulphate minerals Hexahydrite and Starkeyite

Al sulphate minerals Alunogen, Tamarugite, Wupatkiite and Apjohnite

Fe sulphate mineral Jarosite

Ca sulphate sulphate mineral Gypsum.

Blodite was identified in low quantities by XRD. Thernadite was interpreted as apjohnite and eugusteri as Tamarugite. These sulphate minerals were not correctly identified by ASD because they are not included in reference spectral libraries. ASD and XRD discrepencies like copiapite-fibroferrite, epsomite-hexahydrite can be attributed to dehydration during storage of samples.

Generally, efflorescent precipitates consist of gypsum and Al-Mn-Mg-Na sulphate salts such as Tamarugite and Apjohnite. Ochre precipitates consist mainly of jarosite and hematite.

Geochemical modelling, following analysis of solutions formed by dissolving crusts in water, showed gypsum and jarosite as dominant minerals, indicating that iron and sulphate are the major ions responsible for acidity during precipitation and dissolution of mineral salts.

Measured reflectance and the concentration of measured geochemical variables showed significance difference in all types of precipitates. High reflectance was associated with white crusts. White crusts also have elevated concentrations of Cu, Co, Ni, Zn and U and Red Crust are enriched in As, Fe, Cr and V. Univariate statistical analysis showed that concentration of elements is strongly related to land-use and prevailing environmental conditions.

Applicability of hyperspectral data to estimate acidity was investigated by modelling geochemical variables using reflectance spectrum. Low negative correlation of these spectral signatures supports the hypothesis that the high concentrations of metals associated with the absorption surface weakens the absorption feature related of the surface because the decrease in surface functional groups of the mineral surfaces. Using the correlation matrix, QAF parameters were determined to model geochemical variables. Only 15% of the geochemical variables can be explained by QAF parameters. Good prediction estimates were obtained for SO_4^{2-}, EC and pH which are highly correlated with iron content.

Partial Least Squares Regression was performed to see if the reflectance spectrum can be related to geochemical variables. In addition to original reflectance, the study compared different spectral transformation techniques and found the First Derivative (FD) transformation to give better prediction estimates. Partial regression squares (PLSR) combined with bootstrapping show high capacity than regression analysis for modeling geochemical variables. Generally, prediction estimates were low. Poor predictions can be attributed to geochemical variability and physical variability of the samples. Reliable prediction estimates were obtained for elements with high EF values and very high coefficient of variation. Correlation pattern and partial least scores of geochemical variables show significant correlation with spectral regions of know absorption features related to Fe oxides and clay minerals.

Study of spectral indices found the Red and Blue parts of the spectrum are good indicators of salinity. Indices related to hematite/geothite content, Coloration index, Redness Index and Saturation index have significant correlation with EC and pH. In field and image spectroscopy, the regions around 1400 nm, 1900 nm and 2200 nm coincides with major absorption features and

consist of atmospheric noise. This study shows that regions around 550 nm, 705 nm and 2360 nm can be useful in differentiating salinity associated with efflorescent crust.

First derivative transformation is effective in reducing spectral noise and compresses the spectrum into few spectral bands. The high performance of FD spectra in highlighting spectral features and high predictions estimates means low to medium resolution remote sensing sensors like IKONOS and ASTER can predict metal content associated with mineral efflorescent.

The study has demonstrated the binding effect of trace elements to active mineral constituents, and this mechanism can be used to investigate spectrally featureless trace elements.

Study limitations

Availability of samples: Because efflorescent salts are highly unstable and disappear after the rain, their availability is unpredictable. This influenced the sampling strategy as representative samples were not easy to find. Sampling was limited only to areas where these salts are well developed and easily accessible.

Number of Sample: Because of limited resources, sample size of n =29 was obtained. This sample size was successful in identifying significant relationships in terms of chemistry. However, this sample size is too small for building PLSR models. Large sample size lead to more stable predictions models with better accuracies.

Lack of reliable secondary data: There is a huge variation in soil and groundwater chemical data reported in the EIA reports (SRK, 2012; Digby Wells Environmental, 2012); academic reports (Swanepoel, 2009; Phaleng, 2009; Tutu *et al*, 2011) and government report (DWA, 2012). This discrepancy makes it difficult to compare results and evaluate the hazard posed by the efflorescent salts.

Measure used to analyse data: All the samples were highly enriched in organic matter. Eliminating organic matter was carried out during sampling and sample preparation. The influence of organic matter is more pronounced in reflectance spectra. The study should have analysed the carbon and sulphur content of the samples. Since carbon is strongly associated with cations, it would have been a better indicator for metal pollution and a reliable predictor in PLSR modelling.

Based on the results of the study, the following recommendations can be made:

- A large dataset of samples is needed to build reliable prediction models. Prediction accuracies can be improved by reducing sample variability. Sampling should only focus on efflorescent salt and ochre precipitates and not composite sample.
- PLSR B-coefficients are useful in defining regions of spectral significance. Prediction accuracies can be improved by focussing on these regions. This will also reduce data to be used to modelling and therefore better statistical results.
- Better performance of FD transformations indicates low resolution spectrum is more useful than high resolution spectra in predicting geochemical variables. Low resolution spectra can be obtained by spectral resampling. The studied mineral crusts have weak Fe absorption in 400 nm – 1300 nm region. Sampling interval greater than 10 nm will mask iron features and only preserve major features at 1400 nm, 1900 nm and 220 0nm. For preserving all the absorption features, resampling intervals of 2 nm, 4 nm and 6 nm are recommended.

6 References

ABIYE, T.A., MENGISTU, H and DEMLIE, B.M., 2011. Groundwater resource in the crystalline rocks of the Johannesburg Area, South Africa. *Journal of Water Resource and Protection*, **3**, pp. 199-212.

ALLOWAY B.J., 1995. Heavy Metals in Soils. Chapman & Hall, London

CARBONE, C., DINELLI, E., MARESCOTTI, P., GASPAROTTO, G. and LUCCHETTI, G., 2013. The role of AMD secondary minerals in controlling environmental pollution: Indications from bulk leaching tests. *Journal of Geochemical Exploration,* **132**(0), pp. 188-200.

CARMONA, D.M., FAZ CANO, Á. and AROCENA, J.M., 2009. Cadmium, copper, lead, and zinc in secondary sulfate minerals in soils of mined areas in Southeast Spain. *Geoderma,* **150**(1–2), pp. 150-157.

CHENG, H., HU, Y., LUO, J., XU, B., and ZHAO, J. 2009. Geochemical processes controlling fate and transport of arsenic in acid mine drainage (AMD) and natural systems. J. Hazardous Materials **165**: pp. 13 – 26

CHOE, E., VAN DER MEER, F., VAN RUITENBEEK, F., VAN DER WERFF, H., DE SMETH, B. and KIM, K., 2008. Mapping of heavy metal pollution in stream sediments using combined geochemistry, field spectroscopy, and hyperspectral remote sensing: A case study of the Rodalquilar mining area, SE Spain. *Remote Sensing of Environment,* **112**(7), pp. 3222-3233.

CLOUTIS, E.A., HAWTHORNE, F.C., MERTZMAN, S.A., KRENN, K., CRAIG, M.A., MARCINO, D., METHOT, M., STRONG, J., MUSTARD, J.F., BLANEY, D.L., BELL III, J.F. and VILAS, F., 2006. Detection and discrimination of sulfate minerals using reflectance spectroscopy. *Icarus,* **184**(1), pp. 121-157

COETZEE, H., WADE, P., NTSUME, G. and JORDAAN, W. 2002. Radioactivity study on sediments in a dam in the Wonderfonteinspruit catchment. DWAF-Report 2002, Pretoria.

COETZEE, H., WINDE, F. and WADE, P., 2006. An assessment of sources, pathways, mechanisms and risks of current and potential future pollution of water and sediments in gold mining areas of the Wonderfonteinspruit catchment, Report, Water Research Commision, No1214/1/06. Pretoria.

CROWLEY, J., WILLIAMS, D.E., HAMMARSTROM, J.M., 2003. Spectral reflectance properties (0.4 – 2.5 μm) of secondary Fe-oxide, Fe-hydroxide, and Fe-sulphate-hydrate minerals associated with sulphide-bearing mine waste. Geochemistry: Exploration, Environment, Analysis **3**(0), pp. 219-228.

DE JONG, S.M., ADDINK, E.A., VAN BEEK, L.P.H. and DUIJSINGS, D., 2011. Physical characterization, spectral response and remotely sensed mapping of Mediterranean soil surface crusts. *Catena,* **86**(1), pp. 24-35.

DEHNI, A. and LOUNIS, M., 2012. Remote Sensing Techniques for Salt Affected Soil Mapping: Application to the Oran Region of Algeria. *Procedia Engineering,* **33**(0), pp. 188-198.

DEPARTMENT OF WATER AFFAIRS (DWA), 2012: Feasibility Study for a long-term solution to address the acid mine drainage associated with the East, Central and West Rand underground mining basins. Assessment of the water quality and quality of the Witwatersrand Mine Voids. Pretoria, South Africa.

DIGBY WELLS ENVIRONMENTAL, 2012. Final Scoping report for the immediate and short term interventions for the treatment of acid mine drainage (AMD) in the western, central and eastern basins of the Witwatersrand Gold fields. DEA Ref #: 12/1220/2403

DOLD, B., 2005. Basic concepts in environmental geochemistry of sulfide mine-waste. In: Memorias de XIX Curso International de Postgrado en Metalogenia. International UNESCO & SEG Short course in Metalogenesis., Quito, Ecuador, p. 113 – 151.

EQUEENUDDIN, S.M., TRIPATHY, S., SAHOO, P.K. and PANIGRAHI, M.K., 2010. Hydrogeochemical characteristics of acid mine drainage and water pollution at Makum Coalfield, India. *Journal of Geochemical Exploration,* **105**(3), pp. 75-82.

ESTIFANOS, S., 2006. Spectral indicators for assessing pollution in the epithermal gold mining area of Rodalquilar, SE Spain. MSc Thesis, University of Twente (ITC), Enschede.

FAN, C., XIE, H., WU, J. and BIRNBAUM, S., 2012. Analysis of United States Geological Survey spectral library of silicate minerals: implication for remote sensing applications.

FARIFTEH, J., VAN DER MEER, F., VAN DER MEIJDE, M. and ATZBERGER, C., 2008. Spectral characteristics of salt-affected soils: A laboratory experiment. *Geoderma,* **145**(3–4), pp. 196-206.

FERREIRA DA SILVA, E., BOBOS, I., XAVIER MATOS, J., PATINHA, C., REIS, A.P. and CARDOSO FONSECA, E., 2009. Mineralogy and geochemistry of trace metals and REE in volcanic massive sulfide host rocks, stream sediments, stream waters and acid mine drainage from the Lousal mine area (Iberian Pyrite Belt, Portugal). *Applied Geochemistry,* **24**(3), pp. 383-401.

FERRIER, G., HUDSON-EDWARDS, K. and POPE, R.J., 2009. Characterization of the environmental impact of the Rodalquilar mine, Spain by ground-based reflectance spectroscopy. *Journal for Geochemical Exploration,* **100**(1), pp. 11-19.

FITZPATRICK, R.W., GREALISH, G., SHAND, P., THOMAS, B.P., MERRY, R.H., CREEPER, N.L., RAVE, M. D., and JAYALATH, N. 2009. Preliminary Risk Assessment of Acid Sulfate Soil Materials in the Currency Creek, Finniss River, Tookayerta Creek and Black Swamp region, South Australia. CSIRO Land and Water Science Report 01/09., 45 pp

GANNOUNI, S., REBAI, N. and ABDELJAOUED, S., 2012. A Spectroscopic Approach to Assess Heavy Metals Contents of the Mine Waste of Jalta and Bougrine in the North of Tunisia. Scientific Research Publishing.

GIERÉ, R., SIDENKO, N.V. and LAZAREVA, E.V., 2003. The role of secondary minerals in controlling the migration of arsenic and metals from high-sulfide wastes (Berikul gold mine, Siberia). *Applied Geochemistry,* **18**(9), pp. 1347-1359.

HAMMARSTROM, J.M., SEAL II, R.R., MEIER, A.L. and KORNFELD, J.M., 2005. Secondary sulfate minerals associated with acid drainage in the eastern US: recycling of metals and acidity in surficial environments. *Chemical Geology,* **215**(1–4), pp. 407-431.

HARRIS, D.L., LOTTERMOSER, B.G. and DUCHESNE, J., 2003. Ephemeral acid mine drainage at the Montalbion silver mine, north Queensland. *Australian Journal of Earth Sciences,* **50**(5), pp. 797-809.

HOBBS, P.J and COBBING, J.E., 2007. A hydrogeological assessment of acid mine drainage impacts in the West Rand Basin, Gauteng Province. Report no. CSIR/NRE/WR/ER/2007/0097/C. CSIR/THRIP Pretoria. South Africa

JOECKEL, R.M., CLEMENT, B.J. and VANFLEET BATES, L.R., 2005. Sulfate-mineral crusts from pyrite weathering and acid rock drainage in the Dakota Formation and Graneros Shale, Jefferson County, Nebraska. *Chemical Geology,* **215**(1–4), pp. 433-452.

KALENDER, L. and ÇIÇEK UÇAR, S., 2013. Assessment of metal contamination in sediments in the tributaries of the Euphrates River, using pollution indices and the determination of the pollution source, Turkey. *Journal of Geochemical Exploration,* **134**(0), pp. 73-163.

KHAN, N.M., RASTOSKUEV, V.V., SHALINA, E.V. and SATO,Y., 2001. Mapping Salt-Affected Soils using remote sensing Indicators – A simple approach with the use of GIS IDRISI. Proceedings of the 22nd Asian Conference on Remote Sensing, 5-9 November, Singapore. Center for Remote Imaging, sensing and Processing (CRISP), National University of Singapore; Singapore Institute of Surveyors and Valuers; Asian association on remote sensing.

KRUSZEWSKI, Ł., 2013. Supergene sulphate minerals from the burning coal mining dumps in the Upper Silesian Coal Basin, South Poland. *International Journal of Coal Geology,* **105**(0), pp. 91-109.

LI, M., FANG, X., YI, C., GAO, S., ZHANG, W. and GALY, A., 2010. Evaporite minerals and geochemistry of the upper 400 m sediments in a core from the Western Qaidam Basin, Tibet. *Quaternary International,* **218**(1–2), pp. 176-189.

LOSKA, K., WIECHUŁA, D. and KORUS, I., 2004. Metal contamination of farming soils affected by industry. *Environment international,* **30**(2), pp. 159-165.

LULEVA, M.I., 2007. Identification of soil properties variation using spectral and statistical analysis on field samples and aster imagery: a case study of Tunisia. MSc Thesis, University of Twente (ITC), Enschede.

MARITZ, H., CLOETE, H. C. C. and ELSENBROEK, J. H. 2010. Analysis of High Density Regional Geochemical Soil Samples at the Council for Geoscience (South Africa): The Importance of Quality Control Measures. *Geostandards and Geoanalytical Research,* **34**, pp. 265–273.

MCCARTHY, T. S., 2006. The Witwatersrand Supergroup, The Geology of South Africa. Geological Society of South Africa, 155—185.

MCCARTHY, T.S., 2011. The impact of acid mine drainage in South Africa. *South African Journal of Science.* **107** (5/6), 712. pp. 7.

METTERNICHT, G.I. and ZINCK, J.A., 2003. Remote sensing of soil salinity: potentials and constraints. *Remote Sensing of Environment,* **85**(1), pp. 1-20.

MONTERO S., I.C., BRIMHALL, G.H., ALPERS, C.N. and SWAYZE, G.A., 2005. Characterization of waste rock associated with acid drainage at the Penn Mine, California, by ground-based visible to short-wave infrared reflectance spectroscopy assisted by digital mapping. *Chemical Geology,* **215**(1–4), pp. 453-472.

MUNSELL COLOR. 1998. *Munsell Soil Color Charts*. Munsell Color Gretag Macbeth. New Windsor, New York

MUTANGA, O., 2004. Hyperspectral remote sensing of tropical grass quality and quantity. PhD Thesis, University of Twente (ITC), Enschede.

NAICKER, K., CUKROWSKA, E. and MCCARTHY, T.S., 2003. Acid mine drainage arising from gold mining activity in Johannesburg, South Africa and environs. *Environmental Pollution*, **122**(1), pp. 29-40.

NENGOVHELA, A.C., YIBAS, B., and OGOLA, J.S., 2006. Characterisation of gold tailings dams of the Witwatersrand Basin with reference to their acid mine drainage potential, Johannesburg, South Africa. Water SA **32(**4), pp. 499 – 506.

ONAC, B. P., VERES, D., KEARNS, J., CHIRIENCO, M.., MINUT, A., BREBAN, R., 2003. Secondary sulfates found in an old adit from Rosia Montana, Romania. Studia Universitatis Babes-Bolyai, Geologia 48, pp. 29-44.

PARKHURST, D.L. and APPELO, C.A.J., 1999, User's guide to PHREEQC (version 2) A computer program for speciation, batch-reaction, one-dimensional transport, and inverse geochemical calculations: U.S. Geological Survey Water-Resources Investigations Report 99-4259, 312 p

PHALENG, D, M. 2009. Anthropogenic impacts on the integrity of the Blesbokspruit catchment: a case study on surface water pollution. MSc Dissertation, University of Johannesburg, Johannesburg.

QUENTAL, L., SOUSA, A.J., MARSH, S., BRITO, G. and ABREU, M.M., 2011. Imaging spectroscopy answers to acid mine drainage detection at S. Domingos, Iberian Pyrite Belt, Portugal. *Comunicaçõe Geológicas,* **98**(8), pp. 61-71.

RAMOELO, A., SKIDMORE, A.K., CHO, M.A., MATHIEU, R., HEITKÖNIG, I.M.A., DUDENI-TLHONE, N., SCHLERF, M. and PRINS, H.H.T., 2013. Non-linear partial least square regression increases the estimation accuracy of grass nitrogen and phosphorus using

in situ hyperspectral and environmental data. *ISPRS Journal of Photogrammetry and Remote Sensing,* **82**(0), pp. 27-40.

RAMONTJA, T., COETZEE, H., HOBBS, P.J., BURGESS, J.E., THOMAS, A., KEET, M., YIBAS, B., van TONDER, D., NETILI, F., RUST, U.A., WADE, P., MAREE, J. 2011. Mine water management in the Witwatersrand Gold Fields with special emphasis on acid mine drainage. Inter-ministerial-Committee on acid mine drainage, Pretoria. 146pp

RIAZA, A., BUZZI, J., GARCIA-MELENDEZ, E., VAZQUEZ, I., BELLIDO, E., CARRERE, V. and MUELLER, A., 2012. Pyrite mine waste and water mapping using Hymap and Hyperion hyperspectral data. *Environmental Earth Sciences,* **66**(7), pp. 1957-1971.

RIAZA, A., and MULLER, A. 2009. Hyperspectral remote sensing and monitoring od pyrite mine wastes: a record of climate variability (Pyrite Belt, Spain), *Environmental Earth Sciences,* **61**, pp. 575-594.

RONG, Z., 2009. Estimation of foliar chemicals as indicators of tea (*Camellia sinensis L*) quality using reflectance spectroscopy. MSc Thesis, University of Twente (ITC), Enschede.

ROSNER, T., VAN SCHALKWYK, A, 2000. The environmental impact of gold mining tailings footprints in the Johannesburg region, South Africa. Bull. Eng. Geol, Environ. 122, 137-148.

ROYCHOUDHURY, A.N. and STARKE, M.F., 2006. Partitioning and mobility of trace metals in the Blesbokspruit: Impact assessment of dewatering of mine waters in the East Rand, South Africa. *Applied Geochemistry,* **21**(6), pp. 1044-1063.

SRACEK, O., VESELOVSKÝ, F., KŘÍBEK, B., MALEC, J. and JEHLIČKA, J., 2010. Geochemistry, mineralogy and environmental impact of precipitated efflorescent salts at the Kabwe Cu–Co chemical leaching plant in Zambia. *Applied Geochemistry,* **25**(12), pp. 1815-1824.

SRK Consulting, 2012. Water study for input to the EIA for the Waste Licencing of Waste Management Activities at Impala Platinum Refineries, Springs, 2012

STIFANOS, S., 2006. Spectral indicators for assessing pollution in the epithermal gold mining area of Rodalquilar, South East Spain. MSc Thesis, University of Twente (ITC), Enschede.

SUTTON, M.W., WEIERSBYE, I.M., and GALPIN, J.S., HELLER, D. 2006. A GIS-based history of gold mine residue deposits and risk assessment of post-mining land-use on the Witwatersrand Basin, South Africa. Mine Closure 2006.

SUTTON, M, W., 2012. Use of remote sensing and GIS in a risk assessment of gold and uranium mine residue deposits and identification of vulnerable land use. Msc Thesis, University of Witwatersrand, Johannesburg

SWANEPOEL, C, L. 2009. An assessment of the health-related microbiological water quality of the Blesbokspruit. MSc Dissertation. University of Johannesbug, Johannesbug.

TAYLOR, S.R. and MCLENNAN, S.M., 1995. The geochemical evolution of the continental crust. *Reviews in Geophysics* **33**, pp. 241-265.

THORIUS, S., 2004. The effects of Grootvlei Mine water on the Blesbokspruit. MSc Thesis. University of Johannesburg, Johannesburg.

TUTU, H., 2005. Determination and geochemical modeling of the dispersal of uranium in gold-mine polluted land on the Witwatersrand, PhD thesis, University of the Witwatersrand, Johannesburg.

TUTU, H., MCCARTHY, T.S. and CUKROWSKA, E., 2008. The chemical characteristics of acid mine drainage with particular reference to sources, distribution and remediation: The Witwatersrand Basin, South Africa as a case study. *Applied Geochemistry,* **23**(12), pp. 3666-3684.

TUTU, H., CAMDEN-SMITH, B., CUKROWSKA, E.M., BAKATULA, E.N., WEIERSBYE, I.M., SUTTON, M.S. 2011. Mineral efflorescent crusts as sources of pollution in gold mining environments in the Witwatersrand Basin. Proceedings of the 11th International Congress on Mine Water and the Environment, Aachen, Germany. Rüde, T., Freund, K., and Wolkersdorfer, C. Editors. International Mine Water Association, pp. 623 – 626

VALENTE, T.M. and LEAL GOMES, C., 2009. Occurrence, properties and pollution potential of environmental minerals in acid mine drainage. *Science of The Total Environment*, **407**(3), pp. 1135-1152.

VAN DER MEER, F., 2004. Analysis of spectral absorption features in hyperspectral imagery. *International Journal of Applied Earth Observation and Geoinformation* **5** (0), pp. 55 – 68.

VELASCO, F., ALVARO, A., SUAREZ, S., HERRERO, J. and YUSTA, I., 2005. Mapping Fe-bearing hydrated sulphate minerals with short wave infrared (SWIR) spectral analysis at San Miguel mine environment, Iberian Pyrite Belt (SW Spain). *Journal of Geochemical Exploration*, **87**(2), pp. 45-72.

VISCARRA ROSSEL, R.A., WALVOORT, D.J.J., MCBRATNEY, A.B., JANIK, L.J. and SKJEMSTAD, J.O., 2006. Visible, near infrared, mid infrared or combined diffuse reflectance spectroscopy for simultaneous assessment of various soil properties. *Geoderma*, **131**(1–2), pp. 59-75.

VISCARRA ROSSEL, R.A., 2008. ParLeS: Software for chemometric analysis of spectroscopic data. *Chemometrics and Intelligent Laboratory Systems*, 90(1), pp. 72-83.

WEIERSBYE, I.M., WITKOWSKI, E.T., REICHARDT, M. 2006a. Floristic composition of gold and uranium tailings dams, adjacent polluted areas, on South Africa's deep level mines. Bothalia **36**(1), pp. 101-127

WEIERSBYE, I., N. MARGALIT, T. FEINGERSH, G. REVIVO, R. STARK, Y. ZUR, D. Heller, O. and Cukrowska, E.M., 2006b. Use of airborne hyper-spectral remote sensing

(HSRS) to focus remediation and monitor vegetation processes on gold mining landscape in South Africa, Mine Closure 2006, Proceedings of the First International Seminar on Mine Closure, Eds. A. Fourie & M. Tibbett 13-15 September, Perth Australia, pp 601-611

WEISBROD, N., PILLERSDORF, M., DRAGILA, M., GRAHAM, C., CASSIDY, J. and COOPER, C.A., 2005. Evaporation from fractures exposed at the land surface: Impact of gas-phase convection on salt accumulation. *American Geophysical Union,* **162** (7-4), pp. 1-15.

WILLIAMS, D.J., BIGHAM, J.M., CRAVOTTA III, C.A., TRAINAA, S.J., ANDERSON, J.E. and LYON, J.G., 2002. Assessing mine drainage pH from the color and spectral reflectance of chemical precipitates. *Applied Geochemistry,* **17**(10), pp. 1273-1286.

WOLD S. M., SJÖSTRÖM, and L. ERIKSSON. 2001. PLS-regression: a basic tool of chemometrics. *Chemom. Intell. Lab. Syst.* **58** (2), pp. 109-130.

WU, Y., CHEN, J., JI, J., GONG, P., LIAO, Q., TIAM, Q., MA, H. 2007. A mechanism study of reflectance spectroscopy for investigating heavy metals in soils. *Soil Sci Soc. Am.J* **7**(3), pp 918 – 926.

XIE, X., PAN, X. and SUN, B., 2012. Visible and Near-Infrared Diffuse Reflectance Spectroscopy for Prediction of Soil Properties near a Copper Smelter. *Pedosphere,* **22**(3), pp. 351-366.